Study on LEO Satellite Charging and Associated Plasma Disturbance in the Ionosphere

NIZAM, AHMAD

(Degree)
博士（計算科学）
(Date of Degree)
2019-03-25
(Date of Publication)
2020-03-01
(Resource Type)
doctoral thesis
(Report Number)
甲第7519号
(URL)
https://hdl.handle.net/20.500.14094/D1007519

Doctoral Dissertation

Study on LEO Satellite Charging and Associated Plasma Disturbance in the Ionosphere
（電離層における地球低軌道衛星の帯電とそれに伴うプラズマ擾乱に関する研究）

January 2019

Graduate School of System Informatics,
Kobe University

Nizam Ahmad

Study on LEO Satellite Charging and Associated Plasma Disturbance in the Ionosphere

Nizam Ahmad

ABSTRACT

The placement of satellite in space will always be affected by space environment resulting in various impacts from temporary faults to permanent failures depending on several factors such as satellite orbit, level of solar and geomagnetic activities, satellite local time and types of satellite material. Anomaly events commonly occured during the period of high geomagnetic activity that also triggered the plasma variation in low earth orbit (LEO) environment. Diagnosis process used electron data from MEPED (Medium Energy Proton and Electron Detector) onboard NOAA 15 satellite in addition to fluctuated electron fluxes associated with geomagnetic disturbances within period of 3 days prior to and after the anomaly day. We selected 20 LEO anomaly cases registered in satellite news digest (SND) database in the period of year 2000 to 2008. Satellite local time, one of important parameters in the anomaly diagnosis, is determined by using propagated two line elements (TLE) of Simplified General Perturbations-4 (SGP4) to calculate the Longitude of Ascending Node (LAN) of satellite through the position and velocity vectors. The results showed that the majority of LEO satellite anomalies were linked to the low energy electron fluxes of 30 - 100 keV and associated with the magnetic perturbations which had higher correlation coefficient (~ 90%) on the day of anomaly. The mean local time calculation during the day of anomaly with respect to the nightime migration of energetic electrons revealed that the majority of anomalies (65 %) occured on the night side of the earth from dusk to dawn sector of magnetic local time.

We then investigated the failures related charging on LEO satellites since the majority of failures subject to environmental charging. In the absence of perturbations from auroral electrons, overall the potential on the spacecraft is less than 3V (negative), whereas the cases by including auroral electrons impact insignificantly contributes to high level charging. This is due to smaller flux ratio of auroral electrons to ambient plasma. In general, ion void region in the near-wake exists in most cases, but more distorted as the object potential becomes more negative. The distorted ion void is more pronounced in the presence of auroral electrons. Simulation done for 20 LEO cases shows the potential dependence on electron temperature rather than density of which floating potential decreases as the electron temperature increases reaching confidence level of 99%.

Simulation done by increasing auroral electron density so that the flux ratio of auroral electrons to ambient plasma becomes unity giving rise to increasing magnitude of negative potential, but still less than 20V. There exists ion focusing inside the wakefield in addition to ion void structure. It is likely to be related to ion trajectory deflection by the electric field as the potential of the spacecraft becomes much more negative. Furthermore, the inclusion of photoelectrons inspite of auroral electrons in simulation disappears the ion void structure and turns out to be ion focusing in the near-wake spanning up to mid-wake region. The ion-back flow due to potential distribution might be contribute to defocusing ion in this region. The confirmation of ion focusing structure is done through numerous simulations using fixed and floating potential. There exists discrepancy between two cases where the ion focusing in the former case is temperature ratio and potential dependence, whereas the latter case is likely to be attributed to flux ratio of auroral electrons to ambient plasma giving rise to ambi polar electric field. This field plays role to accelerate ions in the wake field leading to ion-rich region.

Acknowledgements

In the name of Allah, the Beneficent, the Merciful. First of all, allow me to quote a beautiful verse in my holy book, Quran {3:190-191}

> *Most surely in the creation of the heavens and the earth and the alternation of the night and the day are signs for those who understand [190]. Those who remember Allah standing and sitting and lying on their sides and reflect on the creation of the heavens and the earth, [saying], "Our Lord, Thou has not created this in vain! Glory be to Thee; save us then from the chastisement of the fire [191]."*

I would first like to thank Allah, Almighty God, for giving me everything to accomplish my Ph.D. course. I would also like to express my gratitude to the most respectable person, Prophet Mohammed (Peace Be Upon Him).

Working in the field of space science and spacecraft charging are really wondrous for me due to full of interesting mysteries to be resolved. For this, it's an honor for me to have a great advisor, Prof. Hideyuki Usui, who has guided me and opened the way for me to comprehend those fields. I really appreciate for your time, favor, patience and all supports from you during my study.

I would like to extend my appreciation to Dr. Yohei Miyake who has taught and guided me how to perform simulations using EMSES based on Particle-In-Cell method. It was really nice to have fruitful discussions with you during my Ph.D. course. I also really thank you for helping me preparing documents needed for the completion of my study.

I will not forget to express my sincere gratitude to Prof. Kageyama and Prof. Matoba for their beneficial suggestions to improve the quality of my dissertation.

I would like to express my thankfulness to Prof. Thomas Djamaluddin who has guided me how to be a good scientist. I wish to express my gratitude to the Ministry of Research and Technology under Secretariat of Project Management Office (PMO) Research and Innovation in Science and Technology Project (RISET-PRO) and National Institute of Aeronautics and Space (LAPAN) for supporting and facilitating all my activities during the Ph.D. study program.

I would like to humbly express my gratitude to my beloved mother and father as well as my parents-in-law for their prayer day and night. I would never completed my study without full support of wife, Khairani Mardiah, and my three beloved kids, Hana, Azami and Hafizh. " Dear loves! we have stepped a thousand miles away and gone through the bittersweet of life together".

Lastly, I would like to acknowledge my friends in Usui's laboratory, Oki, Uko, Sasaki and the others as well as all staff members at administration office of faculty of engineering of Kobe university for their help and support during my study. I hope I can meet you all, someday, somewhere with new atmosphere.

Contents

List of Figures

List of Tables

Chapter 1

Introduction

1.1. Satellite Anomaly

Placing a satellite into space is challenging not only due to the technical aspects of mission requirements but also due to the space environment where the satellite is placed and operated. The variability of the space environment around the satellite can lead to multiple effects, such as loss of performance in satellite subsystems. Some effects present low-level and temporary risks from which the satellite can recover, but others present high-level risks that can result in notorious failures that stop satellite operation permanently. Although the reliability of satellites is tested and proved well before launch to avoid damage during operation, nevertheless failures arise due to many factors, including command errors, mechanical and electrical faults, and design or manufacturing problems, as well as environmental effects on the satellite (Vampola 1994).

The causes of satellite failures are generally difficult to diagnose accurately, so they are often called anomalies. Documentation of numerous anomaly cases and knowledge about the proximate causes leads to an understanding that plasma variation around satellites also plays an important role in anomalies through the interaction between the plasma and satellite system. The interaction gives rise to various impacts on satellites, depending on satellite orbit, relative position in space, satellite local time (SLT), solar and geomagnetic activities, and materials in the satellite structure (Hastings and Garret 1996).

It is believed that satellite anomalies predominantly occur during periods of high geomagnetic activity, which can change plasma properties abruptly and accelerate electrons and ions to energies on the order of kiloelectronvolts. Electrons and ions with energies above tens of kiloelectronvolts are known to greatly contribute to spacecraft charging phenomena (Lai 2012). Since the thermal speed of electrons is much larger than that of ions, the electron impact on satellites becomes of prime interest for satellite anomaly diagnosis, especially in low Earth orbit (LEO) environments below an altitude of 1,000 km.

The effects of charging due to plasma variation on LEO satellites are not critical except in some regions, such as polar regions and a small equatorial region called the South Atlantic Anomaly. Plasma in those regions is cold and dense with typical energies less than 10 keV, but it can change rapidly during periods of high geomagnetic activity. Rapid changes in plasma properties around a satellite can be problematic for some sensors and even for the satellite itself through charging effects. Plasma variations in LEO can be destructive because the collective plasma can release sufficient energy to the satellite to cause effects such as surface charging, detector contamination, and surface chemical reactions (Hastings 1995). It is of interest that satellite charging occurs in finite time until an equilibrium state is reached (Lai 2012). Moreover, the current balance on a satellite due to its interaction with plasma strongly depends not only on material properties but also the flux of energetic particles along the satellite trajectory.

One of challenges in diagnosing satellite anomalies arises from the limited amount of anomaly data because some anomalies were not formally or thoroughly documented (Koons et al. 2000). In addition, it is difficult to maintain a comprehensive database in which all anomalies are categorized by, for example, satellite orbit type, material properties, position on the anomaly day, Satellite Local Time (SLT), type of anomaly, and space weather at the time of the anomaly. In addition, the database should contain detailed descriptions of anomalies, including the initial presumption of cause, and it should be up to date.

Numerous studies have been published regarding satellite anomaly events, including the estimation of causes, but the majority of research is more concerned with geosynchronous Earth orbit (GEO) satellites, with few studies looking at anomalies in LEO and medium Earth orbit satellites (Fennel et al. 2001; Belov et al. 2005; Pilipenko et al. 2006; Iucci et al. 2006; Patil et al. 2008; O'Brien 2009; Choi et al. 2011; Thomsen et al. 2013). In addition, in any attempt to find anomaly causes related to environmental changes, most analyses used high-energy particle data at energies on the order of megaelectronvolts for both electrons and protons.

It is a challenge to study anomaly cases for satellites in LEO environment because they were the most numerous among active satellites in 2015, with a total of 696 (53.33%) satellites in LEO, whereas satellites in GEO number about 481 (36.86%) (http://www.ucsusa.org). In other words, the population of LEO satellites is significantly higher than that of GEO satellites (SIA 2015).

1.2. Satellite Charging

It is evident that malfunction or failures on satellites commonly attributed to charging and it has been acclaimed as the main source of spacecraft anomalies (Koons et al. 2000). The level of charging depends on the energy of particles interacting with the spacecraft. At lower level of energy, the form of interaction of charged particles with the spacecraft only affect the surface part called surface charging. However, the higher level of energy gives rise to severe effects in which the charged particles can penetrate deep inside the spacecrafts components resulting in internal charging (Fennell et al. 2001).

The charging on the spacecraft depends strongly on the current balance inflow or outflow of spacecraft. If the spacecraft is more exposed to incoming currents than outgoing currents, the potential difference on spacecraft will immediately increase and then gradually drop until the net current balance is settled up. In most cases, electron currents play important role in charging mechanism. In thermal equilibrium, due to the mass difference between electrons and protons, plasma electrons overall have much larger velocity than that of protons (~ 43 times) resulting in highly collision of electron currents onto spacecraft compared to ion currents. This can be interpreted as an increase of negative voltage of spacecraft due to incoming electron currents where the potential is confined to certain length (sheath) depending on the plasma density and potential of spacecraft (Frooninckx 1991).

At the beginning, it is believed that high level charging only occurred on GEO spacecraft due to hot and tenuous plasma in this regime. The varied plasma density with energy range from the order of few eV to tens of keV can charge the spacecraft up to -10 kV as sustained by ATS-5 satellite (DeForest 1972). In contrast to GEO environment, overall the LEO environment has a dense and cold plasma and can only charge the spacecraft less than 10 V (negative). However, in some occasions the LEO environment can be harsh to spacecraft especially in polar region where precipitating auroral electrons are so intense during magnetically disturbed condition.

The precipitating auroral electrons can severly charge the spacecraft negatively up to the 100 V (Frooninckx 1991). On May, 1995, The Defense Meteorological Satellite Program F13 (DMSP F13) satellite at 840 km altitude has been reported to experience high-voltage charging up to around 459 V (Anderson and Koons 1996). The previous study done by Gussenhoven et al (1985) pointed out that DMSP satellite undergone high-level charging under characterized conditions, i.e., ionospheric plasma density lower than 10^4 cm^{-3}, the precipitating auroral electrons energy on the order of tens of keV has reached flux up to 10^8 electrons/cm^2/s/sr and spacecraft was exposed to eclipse. Furthermore, Frooninckx and Sojka (1992) found solar cycle dependence of LEO charging events with emphasis that the energetic electron fluxes subjected to charging were insignifcantly varying between solar maximum and minimum. However, the decrease of plasma density at solar maximum leads to significant contribution of currents from the precipitating auroral electrons on LEO satellite.

An obvious indication of high level charging on LEO polar satellites linked to auroral electrons can be seen through further study done by Mazur et al. (2011) which was exploiting SAMPEX satellite charging; Colson (2011) identified charging on DMSP F16, F17 and F18 serial satellites; Anderson (2012) analyzed 1600 DMSP satellite charging events over 12-year period; Eriksson and Wahlund (2005) investigated Freja satellite charging statistically and numerically using POLAR code. In addition, numerical simulation has been progressively done in conjuction with LEO polar satellite charging and its environment as shown by Cooke (2003) by employing Potential of Large Spacecraft in the Auroral Region (POLAR) code for DMSP satellite charging. Furthermore, Wang et al. (2008) performed Particle-in-Cell (PIC) simulation of surface charging in LEO environment attributed to hot auroral electrons.

Since LEO satellite anomaly related charging becomes primary interest nowadays, it is important to study more anomaly cases on LEO satellites by performing not only statitistical approach but also numerical simulation. While numerous studies hitherto exploited the approximated parameters, here we attempted to numerically simulate LEO anomalies related charging by applying the empirical parameters on the day of spacecraft anomaly. We performed simulation by employing PIC model to attain the electric potential, as indicator of charging levels, including the property of wake structure behind the LEO satellites used in this study.

Chapter 2

Space Weather and Spacecraft Anomaly

Space weather describes the condition in the space environment that varies in time (Figure 2.1) and can affect, e.g., the performance and reliability of the space-borne technology such as satellite and rocket (Schwenn 2006). The effects of solar disturbances can modify the terrestrial magnetic configuration leading to changes of plasma property in space. Numerous studies found that the space weather greatly contributes to spacecraft anomalies (Belov et al. 2004 ; Patil et al. 2008 ; Choi et al. 2011). In this chapter we present some geophysical parameters commonly used to diagnose anomaly phenomena on the spacecraft. The motivation is to find the relationship between anomaly cases and these parameters as one of contributors of anomaly events. We demarcate the analysis on LEO satellite and its environment as primary concern of this study. We also limit our discussion about geophysical parameters that cover the geomagnetic activity and low energy particle fluxes as presented in the next subsections.

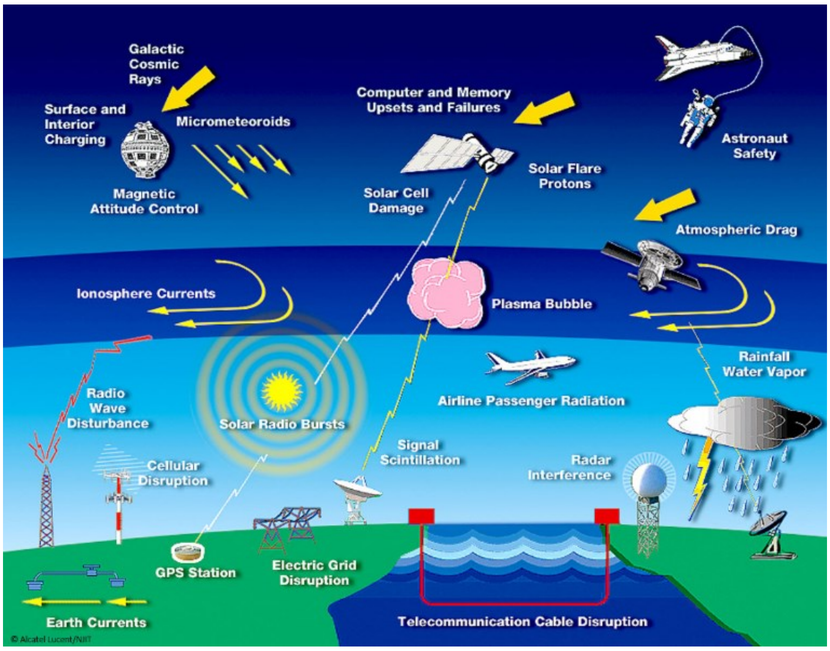

Figure 2.1 : Space Weather affects on space-borne and ground based infrastructures (https://www.nasa.gov/)

2.1.Geomagnetic Activity

It has been shown that the number of spacecraft anomalies raised up during periods of intense geomagnetic activity (Farthing et al. 1982 ; Lam and Hruska 1991). The rapid changes in geomagnetic activity can lead to satellite disorientation, induced currents in conductors, spacecraft on-board interference and decreasing satellite altitude affecting communication loss to the ground station (Dorman et al. 2005). In addition, some anomaly occurrences, spacecraft charging and electrical discharges also have a good agreement with geomagnetic activity (Lam and Hruska 1991). Hence, it is important issue to first discuss the role of geomagnetic activity in the spacecraft anomaly phenomena.

The strength of geomagnetic field can be characterized using some indices, but the most commonly used are Kp and Dst. Both indices have been preferentially associated with spacecraft anomalies as seen in Belov et al. (2004), Patil et al. (2008), and Choi et al. (2011).

2.1.1 Planetary Magnetic Activity Index (Kp)

Kp index is an indicator of global geomagnetic disturbance counted with a scale from 0 to 9. It can represent global magnetic activities in high and middle latitudes (Prolls 2004). It quantifies, in the absence of geomagnetic disturbance, the field-align current stream into and out of the auroral oval, while during the geomagnetic storm the auroral electrojets can extend toward the equatorial region. The latter case, in spite of the field-align current, the ionospheric current can also contribute to Kp measurement (Rostoker 2000). Kp index is measured by 13 stations located at midlatitudes of 44°and 60° north/south geomagnetic latitudes (Figure 2.2) and counted over three-hour intervals (Pisacane 2008).

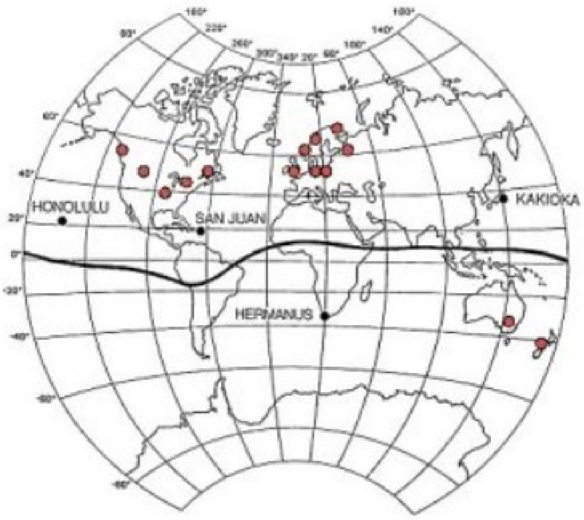

Figure 2.2 : Distribution of laboratories for Kp index measurement (http://www.ingv.it/ufficio-stampa/research-areas/sun-earth/)

In general, a larger Kp index corresponds to more anomaly occurrences. Farthing et al. (1982) showed that anomalies on the GOES satellite series were clearly linked to Kp index values ranging from 1 to 6. Their finding showed that the overall tendency of anomalies increased with higher Kp. Fennel et al. (2001) also found that highly elliptical orbit satellite anomalies increased with increasing Kp. Furthermore, Choi et al. (2011) found that, although some GEO satellite anomalies were linked to lower Kp values, the number of GEO anomalies increased with increasing Kp.

2.1.2 Disturbance Storm Time Index (Dst)

The level of geomagnetic disturbance can also be indicated by the Dst index, which quantifies plasma changes in the ring current due to those disturbances. It is measured hourly from four low-latitude magnetic observatories such as Honolulu, San Juan, Hermanus and Kakioka (Figure 2.3). The Dst index is not only used progressively to measure the symmetric ring current of magnetic storms, but also to quantify the partial (asymmetric) ring current, the tail current and field-aligned currents (FACs) that connect the low-latitude and high-latitude ionosperic currents (Prolls 2004).

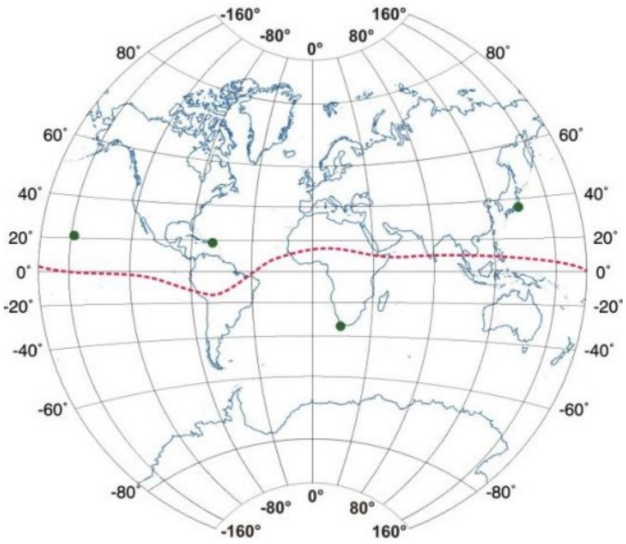

Figure 2.3 : Low -latitude observatories for Dst index measurement (http://roma2.rm.ingv.it/en/themes/23/geomagnetic_indices/27/dst_index)

The geomagnetic storms measured using Dst index overall consist of four phases (Figure 2.4) as follows.

1. The sudden storm commencement (SSC) / sudden impulse (SI) : the immediate rise of geomagnetic field strength due to magnetospheric compression by the interplanetary shockwave.
2. The initial phase : the geomagnetic field strength increases immediately and can last from minutes to hours. It is important to note that both the initial phase and SSC (or SI) are not always occure during the geomagnetic storm.
3. The main phase : the geomagnetic field is depressed and attributes to magnetospheric ring current enhancement due to energetic particles injection into the inner magnetosphere
4. The Recovery phase : the geomagnetic field relaxation linked to the ring current decay as a result of charge exchange with neutral exosphere.

The geomagnetic storm can be classified into three categories regarding the Dst values (Gonzales et al. 1994), i.e., small (Dst > -30 nT, typical substorm), moderate (-50 nT < Dst < -30 nT) and Intense (Dst < -100 nT).

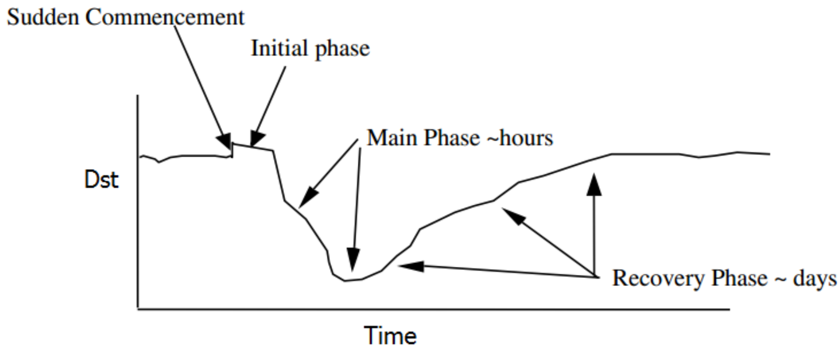

Figure 2.4 : The general phases of geomagnetic storm (Andriyas and Andriyas 2015)

During geomagnetic storms, the Dst index drops rapidly as the energetic electron flux increases substantially (Fennel et al. 2001). Several studies, such as Belov et al. (2005), pointed out that a large number of satellites in different groups were linked to geomagnetic storms through the Dst index. Pilipenko et al. (2006) also found a similar relationship between GEO anomalies registered in the National Geophysical Data Center databases in conjunction to Dst index variation. They noted that not all anomalies occurred precisely at the time the Dst index significantly dropped.

2.2.Low Energetic Particles

The rapid changes of geomagnetic field can affect the properties of plasma in space. A previous study showed that the charge buildup on satellites as a trigger of anomalies did not come from the magnetic perturbations rather than energetic electrons impacting satellite surfaces (Lam and Hruska 1991). The properties of energetic particles and plasma around Earth change in association with magnetic perturbations. In addition, some studies have shown that lower-energy electrons of <100 keV have fluctuated more strongly with geomagnetic variability compared to higher-energy electrons (Pilipenko et al. 2006; Choi et al. 2011).

As has already mentioned that the ring current enhancement is yielded by the energetic particles injection into the inner magnetosphere (Prolls 2004). The supperposition between gradient drift, i.e., charged particles motion through the discontinuous jump of magnetic field strength (weak and strong), and curvature drift, i.e., the bounce motion of charged particles along the curved magnetic field lines, leads to westward drift of proton and eastward drift of electron forming the ring current as illustrated in Figure 2.5.

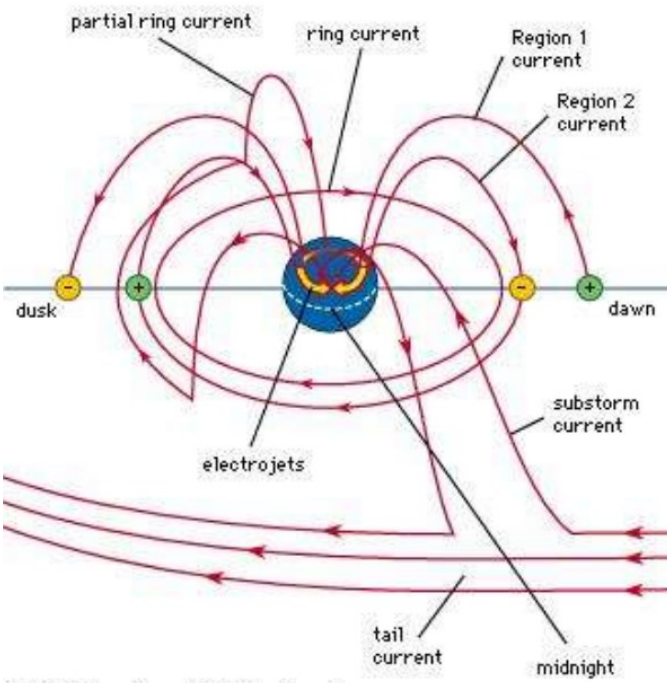

Figure 2.5 : The formation of ring current from injected particles into inner magnetosphere (https://www.britannica.com/science/ring-current).

The ring current region is believed as an occupancy of low energy charged particles, i.e., electrons (< 100 keV) and ions (1-200 keV). During magnetically disturbed condition, the density of particles raises up to ~ 10^6 particles/m^3 (Prolls 2004). The investigation done for some LEO satellites shows that the dynamic of low energy particles in ring current, through the Dst index, affects the satellite system failures (Ahmad et al. 2018). Several studies showed that the particles dynamic in this regime also has good agreement with satellite failures in geosynchronous Earth orbit (GEO) at ~36.000 km altitude (Dorman et al. 2005 ; Patil et al. 2008).

2.1. High Energetic Particles

High energy particles can penetrate the material surface of the spacecraft leading to internal charging. This phenomena is commonly related to higher particles energy, i.e., > 100 keV for electrons and 10 MeV for ions. The impact of high energy particles on Aluminium has been well studied and shown in Figure 2.6.

Mostly the high energy particles are scattered inside the radiation belt region confined to the inner magnetosphere. During magnetic storm events, these particles are accelerated into upper atmosphere with higher density. The failures on ANIK E1 and

E2 satellites on 20 January 1994 are believed to be linked to radiation belt particles (Horne 2001).

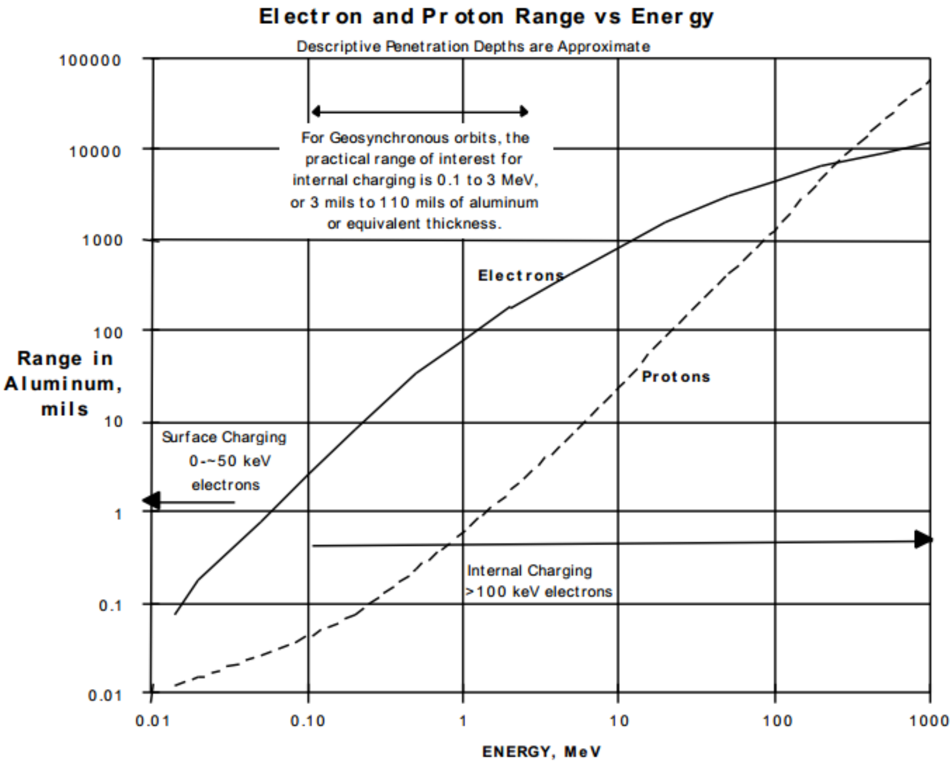

Figure 2.6 : The penetration depth of high energy particles in Aluminium (NASA 1999).

Chapter 3

Diagnosis of Spacecraft Failures

Many spacecraft have been launched into orbits, but ended up with failures before completing their mission. Various diagnosis have been progressively done to identify the source of failures. The study done by Tafazoli (2008) classified the spacecraft failures based on following categories, i.e., the impact on subsystems and mission, failure types, failure time, spacecraft power and mass distribution, component failures and the proportionality of environmental cause. However, difficulty arises due to some data are barely collected in each failure event. For example, we can usually access the failure time and brief description of failure only, but no detailed explanation about the component errors as well as the proximate cause of failure. Thus, the efforts to find the good method to identify the source of failure are progressively developed.

3.1. Methodology for Diagnosing of Spacecraft Failures

The failures on satellite can be initially detected when it is found such oddity on telemetry data than usual. As an unexpected behaviour observed on the telemetry data, investigation is done through series of analyses covering some possibilities, i.e., command error, mechanical and electrical surge, design/manufacturing flaw and environmentally induced electrical failures (Vampola 1994). The adapted methodology, after doing bit modification, can be seen in Figure 3.1

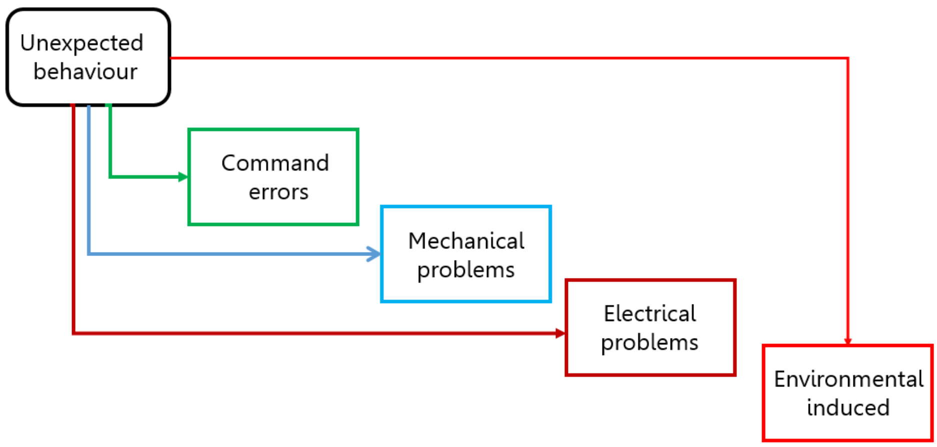

Figure 3.1 : The methodology for diagnosing failures on the spacecraft (adapted from Vampola (1994) with little modification)

There exists some salient points to be considered in diagnosing spacecrat failures as follows (Vampola 1994).

1. Spacecraft orbit and location at the time of failure
2. Magnetic variability around the failure time
3. Local time of failure
4. Space environment condition around the failure time
5. The detailed description of failure
6. The possibility of failure on other spacecraft at the same periode of time.
7. The track record of failures on the spacecraft

Overall, all above points have similar concept to that of proposed by Gubby and Evans (2002) with notion the industry can play role in diagnosing process through approvable design standard. In reality, it is barely quantify the failure due to complexity of conjoining all above considered points. In addition, the satellite telemetry data is sometimes discommoding to analyze, thus the failures are often linked to environmental condition.

3.2. LEO Satellite Failures Analysis

In this section, we discuss the diagnosis of the proximate causes of failure on LEO satellites recorded on the Satellite News Digest (SND) website (http://sat-nd.com) and evaluated their relationship with space environment variations during a specific period of time before and after the failure. The space environment was obtained primarily from low-energy electrons detected by the NOAA-15 satellite (http://satdat.ngdc.noaa.gov/sem/poes/data), as well as geomagnetic parameters represented by two indices called Kp and Dst (http://omniweb.gsfc.nasa.gov/form/dx1.html). We also determine the satellite local time (SLT) during which is crucial in failure diagnosis. To acquire the SLT, an important factor for anomaly diagnosis, we applied the Simplified General Perturbation-4 (SGP4) code to two-line element (TLE) data for each satellite obtained from Space-Track (https://www.space-track.org). All these steps enabled us to diagnose the relationship between low-energy electron fluxes and their associated magnetic perturbations with regard to their effect on LEO satellites.

3.2.1. Spacecraft Failures Database

A number of studies have examined failures on LEO satellites using various databases, such as Robertson and Stoneking (2003) and Belov et al. (2005). The former study used only a small number of LEO anomaly cases, whereas the latter study applied Kosmos data on anomalies attributed to high-energy particles. It is difficult to inventory the LEO satellite failure data exhaustively, since most failures are not very accessible. In this study, we used only Satellite News Data (SND) data (http://sat-nd.com) but excluded some failures attributed to space debris. Moreover, we also rechecked some SND data in terms of failure date and failure descriptions by confirming it through other sources and making adjustments.

Failure descriptions provided by the SND can be the initial step for failure diagnosis. The descriptions contain information about failure status, namely, partial loss, total loss, or contact loss, as well as which satellite subsystem sustained damage, such as solar array failure, power drop, or reaction wheel failure. Failure descriptions, along with the anomaly time, were used to construct the criteria to select LEO satellites for analysis. Some criteria used in this analysis were as follows. First, all failures due to space debris were ignored. Second, satellites were used only if the difference between the perigee and apogee of their orbit was less than 100 km or if their orbital eccentricity was almost circular. As a consequence, all LEO anomaly cases in this study are for satellites having orbits similar to that of the NOAA-15 satellite, which assures the relevance of the electron data used in this study.

Note that not all sources of LEO satellite failure used in this study were explicitly stated; thus, we presumed that the failures with unknown causes were associated with plasma variations triggered by geomagnetic disturbances. This is consistent with other studies, which attributed anomalies to environmental changes by default when analysis from telemetry data was infeasible (Vampola 1994; Gubby and Evans 2002). The LEO satellite failure cases used in this paper are listed in Table 3.1.

Some information in Table 3.1, such as altitude and inclination, are somewhat different from the existing data in SND. We preferred to use satellite orbital data from Space-Track, since it also provided the TLE data used for SLT calculation for each satellite. As previously mentioned, we attempted to confirm the anomaly day for each satellite and found that only the ICESat anomaly day had a discrepancy. ICESat was reported to suffer failure on March 29, 2003, around 9:58 a.m. (Eastern Time), when the Geoscience Laser Altimeter System transmitter stopped emitting laser pulses (Kichak

2011). Hence, in this study we preferred to choose the date reported by NASA for the ICESat anomaly. All other anomaly days were obtained from the SND database. We also found that two satellites, FUSE and Radarsat-1, suffered anomalies more than once. Therefore, the first failure are designated as FUSE (1) and Radarsat-1(1), and the second as FUSE (2) and Radarsat-1(2).

Table 3.1 : LEO satellite anomalies during the period 2000–2008 including brief description of failures.

No	Satellite Name	Anomaly Date	Alt. (km)	Incl. (deg)	Anomaly Description
1	ERS 1	10-Mar-00	772	98	total loss
2	ASCA	15-Jul-00	570	31	safe mode, total loss
3	Terra	26-Oct-00	702	98	telemetry Monitor error
4	FUSE 1	25-Nov-01	752	24	x-axis reaction wheel error
5	FUSE 1(2)	10-Dec-01	752	24	y-axis reaction wheel error
6	Yohkoh	15-Dec-01	575	31	loss of control
7	Aqua	27-Jun-02	702	98	single event upset
8	Radarsat 1	27-Nov-02	792	98	loss of attitude
9	Radarsat 1(2)	30-Dec-02	792	98	attitude control problem
10	Landsat 7	31-May-03	702	98	thematic Mapper failure
11	ICESat	29-Mar-03	595	94	one of three lasers aboard fails
12	Midori	24-Oct-03	805	98	total loss
13	DART	15-Apr-05	554	96	navigational errors
14	Monitor-E	18-Oct-05	527	97	loss of attitude control
15	Kirari	24-Nov-05	593	97	one of four reaction wheels fails
16	KOMPASS 2	29-May-06	422	78	various malfunctions
17	HST	30-Jun-06	564	28	ACS instrument fail
18	MetOp-A	4-Nov-06	821	98	temporary payload shutdown
19	Orbview 3	4-Mar-07	707	97	stops sending usable imagery
20	Orbcomm	10-Nov-08	758	98	satellite operation problems

3.2.2. NOAA-15/ MEPED Low Electron Data

The NOAA-15 satellite was launched on May 13, 1998, and placed at an altitude of 807 km with a polar inclination of around 98.8°. This satellite is equipped with Space Environment Monitor 2 instruments, such as a set of solid-state energetic particle detectors, called the Medium Energy Proton and Electron Detector (MEPED), to measure the flux of protons and electrons within an energy range of 30 keV to 200 MeV. To measure particles from different directions, the detectors are orientated in the zenith (0°) and horizontal/perpendicular-to-zenith (90°) directions, and these are referred to here as the 0° and 90° detectors, respectively; the MEPED also has omnidirectional detectors (Evans and Greer 2004), but these data were not used in this study. The MEPED instrument only measures the electron fluxes in three energy channels that span 30 to 2,500 keV. Since the electron detectors are also sensitive to protons, as shown in Table 3.2, all electron data must be examined and corrected to obtain better accuracy.

Table 3.2: MEPED electron energy channel detection and proton contamination ranges

Channel	Range (keV)	Contaminant range (keV)
E1	30–100	210–2700
E2	100–300	280–2700
E3	300–2500	440–2700

Table 3.2 shows the proton energy ranges at which each electron channel is subject to contamination by protons (CP) with energy range 210 to 2700 keV for E1 channel; The E2 electron channel is sensitive to protons over the energy 280 to 2700 keV; The E3 channel suffers from protons in the range 440 to 2700 keV (Evans and Greer 2004). Protons with energies in these ranges contaminate the electron detector channels and affect electron flux measurement. Thus, their effects must be removed from the data. Several methods can remove CP from electron data, as introduced by Lam et al. (2010), Rodger et al. (2010), Asikainen and Mursula (2013), and Peck et al. (2015). Since we only used short-term data over the 7 days straddling the anomaly day, the electron data were examined by comparing the flux variations between electrons and the CP within specific time intervals, as done by Tadokoro et al. (2007). When the trend of electron fluxes differed from proton fluxes, the electron data were regarded as contaminant-free.

Furthermore, we also adopted the method introduced by Rodger et al. (2010), in which the electron data are deemed to have acceptable quality if the electron flux in each energy channel is larger than two times the CP flux. We applied these methods for removing CP from electron channels for some anomaly cases, as shown in Figure 3.2.

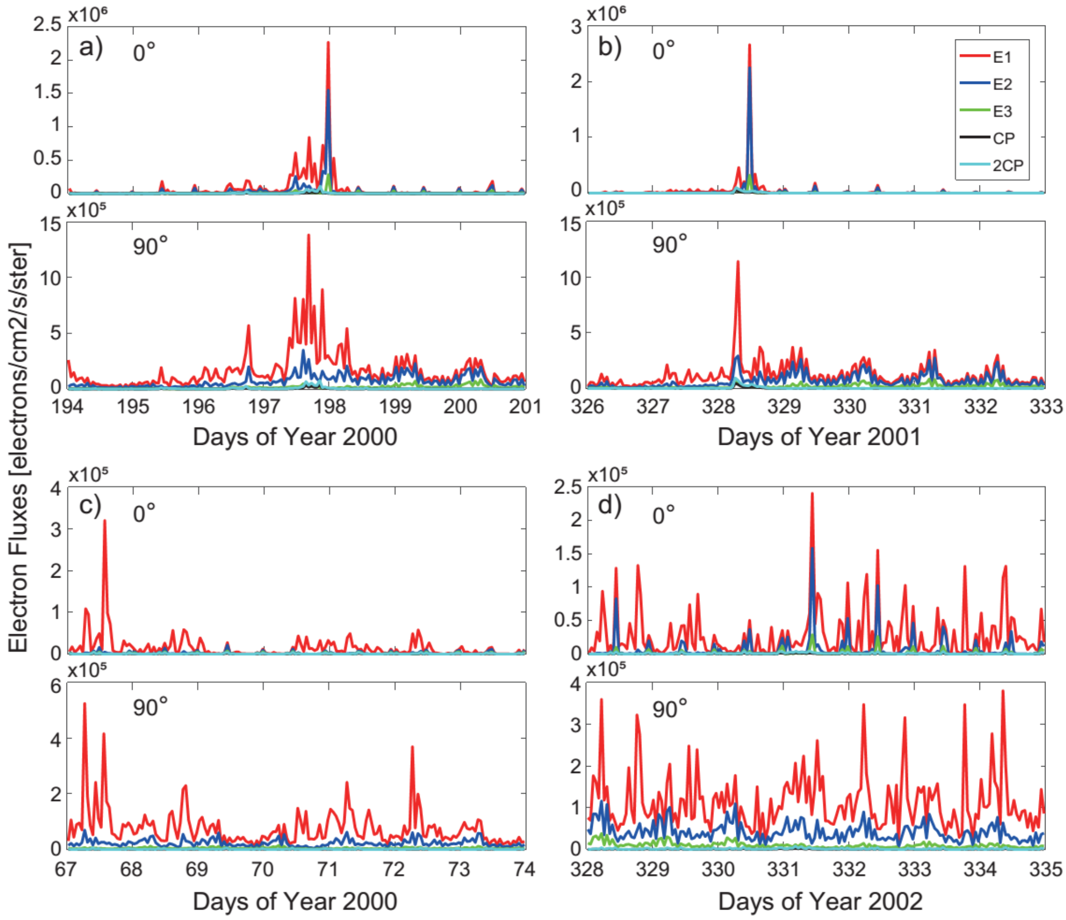

Figure 3.2 : Variation of electron and proton fluxes during the 7-day interval straddling the anomaly day on (a) ASCA, (b) FUSE (1), (c) ERS-1, and (d) Radarsat-1(1). The red, blue, and green curves represent electron fluxes for channels E1, E2, and E3, respectively, while the black and light blue curves indicate the variation of contaminating protons obtained from methods 1 and 2 in sequence.

Here we focus on the variation of electron flux during the 7-day time interval straddling the anomaly day for four cases: two equatorial satellites (ASCA and FUSE (1)) and two polar satellites (ERS-1 and Radarsat-1(1)). The other 16 cases are presented in the Appendix A. We used the hourly averages of electron flux to match the magnetic field data. Figure 3.2 shows the electron flux variations for channels E1 (red lines), E2 (blue lines), and E3 (green lines). The trend of CP on the electron fluxes is indicated by the black lines. It can be seen that overall the protons only affected a small portion of the electron flux data: day of year (DOY) 197-198 for ASCA (Figure 3.2a) and DOY 328-

329 for FUSE (1) (Figure 3.2b) for both the 0° and 90° detectors. Significant CP was not found in the other two cases (Figures 1c and 1d) in channel E1, whereas CP significantly affected the electron data in channels E2 and E3. Note that the CP did not occur exactly in conjunction with the increase of electron flux. The pattern of the peaks was totally divergent. The average of CP in the electron channels is obtained from the equation 3.1.

$$\frac{\overline{\Gamma}_p}{\overline{\Gamma}_e} \; x \; 100 \; \% \; \approx CR \tag{3.1}$$

where $\overline{\Gamma}_p$ and $\overline{\Gamma}_e$ are the average flux of protons and electrons, respectively, within the selected time interval and *CR* is the percentage of proton flux contamination in the electron channels. The rates of proton contamination for the same four anomaly cases are shown in Table 3.3.

Table 3.3: Proton contamination in each energy channel as a percentage of electron fluxes within ±3 days of the anomaly day for each case.

Channel	Proton contamination in 0°/90° detectors (%)			
	ASCA	FUSE (1)	ERS-1	Radarsat-1(1)
E1	3.3/1.5	4.9/1.7	2.2/0.7	1.6/0.7
E2	7.9/3.6	8.4/3.1	16.5/2.2	6.8/1.8
E3	33.9/16.2	39.5/11.7	37.1/10.9	28.2/7.5

The biggest CP occurred in channel E3 for both detectors and all cases. A higher energy corresponded to a larger CP. It seems that the magnitude of contamination is independent of satellite orbit. Data from both equatorial and polar satellites suffered similar magnitudes of CP.

To confirm that the electron data were usable, the second method was applied. The electron fluxes in each energy channel should be larger than two times the CP (called 2CP here) because one contaminant will result in one incorrect electron flux (Rodger et al. 2010). The 2CP values are indicated by the light blue curves in Figure 3.2. Here we can see that only electrons in channel E3 for both the 0° and 90° detectors were affected by CP. The increases of electron flux were followed by proton flux enhancement and their patterns were similar. The other channels, E1 and E2, were not totally affected by the contaminant. Based on this confirmation of usability, we removed the CP from the electron data using the aforementioned methods.

Particle data from the 0° and 90° detectors were used in this study for the following reasons. When the NOAA-15 satellite passes through a high-latitude region, the 0° detector measures precipitated particles, while the 90° detector counts trapped particles. Conversely, during low-latitude passage, the 0° detector measures trapped particles, while the 90° detector counts precipitated particles (Asikainen and Mursula 2008). Due to the orthogonal orientation of the detectors, we attempted to reconcile the electron data from both detectors to simplify the diagnosis process. In this study, reconciliation was done using the following steps. Firstly, hourly averages of electron data were selected from the 0° and the 90° detectors. Secondly, CP was removed from all electron channels in both detectors by deducting or subtracting the proton fluxes from the electron flux data. This subtraction was appropriate because one flux of contaminant will produce one incorrect electron flux (Rodger et al. 2010). This means that the presence of proton flux in electron detector will give rise incorrect measurement of electron flux, thus needs to be removed. In most cases, the electron fluxes were two times larger than the CP fluxes (except for channel E3), indicating the domination of electron flux in the electron detector. Since we used only short time intervals (7 days), the trend lines showed that the contaminant only affected a small portion of the electron data, such as on DOY 197-198 and DOY 328-329 in Figures 3.2a and 3.2b, respectively. Thus, not all electron data during the selected interval were significantly contaminated by protons, as seen in Figure 3.2. Thirdly, we calculated the magnitude or resultant of corrected electron flux data from the second step: $\Gamma_{corr} = \mathrm{sqrt}(\Gamma_{0deg.corr}^2 + \Gamma_{90deg.corr}^2)$, where $\Gamma_{0deg.corr}$ and $\Gamma_{90deg.corr}$ are corrected electron fluxes from the 0° and 90° detectors, respectively. These data were used with the magnetic field data to diagnose the anomalies on LEO satellites.

3.2.3. Relationship with Geomagnetic Variability

Geomagnetic data provide fundamental parameters for environmentally induced satellite anomaly research. These data, along with the energetic particle data, have been used to diagnose failures on LEO and GEO satellites. In this study, we use only the geomagnetic data represented by the Kp and Dst indices, since these data have shown good agreement with failure events, as seen in Belov et al. (2004), Patil et al. (2008), and Choi et al. (2011).

The Kp index is an indicator of global geomagnetic disturbance counted with a scale from 0 to 9. In general, a larger Kp index corresponds to more anomaly occurrences. Farthing et al. (1982) showed that anomalies on the GOES satellite series were clearly linked to Kp index values ranging from 1 to 6. Their finding showed that the overall tendency of anomalies increased with higher Kp. Fennel et al. (2001) also found that highly elliptical orbit satellite failures increased with increasing Kp. Furthermore, Choi et al. (2011) found that, although some GEO satellite anomalies were linked to lower Kp values, the number of GEO anomalies increased with increasing Kp.

The level of geomagnetic disturbance can also be indicated by the Dst index, which quantifies plasma changes in the ring current due to those disturbances. During magnetic storms, the Dst index drops rapidly as the energetic electron flux increases substantially (Fennel et al. 2001). Several studies, such as Belov et al. (2005), pointed out that a large number of satellites in different groups were linked to magnetic storms through the Dst index. Pilipenko et al. (2006) also found a similar relationship between GEO anomalies registered in the National Geophysical Data Center databases in conjunction to Dst index variation. They noted that not all failures occurred precisely at the time the Dst index significantly dropped.

In this study, a Dst index less than −30 nT (Gonzales et al. 1994) and a Kp index in the range of 3 to 9 were regarded as indicating a high level of geomagnetic activity. High levels of geomagnetic activities are generally associated with geomagnetic storms and substorms. In some events, the geomagnetic substorm occurs during the main storm phase (Wu et al. 2004) and can lead to partial ring current formation (Gonzales et al. 1994). The use of these bounds in this study is intended to simply identify the levels of geomagnetic activity in regard to anomaly occurrences. We also adopted the interval of 3 days before the anomaly day because Choi et al. (2011) found that a 3-day interval has a good agreement with the occurrence rate of anomalies. We appended a time interval of 3 days to see the characteristic environment after the anomaly day. Charged particles can remained in the satellite orbital path during the recovery phase of magnetic storms (Choi et al. 2011). Although Choi et al. (2011) focused on GEO satellites, we found similar features in LEO.

We initially examined the strength of geomagnetic disturbances affecting the properties of plasma in space. A previous study showed that the charge buildup on satellites as a trigger of anomalies did not come from the magnetic perturbations but rather from energetic electrons impacting satellite surfaces (Lam and Hruska 1991). The properties of energetic particles and plasma around Earth change in association with magnetic perturbations. In addition, some studies have shown that lower-energy electrons of <100 keV have fluctuated more strongly with geomagnetic variability compared to higher-energy electrons (Pilipenko et al. 2006; Choi et al. 2011). The first study used the Dst index in association with electron fluxes of >1 MeV and >2 MeV, whereas the latter applied the Kp index corresponding to electron fluxes of 50 keV to 1.5 MeV. Since the magnetic perturbations are believed to be indicative of plasma changes in space, we examined the relationship between both indices together with electron flux variations within the 7-day time interval. We first evaluated the relationship of Kp, Dst, and electron flux in each detector energy channel (E1, E2, and E3) and then identified the energy channel that was most strongly associated with magnetic perturbations represented by both indices. Note that the electron fluxes from all three channels have the same number of datasets for each event. Because we can access all magnetic data from https://omniweb.gsfc.nasa.gov/form/dx1.html, we preferred using the hourly averaged data for Kp and Dst and then adjusting the 1-hour resolution for electron flux data to match the resolution of the selected Kp and Dst data. The relationship of each energy channel is expressed by a correlation coefficient, designated as R, which can be seen in Figure 3.3 for the same four anomaly cases shown in Figure 3.2.

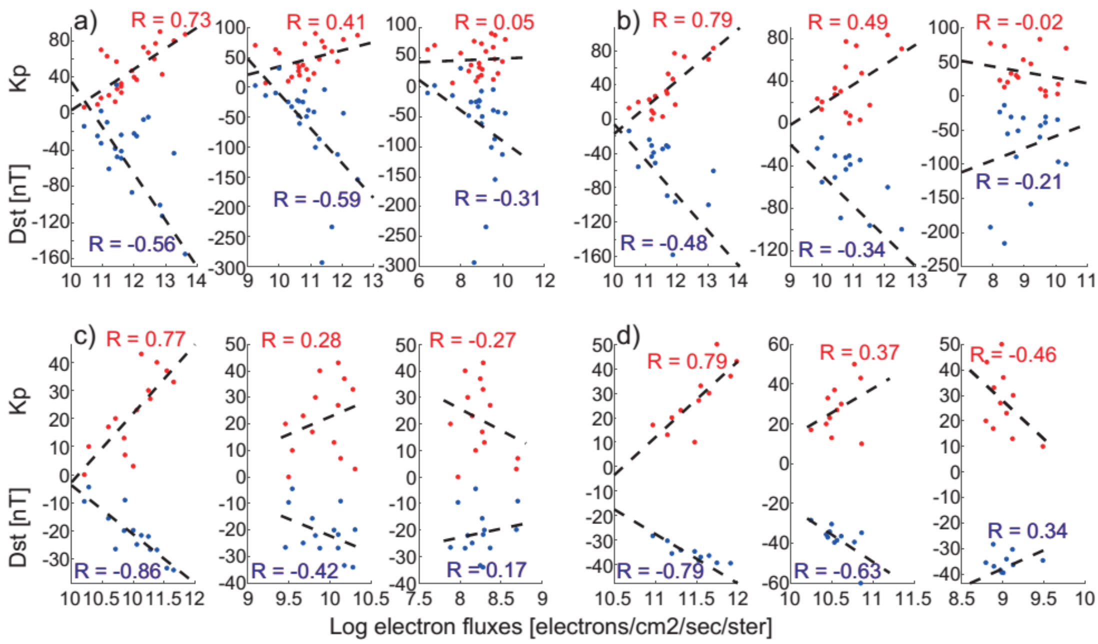

Figure 3.3 : Relationship between geomagnetic variability (Kp and Dst indices) and electron fluxes for channels E1 (left), E2 (middle), and E3 (right) around the day of anomaly for (a) ASCA, (b) FUSE (1), (c) ERS-1, and (d) Radarsat-1(1). The red and blue spots indicate the relationship with Kp and Dst data, respectively.

Since we adopted the 7-day interval, which is essentially short-term data, the images in Figure 3.3 were created by averaging all data points (Dst and E1, E2, and E3 data) corresponding to various Kp bins in intervals of 10: 0, 10, 20, …, 90. We then fitted the line for the averages of the bins, not for the entire dataset. The red spots indicate the scatter diagram for averaged Kp index bins, while the blue spots represent the scatter diagram for Dst index bins. The R values of each energy channel are given at the top and bottom of each panel. The R values make it obvious that the electrons with lower energy (E1) have a strong relationship with magnetic perturbations compared to those with higher energy (E2 and E3). This strong correlation is seen not only for the Kp index but also for the Dst index. Overall, R values for channel E1 are larger than those for channels E2 and E3. In this study, the Kp index value was multiplied by 10 (Kp × 10) for scaling purposes.

We initially expected that the correlation would be much higher during the period of solar maximum in 2000 and 2001, since the electrons trapped in the magnetosphere are related to solar activity (Lam et al. 2010). The anomalies ASCA, FUSE (1), and ERS-1 (Figures 3.3a, 3.3b, and 3.3c, respectively) occurred during the solar maximum. Geomagnetic disturbances occurred several times, as indicated by the Kp and Dst indices. For the anomalies in these three satellites, the maximum Kp index values were up to 9, 8.3, and 4.3, respectively, whereas the Dst index dropped to −300, −221, and −51 nT, respectively. We presumed that the relationship was not always individually consistent for every event due to the different datasets. Furthermore, high-level geomagnetic disturbances were not always followed by increased electron flux. A plausible explanation for the time lag between geomagnetic disturbance and electron flux enhancement ranging from hours to days is that it is driven by a mechanism such as radial transport diffusion or pitch-angle scattering (Tadokoro et al. 2007). However, the overall trend for each anomaly case shows that lower-energy electrons (>30 keV, channel E1) had a good correlation with Kp and Dst values, as shown in Figure 3.4.

In Figure 3.4, the *x*-axes represent a sequence of seven of the satellite failure cases listed in Table 3.1. Because the FUSE (2) and Yohkoh anomalies occurred within 5 days of each other, we merged their data for simplicity. Hence, in the diagnosis steps, both satellites were designated as case #5 (#5a for FUSE (2) and #5b for Yohkoh). In general, the correlation trend is consistent for each anomaly case, where R for E1 was larger than that for E2 and E3. Furthermore, the right panel shows the correlation with the Dst index, where for some cases the level of disturbance was less than −100 nT (intense storm), such as in case #4. For some events, such as case #14, no storm was present. We also note that electron flux has a negative correlation with Dst because the ring current energy containing electrons and ions is inversely proportional to the magnitude of Dst (Lohmeyer et al. 2012). Overall, the trend in Figure 3.4 shows that the majority of lower-energy electrons are highly responsive to geomagnetic disturbance. Hence, in the next section, we diagnosed LEO satellite anomalies using only lower-energy electron data (channel E1).

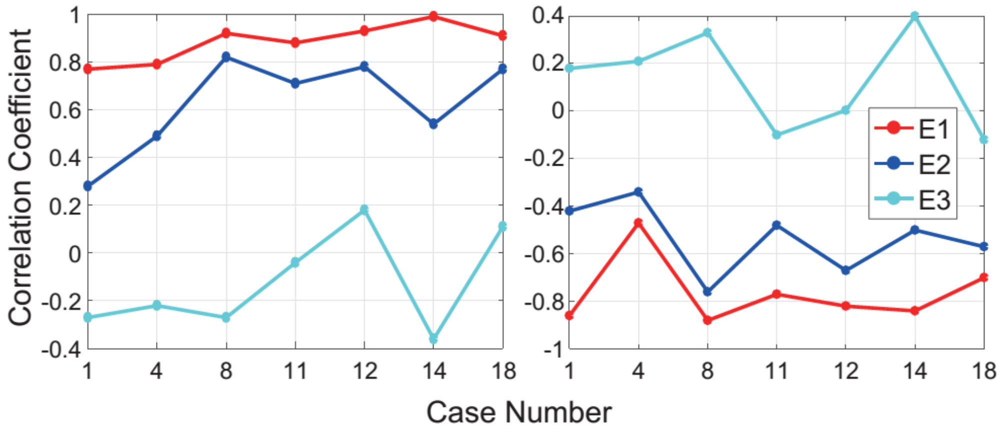

Figure 3.4 : Correlation coefficient between electron fluxes and (left) Kp index and (right) Dst index for channels E1 (red), E2 (blue), and E3 (light blue) for selected cases.

3.2.4. Environmental Failure Diagnostic

The satellite failure descriptions can provide clues for tracing the source of anomalies. The SND data used in this study did not contain any assertive statements that definitively identified the cause of any anomalies. In addition, our investigation to find the relationship between LEO anomalies and environmental changes was hindered by the limited amount of data. For example, we obtained only five anomaly cases for equatorial satellites, while the remaining cases involved polar satellites. Furthermore, the majority of anomalies were presented as technical failures, such as attitude loss and power drop, without identifying the cause of those conditions (such as environment, debris, or phantom command). The descriptions can be summarized as follows:

- ERS-1 operated for almost 9 years before being terminated by the European Space Agency due to failure in its attitude control system (ACS); no report about the cause of the ACS failure was prepared.
- ASCA (Astro-D) lost its attitude, and a power drop coincided with increased solar activity. Increasing incident solar radiation was suspected to impart torque to the satellite and increase its drag. Atmospheric drag strongly affects satellite

orbit, rather than onboard systems, so we concluded that the cause of this anomaly remains unknown.

- FUSE was reported to experience several reaction wheel failures in quick succession. Although it initially recovered, the third and fourth reaction wheels suffered damage several times until they failed completely in August 2007. No explanation of the failure cause is available.
- Radarsat-1 was discontinued by the Canadian Space Agency due to a deteriorating ACS. This satellite had previously suffered excessive friction and temperature in the primary momentum wheel in September 1999. Its back-up wheel suffered a similar problem in November 2002. No information about the cause of the anomaly is available.
- Midori-2 (ADEOS-2) switched to “light load” mode due to an unknown anomaly. The power level fell from 6 kW to 1 kW. It was presumed that there might be a relationship between the accident and solar flares. Further investigation is needed.
- Data for other satellites in the SND database, not presented in detail in this paper, also do not contain definite information about the causes of failures, so further study is needed.

Since we could not obtain much conclusive information about the causes of anomalies from the SND database or other sources (http://www.astronautix.com and http://spaceflight101.com/spacecraft/satellite-catalog/), we attributed these anomalies to environmental changes by default. As a first step, we traced the changes of environmental conditions using the Kp and Dst indices, as well as the electron flux data from channel E1, as shown in Figure 3.5.

In Figure 3.5, the left *y*-axes represent the magnitude of geomagnetic disturbance for both the Kp (red curves) and Dst indices (blue curves), while the right *y*-axes designate the electron fluxes for channel E1 (green curves). As already discussed, the lower-energy electrons (E1) were significantly correlated to magnetic perturbations. The day on which the anomaly was suffered is identified by the time interval inside the black dashed lines. The first two panels (Figures 3.5a and 3.5b) show data for equatorial satellites (ASCA and FUSE (1)), whereas the last two panels (Figures 3.5c and 3.5d) show data for polar satellites (ERS-1 and Radarsat-1(1)).

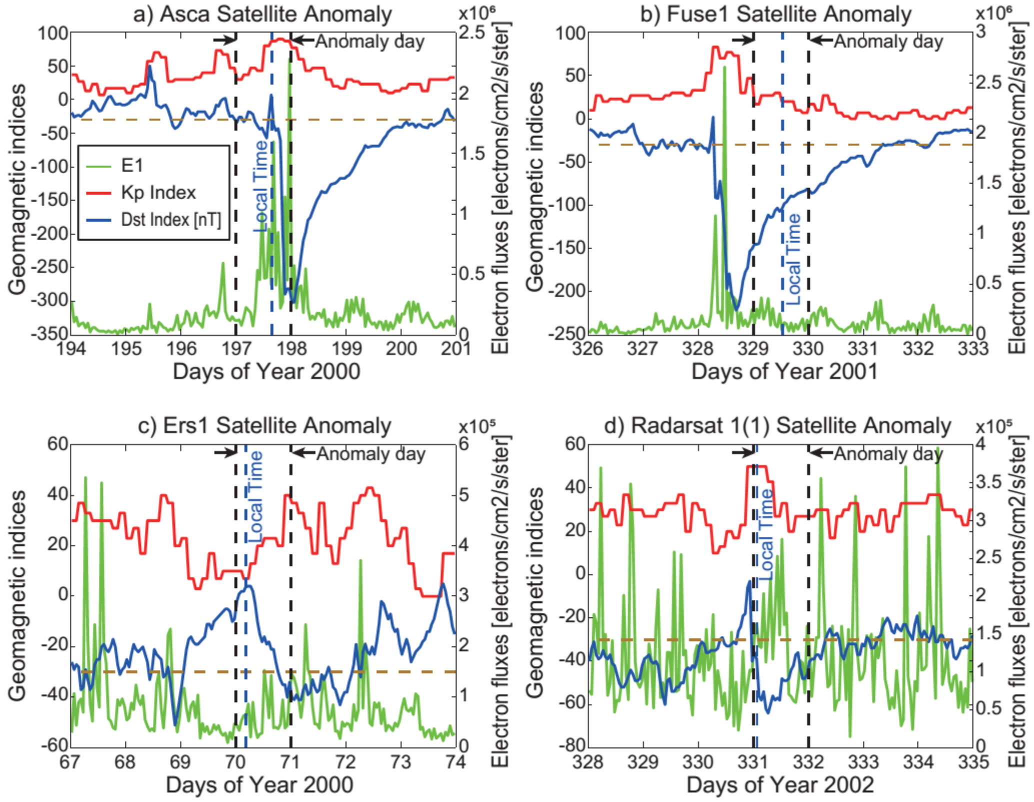

Figure 3.5 : Variation of electron fluxes and geomagnetic disturbances during the 7-day interval straddling the anomaly day for (a) ASCA, (b) FUSE 1(1), (c) ERS-1, and (d) Radarsat-1(1). The red, blue, and green curves are the Kp index, Dst index, and electron flux in channel E1, respectively.

It is of interest that the “peaks” of Kp and “valleys” of Dst do not occur simultaneously due to their different complex mechanisms. Sometimes, a time lag exists between two events. For example, in Figure 3.5a, the magnetic activity increased 2 days prior to the anomaly day (DOY 195), but a decline of Dst (down to -43 nT) was preceded by an increase of Kp (up to 6.3). We also found this pattern in other cases (see the Appendix A). The Kp index globally measured the magnetic activity at high geomagnetic latitude in which plasma in the magnetotail is heated and then transported earthward, whereas the Dst is measured at low latitude linked to ring current disturbances. We concluded that the time lag arose due to the difference in observation method. In addition, it was also probably related to the transport mechanism in which the energetic particles are firstly accelerated at high latitude and then transported and drifted into the ring current (Prolss 2004). The transport mechanism probably leads to measurement time lags between Kp and Dst. The existence of a time leg between Kp and Dst, especially at the peak of geomagnetic disturbances, affected the determination of satellite anomaly occurrences in association with Kp enhancement and Dst depression simultaneously. In some events, it was found that the anomaly had a good correlation with Kp, as shown in case #5b (Yohkoh, see Appendix A), whereas other events show that the anomaly was related to Dst, as in case #4 (FUSE (1), Figure 3.5b). Thus, the use of both indices in this paper increased our ability to associate anomalies with geomagnetic phenomena.

Previous attempts to link anomalies to magnetic activity, such as Fennel et al. (2001), showed that the majority of anomalies occurred during substorms, but not all substorms led to anomalies. During a geomagnetic substorm, a large number of energetic particles driven by solar wind interact with local plasma in the geomagnetic tail on the night side of the Earth, resulting in plasma configuration changes. The increased plasma energies from this process are injected toward the Earth through plasma sheets. Any satellites that cross these regions potentially experience charge buildup. Moreover, it has been well established that an increase of particle flux associated with magnetic activity occurred during a period of increasing anomalies (Welling 2010), but only 15% of anomalies occurred during magnetically disturbed conditions. In this study, we investigated LEO satellite failures in Table 3.1 using three patterns as follows.

1. Failure coincided with the main phase of a magnetic storm (pattern 1).
2. Failure occurred during the recovery phase of a magnetic storm (pattern 2).
3. High geomagnetic activities occurred during the 3 days before or after the failure day (pattern 3).

These patterns were used to evaluate failures on LEO satellites in this study. However, only 60% of failures (12 cases) fit one of the three patterns, while 40% (8 cases) showed weak correlation to magnetic variability. For the ASCA, FUSE (1), ERS-1, and Radarsat-1(1) failures in Figure 3.5, we found that all the above criteria were satisfied by these cases collectively, since magnetic storms, followed by an increase in electron flux, occurred prior to and up to the anomaly day. In Figure 4a (ASCA), a magnetic storm started on DOY 195 (Kp 7 and Dst −43 nT). It is clear that electron flux enhancement occurred gradually following the increase of Kp (~9) and decrease of Dst (~−289 nT) on the anomaly day (DOY 197). This occurred during the main phase of a magnetic storm (pattern 1). We did not see a significant time lag during this event, so we concluded that the activity was probably caused by the mechanism explained by Gonzales et al. (1994), in which a large injection of energetic particles from the magnetotail into the ring current and high-latitude region was proportionally constant.

It might be explained that the increased electron flux affected ASCA on the anomaly day, which coincided with increased Kp and decreased Dst.

In contrast to the ASCA case, case #4 (FUSE (1), Figure 3.5b) appears to have different features, where the anomaly occurred during the recovery phase of a magnetic storm (pattern 2). The disturbance of geomagnetic field strength occurred a few days prior to the anomaly day and was severe on DOY 328, 1 day before the FUSE (1) anomaly day. The maximum Kp was 8.3 and minimum Dst was −221 nT on DOY 328. We found that the time lag between Kp and Dst changes was insignificant, as in the ASCA case, so we presumed that energetic electrons were accelerated in the magnetotail plasma sheet and then transported into the ring current. The insignificant time lag between Kp and Dst changes for the ASCA and FUSE (1) anomalies confirm that both indices have good agreement with electron flux enhancement during periods of highly disturbed geomagnetic activity. We also found this pattern in other cases, such as cases #12 (DART) and #13 (Monitor-E) (see the Appendix A). While FUSE is an equatorial satellite and the other two satellites (DART and Monitor-E) are polar satellites, it seems that pattern 2 is independent of satellite orbit.

Pattern 3 was found in the ERS-1 anomaly (Figure 3.5c), where multiple storms occurred around the anomaly day, but the strongest was on DOY 68 (Kp 4 and Dst −51 nT) and then weakened to similar maximum Kp, but lower strength of Dst (~−35 nT) on the anomaly day (DOY 70). In general, the electron flux fluctuated in step with Kp variation, indicating that electron streams were injected earthward from the magnetotail and reached LEO with temporal fluctuation. For the Radarsat-1(1) anomaly in Figure 3.5d, several magnetic storms also occurred on DOY 329 (Kp 3.7 and Dst −60 nT) and became stronger on the anomaly day (Kp 5 and Dst -64 nT). A similar pattern was also found in other cases, such as Terra (#3), Yohkoh (#5b), Radarsat-1(2) (#8), Landsat 7 (#9), ICESat (#10), and Midori (#11) (see Appendix A). Most LEO failures in this study were associated with pattern 3.

It is interesting that no anomalies occurred prior to the reported anomaly day, since it is obvious that several magnetic storms occurred before that day, as shown in Figure 3.4 and the Appendix A. To explain this, we propose three scenarios:

1. Failures occurred with a time delay between storm occurrence and incoming electrons near the satellite, as seen in Figures 3.5b and 3.5c. This was also generally found in some anomaly cases studied by Farthing et al. (1982), Lam and Hruska (1991), and Iucci et al. (2005).

2. The link between LEO failures and environmental changes was weak in some cases, specifically #5a [FUSE 1(2)], #7 (Aqua), and #15 (Kirari) to # 20 (Orbcomm) in Table 3. Weak linkage was also found in GEO failures cases studied by Gubby and Evans (2002).
3. Failures were not promptly logged and documented by the satellite operator when the anomaly occurred. The anomaly occurrence was logged and documented several days after the event, resulting in an inaccurate local time for the anomaly. This evidence was found by one of the authors during analysis of some anomaly cases using unpublished data from a satellite operator.

Another interesting point is that we found that some anomalies occurred on the cuspate gradients, that is, where the curve of electron flux and Kp and Dst indices change steeply. This feature was also found by Gubby and Evans (2002). In Figure 3.5a, the sharp drop of Dst on DOY 197 indicated an abrupt change in electron streams, especially in the ring current. Electron flux fluctuated rapidly during this period. A similar pattern is seen in Figure 3.5c on DOY 70 and Figure 3.5d on DOY 331. Contrary to these cases, in Figure 3.5b, Dst clearly had a cuspate gradient on DOY 328, which was followed by increased electron flux, but the impact on FUSE (1) was delayed some time. Since several storms occurred prior to the anomaly day, it is still problematic which pattern precisely contributed to the failure.

It is an still open question which energies are primary contributors to satellite anomalies (Choi et al. 2011), but as a whole, the use of the lower-energy channel (30–100 keV, channel E1) is relevant in this study due to its sensitivity to geomagnetic disturbances, as demonstrated by the R values presented in Figure 3.3.

To support this relationship, we adopted a method used by Choi et al. (2011) to calculate the anomaly occurrence rate for LEO satellites. We selected the maximum Kp value, for example on the day of anomaly, for each anomaly case in Table 3. We counted the number of anomalies corresponding to each maximum Kp as well as the total number of days of maximum Kp within the period 2000 to 2008. The anomaly occurrence rate was obtained by dividing the number of anomalies by days for each maximum Kp. The same operation was also performed for 3, 2, and 1 days prior to the anomaly day. We found that the anomaly occurrence rate correlation coefficient (R) was highest on the day of anomaly, as shown in Figure 3.6.

In contrast to what Choi et al. (2011) found, where the 2-day window (3 days prior to anomaly day) had a good correlation with the Kp index, we found that the 0-day window (on the anomaly day) had higher correlation with Kp (R ~ 90%), as shown in Figure 3.6 (panel 4). We presumed that, in spite of orbital dependence, the correlation also varied case by case. Figure 3.6, especially panel 4, makes it obvious that overall a higher the Kp index corresponded to a higher the number of satellite anomalies.

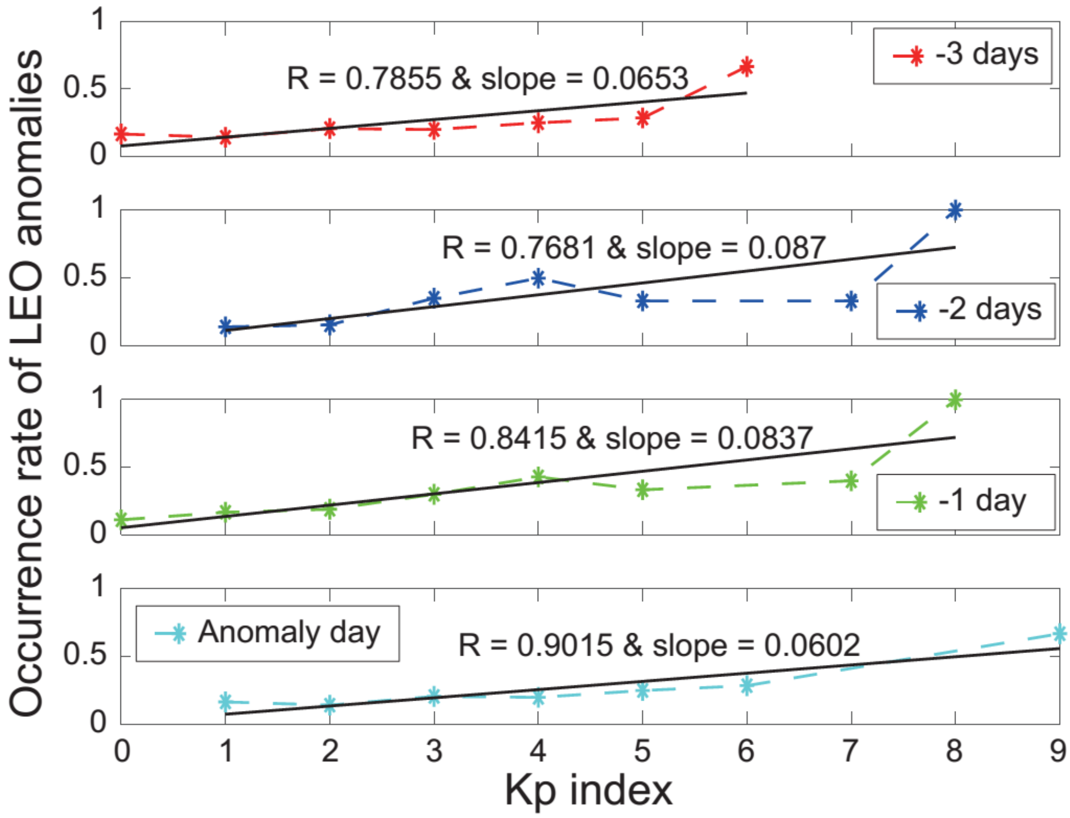

Figure 3.6 : LEO satellite anomaly occurrence rates: (from top) for 3 days (panel 1), 2 days (panel 2), and 1 day (panel 3) prior to the anomaly day and on the anomaly day (panel 4)

We have shown that there was strong relationship between electron flux in channel E1 and magnetic perturbations through Kp and Dst indices, for which average R values were around 75% and 60%, respectively (Figure 3.3). We have also demonstrated a strong relationship between the anomaly occurrence rate and Kp index, which was higher on anomaly days. Hence, we inferred that lower-energy electrons also play important role in satellite anomalies, primarily due to satellite charging (Fennel et al. 2001).

It is of interest that anomalies on the DMSP F6 and F7 satellites, at an altitude of 840 km, were linked to electrons with energies over 14 keV (Gussenhoven et al. 1985). They showed that the satellite potential was strongly related to the variation of electron flux with energies on the order of tens of kiloelectronvolts, which dropped to potential level of −462 V. Other simulations on the DMSP F13 satellite also found the same malfunction, called electrostatic discharge, which subjected the satellite to energetic electrons of 31.3 keV (Anderson and Koons 1996). We chose the low-energy electron channel (30–100 keV) in this study for the following reasons: it was sensitive to geomagnetic disturbances, as shown in Section 3.1; electron data from NOAA-15 are readily accessible; this energy range is partly attributed to surface charging (Anderson 2012) or internal charging (Fennel et al. 2001); and Lam et al. (2010) found that there was consistency of local time distribution between precipitation and injection of electrons (channel E1) in the nightside region due to a mechanism called whistler mode chorus waves resonance. Thus, the use of the lower electron channel in this study is appropriate for the diagnosis process.

3.2.5. Satellite Local Time (SLT)

The SLT is defined in many anomaly cases due to its connection with magnetic field fluctuations (Vampola 1994). The majority of anomalies, especially in GEO satellites, occurred during the midnight-to-dawn sector of magnetic local time. Its dynamical process has been described vividly by Vampola (1994) and Lai (2012). Since SND provided only a limited number of anomaly times, and mostly in Coordinated Universal Time (UTC), it is important to know the SLT because of its relationship to the migration of energetic particles due to magnetic perturbations. It is more complicated to find anomaly tendencies associated with SLT for LEO anomalies due to relative satellite position changes over time. However, we applied a method using celestial mechanics for this calculation, as shown in Figure 3.7.

Since the earthward injection of energetic particles from the magnetotail occurs on the nightside, we initially determined the relative position of a satellite with respect to the sun through the longitude of ascending node (LAN) parameter. This parameter indicates the longitude of a satellite in an equatorial plane eastward where the sun offset to that plane (Vallado and McClain 1997). The satellite reaches the ascending node at a particular SLT every day. The point here is that the calculation of SLT using LAN will not vary much due to the small nodal regression rate, which is less than 0.5° in our case or around 2 min/day (assuming that 1 solar hour is equal to 15°). Hence, although LAN oscillates, it does not affect the SLT variance significantly at an hour time scale. The SLT calculation was done only for satellite anomalies in Table 3 for which the SLT was not provided in the SND data. The anomaly times were provided in SND only for Aqua (1500 UTC), Midori (2349 UTC), HST (1234 UTC), and ICESat (0258 UTC). The last time was obtained from http://icesat.gsfc.nasa.gov/icesat/docs/IGARB.pdf.

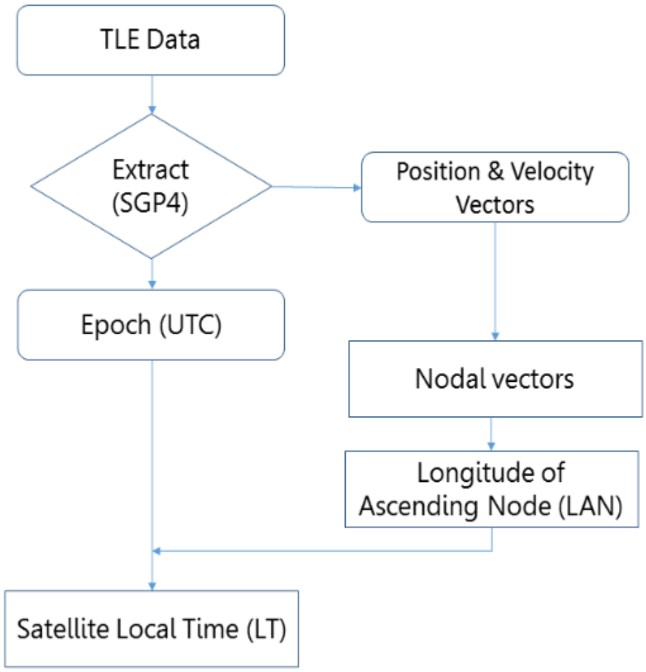

Figure 3.7 : Distribution of local time for LEO satellites within the day of failure

The TLE dataset from Space-Track is very important in this technique because it provides some orbital parameters. The use of TLE data corresponding to the anomaly day is the primary concern for the calculation. Detailed explanations of the TLE data are provided at www.space-track.org. For the first step, we extracted TLE data using the SGP4 code to obtain the position and velocity vectors of each satellite. The SGP4 is an orbital propagator that computes drag effects and estimates orbital parameters, as discussed in more detail by Vallado et al. (2006). Both position and velocity vectors are crucial for nodal vector calculations, as well as the satellite LAN, that is, the angle in the equatorial plane where the satellite crosses from south to north (Vallado and McClain 1997). In parallel, we can also derive the satellite epoch in UTC from the extracted TLE data. Both the LAN and epoch are then used to calculate the SLT for the anomaly. It is important to note that the SLT obtained from this method was the mean SLT when the satellite crossed the LAN on the day of the anomaly.

The vertical blue dashed lines in Figure 3.5 show the mean SLT for these four anomaly cases, as obtained from the above method using the extracted TLE data for the day of the satellite anomaly. Since the TLE data for satellites were mostly recorded during the ascending phase, the TLE epoch can be expressed as the time when the satellite passes through the LAN in the equatorial plane. Therefore, we can estimate the position of the satellite with respect to the local time sector (midnight, dawn, noon, or dusk).

As already discussed, discrepancies exist between the local time of magnetic storm events, increased electron flux, and anomaly occurrence on the satellite. We cannot always expect that satellite anomalies occur immediately as magnetic activity becomes very active. Figure 3.5b makes this evident: the FUSE (1) anomaly (DOY 329) occurred after the severest part of a magnetic storm (DOY 328). Hence, we assumed that time delays also existed for local times of anomalies in other cases. This time delay is probably also related to satellite position during magnetically disturbed conditions. For example, the time delay can be very short if the satellite is located near the ionospheric magnetic foot point where the substorm is initiated. Conversely, the time delay can be large when satellite is located in the ring current because buildup of the ring current takes hours or days. Moreover, the local time of anomalies in this study tended to coincide with the increasing phase of electron flux, as shown in Figures 3.5a, 3.5c, and 3.5d.

We then further examined the local times given in the SND database for Aqua, Midori, HST, and ICESat and compared them with the extracted TLE data used for the other cases. To convert the UTC into SLT, the LAN parameter and UTC are used together (SLT ≈ LAN/15 + UTC). Since most cases have very small nodal regression, the time resolution can be estimated at around 2 minutes. Table 3.4 compares the SLTs obtained by UTC conversion and calculation with extracted TLE.

Table 3.4: Comparison of mean SLT derived from SND and the extracted TLE for selected cases.

Case	UTC (SND)	Local Time		Difference
		SND Conversion	Extracted TLE	
#7 (Aqua)	1500	13:35:58	13:34:45	0:01:13 (-)
#11 (ICEsat)	2349	2:12:40	2:10:59	0:01:41 (-)
#12 (Midori)	1234	22:28:48	22:29:38	0:01:50 (+)
#17 (HST)	0258	2:52:32	2:51:42	0:01:50 (-)

We can see from Table 3.4 that the differences between the mean SLT obtained from the SND–UTC time conversion and that derived from extracted TLE are less than 2 minutes. The negative or positive sign in the bracket in the "Difference" column indicates whether the TLE-derived SLT was ahead or behind the actual local time. Since the time differences are less than 2 minutes, we concluded that the SLT calculation can be applied to the other cases for the diagnosis process. By taking into account the estimated time resolution for actual local time, that is, 2 minutes, we presumed that the time resolution of SLT obtained from TLE data extraction is approximately 4 minutes. Furthermore, we located the position of satellites in Table 3.3 during the failure day using propagated TLE data obtained from the SGP4 code. Thus, we obtained the latitude and longitude of satellites and then converted them into the geomagnetic frame using the converter at http://wdc.kugi.kyoto-u.ac.jp/igrf/gggm/. By taking the average period of satellites per orbit (Table 3.3) as around 90 minutes, we estimated the resolution of satellite position to be approximately 8°. Figure 3.8 summarizes the magnetic local time (MLT) sectors and approximate satellite locations on the day of their anomaly. The red spots represent the approximate locations of the corresponding satellites listed in Table 3.3 with respect to the geomagnetic frame.

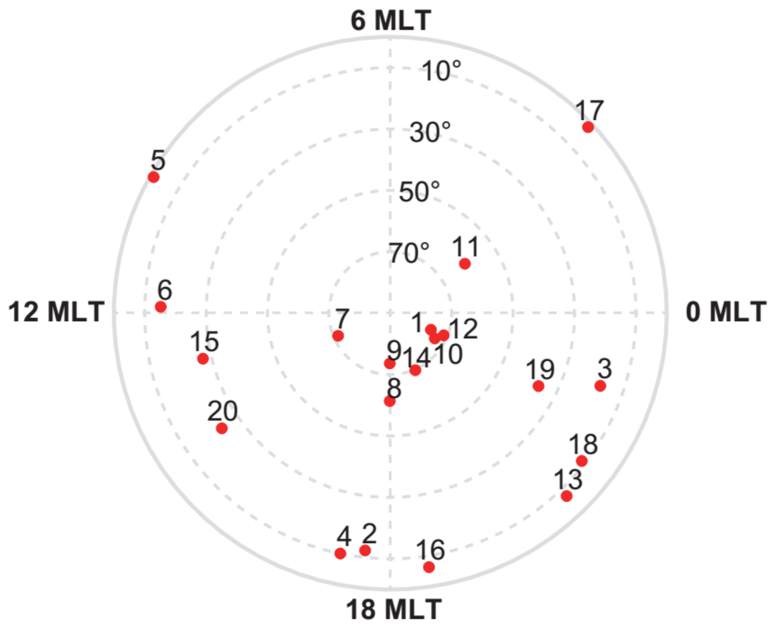

Figure 3.8 : Distribution of local time of LEO satellites within the day of failure

The largest numbers of anomalies appear in two sectors: the noon-to-dusk and dusk-to-midnight sectors. This pattern is similar to the pattern found by Lam and Hruska (1991), who found anomalies mostly distributed within the noon-to-dusk and evening sectors. As previously discussed, the time delay between magnetic storm and anomaly may explain why the magnetic local time of anomalies predominantly spreads out within the above two sectors. In addition, we also suggest that the anomaly occurrences in LEO are slightly different from those of GEO. During magnetic storms, the accelerated electrons and ions reach the GEO altitude at around midnight (Lai 2012). It is clear that the majority of GEO anomalies occurred from the midnight-to-dawn sector of MLT. In contrast to GEO satellite anomalies, overall the LEO satellite anomalies are affected by geomagnetic activity and the precipitation of electron fluxes in the upper atmosphere. Since the times of high geomagnetic activity and electron flux do not always coincide, we suspect that this leads to discrepancies in the local time distribution of LEO satellite anomalies. Note that the distribution of pre-midnight anomalies in Figure 3.8 seem to be related to scattered electrons associated with whistler mode chorus waves resonance (Lam et al. 2010), in which the wave intensities and the precipitating electron flux increase simultaneously when geomagnetic activity increases. Moreover, the pre-midnight pattern is probably also associated with monoenergetic electrons that are accelerated by the electric field or low-frequency Alfven waves (Wing et al. 2013). They showed that the aurora electron flux was predominantly distributed in the pre-midnight sector and that it dramatically increased after the substorm onset.

In addition, we compared the local time morphology using the anomaly cases in our study to what was found by Anderson (2012), which revealed the following:

- Our study: used multiple LEO satellites with different orbits (Table 3.3).
  Anderson: used a series of LEO DMSP satellites at the same sun-synchronous orbits (840 km altitude and 99° inclination).
- Our study: related LEO anomalies to lower-energy electron fluxes (30–100 keV) and magnetic perturbations (indicated by Kp and Dst indices).
  Anderson: Attributed anomalies to charging and used lower-energy electrons (30 eV – 31.3 keV).
- Our study: found that proximate local times of anomalies were mostly distributed from dusk to midnight (Figure 3.8).
  Anderson: found that local times of DMSP anomalies were spread out from dusk to midnight (Figure 3.9).

We can see from Figures 3.8 and 3.9 that the morphologies of the local time of anomalies have similarities, being distributed mostly within the dusk-to-midnight sector. This morphology varies depending on case, but both our study and the Anderson

(2012) study showed good correlation between LEO anomalies and lower-energy electrons.

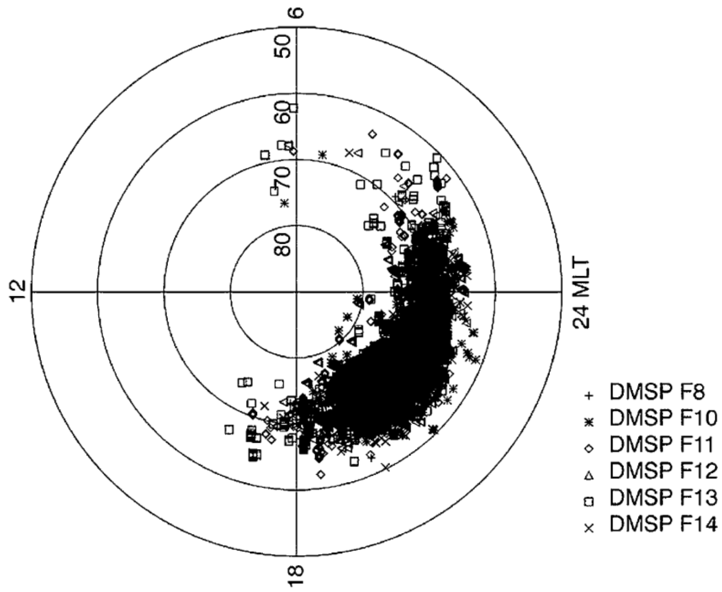

Figure 3.9 : Distribution of local time of LEO DMSP satellite anomalies (Anderson 2012).

As summary of this section, we have investigated the proximate cause of failures on LEO satellites and found that around 60% of failures in this study were strongly related to lower-energy electron fluxes of 30 to 100 keV, as well as associated magnetic perturbations through Kp and Dst indices. The failures tended to follow three patterns: occurred during the main phase of a magnetic storm (pattern 1), as suffered by ASCA (case #2); coincided with the recovery phase of a storm (pattern 2), as shown in FUSE (1) (case #4), DART (case #12), and Monitor-E (case #13); or attributed to multiple storms prior to and after the anomaly day (pattern 3), such as in Radarsat-1(1) (case #7), Terra (case #3), Yohkoh (case #5b), Radarsat-1(2) (case #8), Landsat 7 (case #9), ICESat (case #10), and Midori (case #11). We also noted that among these three patterns, LEO anomalies were mostly linked to pattern 3 (40%). For the remaining cases, such as FUSE 1(2) (case #5a), Aqua (case #7), and Kirari to Orbcomm (cases #14 to #19) in Table 3, it seems that the anomaly occurrences were weakly linked to the geophysical parameters used in this study. Nevertheless, we cannot say that the contribution of lower-energy electron fluxes and their associated geomagnetic disturbances did not play role in these cases. In particular, the failure on FUSE 1(2) (case #5a) resembled the FUSE (1) (case #4) malfunction, and it might represent worsening of the initial damage to the FUSE satellite.

The determination of SLT using the LAN parameter resulted in small deviations between local time derived from SND data and local time extracted from TLE data. The deviations were less than 2 minutes, as shown in Table 3.4. Although the LAN parameter changes over time, its oscillation per day is very small, resulting is discrepancies of minutes and seconds, but not hours (Table 3.4, column 4). Since this parameter can represent the position of the satellite relative to the sun, it is relevant for determining the mean SLT with respect to the sun in association with energetic particle injection in the nightside magnetotail.

It is obvious from Figure 3.8 that the local times of LEO failures were scattered primarily within two sectors: pre-dusk and pre-midnight. Since we intended to relate anomalies to the migration of low-energy electrons in the nightside of the magnetosphere, we inferred that LEO anomalies in this study predominantly occurred in the dusk-to-dawn sector of MLT (65% of occurrences). During geomagnetic disturbances, energetic electrons are accelerated in the magnetotail plasma sheet and drift into the ring current. A large portion of these energetic electrons, which have complex motions, are lost, precipitate into the upper atmosphere, and immerse LEO satellites in electron fluxes. This could be seen through flux variation in lower-energy channels as a result of magnetic perturbations represented by the Kp and Dst indices.

3.3. Spacecraft Failures due to Environmental Charging

It has been well investigated that the major contribution to spacecraft failures come from environmental charging (Rosen 1976). This finding is strenghthened by other investigation showed that charging is responsible for more than half (161 out of 299, Table 3.5) failures attributed to environment (Koons et al. 2000 ; Fennel 2001).

Table 3.5 : The number of failures according to diagnosis

Diagnosis	Number of failure	Total
ESD – internal charging	74	
ESD – surface charging	59	162
ESD - uncategorized	28	
Surface charging	1	
Others		137

It is obvious from Table 3.5 that charging becomes the major spectre of anomalous behaviour of the spacecraft performance and mission in space. Some satellites allegedly damaged subject to environmental charging can be seen in Table 3.6 (Koons et al. 2000).

Table 3.6 : Spacecraft failures attributed to environmental charging

Satellite	Failure date	Diagnosis
DSCS II (9431)	June 1973	Surface ESD
GOES 4	November 1982	Surface ESD
Feng Yun 1	June 1988	ESD
MARECS A	March 1991	Surface ESD
INSAT 2D	October 1997	Surface ESD

Electrostatic discharge (ESD) is one of charging types as a result of high energetic electron penetration into interior part of the spacecraft. A large number of electrons accumulation inside interior part can trigger induced electric field, through ESD, to imminent component or circuit (NASA 1999). It is of interest that approximated regions of concern for charging have been mapped as shown in Figure 3.10 (Evans et al. 1989). This map behaves as guideline for early design in space industry with notion it does not always result in high accuracy.

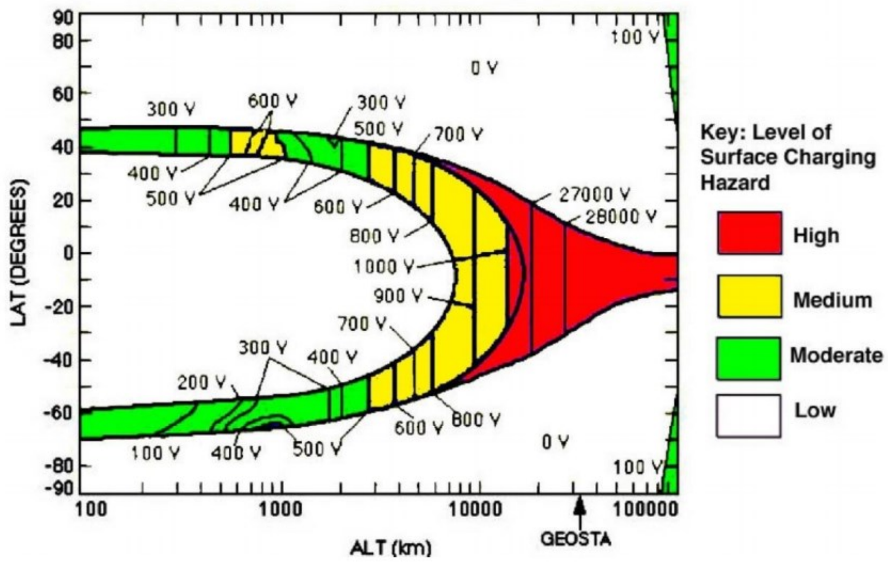

Figure 3.10 : Near-Earth regions of concern for surface charging hazards on spacecraft

Figure 3.10 depicts worst case surface charging scenario on the spacecraft made by Aluminium in shadowed area. Spacecraft placed above 400 km altitude can be exposed to charging around 400-500V giving rise to discharges. Particular investigation on

DMSP and ADEOS-II satellites showed this detrimental effects (Garret and Whittlesey 2012).

It has been well known that LEO satellite traversing auroral region can suffer significant charging due to the presence of high flux of energetic particles. The study done by Anderson (2012) presented statistical analyses of over 1600 DMSP satellite charging occurrences of which its electric potential dropped to less than -100 V. This study used DMSP charging data over a 12-year period. The most interesting finding in their study is there is no obvious correlation between peak energy of auroral electrons and frame charge. In one occasion, the peak of electron spectra of 31 keV results in charging around -100 V. On the other occasions , the electrons having peaks near 14 keV gives rise to high-voltage charging around 2 keV.

Chapter 4

Numerical Simulaton of Spacecraft- Plasma Interaction

In this section, we attempt to numerically simulate the electric potential faced by some LEO satellites as indicator of charging in addition to the wake structure behind the solid object using two conditions, i.e., in the absence of auroral electrons (unperturbed plasma) and in the presence of auroral electrons (perturbed plasma). The motivation is to see the behaviour of plasma around the solid object within aforementioned conditions in addition to the change of wake structure behind the object.

4.1.The Theory of Spacecraft Charging

Spacecraft charging is simply defined as charge accumulation on spacecraft surface (Pisacane 2008). A solid body in space can be charged by space plasma surrounding it giving rise to surface or internal charging. The level of charging, indicated by the object potential relatively to ambient plasma, depends on the currents balance incoming to/outgoing from the object surface as illustrated in Figure 4.1.

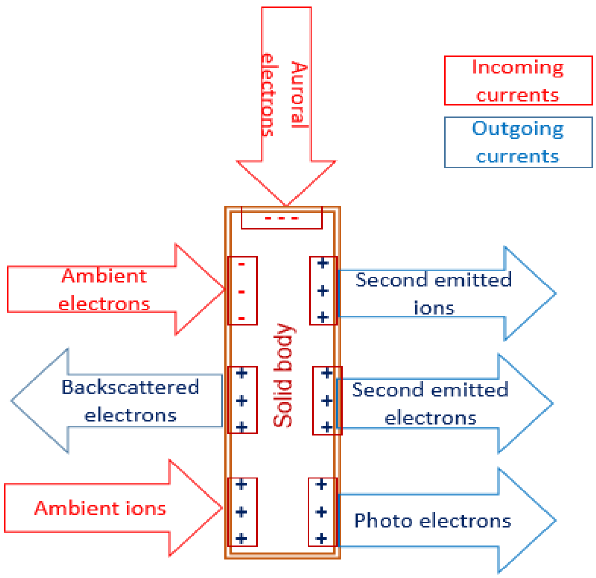

Figure 4.1: The currents balance inflow (red) and outflow (blue) of the spacecraft.

Incoming currents from ambient electrons ($I_e(\phi)$) as well as auroral electrons ($I_{ae}\ (\phi)$) lead to negative charging, whereas incoming ambient ion currents ($I_i(\phi)$) together with outgoing currents, i.e., backscattered electrons ($I_{bse}\ (\phi)$), photoelectrons ($I_{ph}(\phi)$), secondary emitted electrons ($I_{se}(\phi)$) and ions ($I_{si}(\phi)$), yield the positive charging on the spacecraft. The currents balance on the spacecraft are formulated through following equations.

$$I_t(\phi) = I_e(\phi) + I_{ae}(\phi) - I_i(\phi) - I_{bse}(\phi) - I_{se}(\phi) - I_{si}(\phi) - I_{ph}(\phi) \quad (4.1)$$

Here, $I_t(\phi)$ designates the total currents on the spacecraft surface. The net potential will be achieved under equilibrium condition, meaning $I_t(\phi) = 0$. Which currents (incoming/outgoing) are more dominant on the surface will drive the negative/positive potential relatively to its environment. The current from auroral electrons is usually obtained during auroral zone passage or in the course of geomagnetically disturbed condition. The photoelectron currents significantly contribute to charge buildup when spacecraft is more exposed to sunlight. In low Earth orbit (LEO) regime (altitude < 1000 km), the currents in equation (4.1) can be described as follows.

$$I_e(\phi) = J_{e0}A_e exp\left(\frac{e\phi}{kT_e}\right) \qquad \text{for } \phi < 0, \text{ repelled} \quad (4.2)$$

$$I_i(\phi) = J_{i0}A_i\left[1 - \left(\frac{e\phi}{kT_i}\right)\right] \qquad \text{for } \phi < 0, \text{ attracted} \quad (4.3)$$

$$I_e(\phi) = J_{e0}A_e\left[1 + \left(\frac{e\phi}{kT_e}\right)\right] \qquad \text{for } \phi > 0, \text{ attracted} \quad (4.4)$$

$$I_i(\phi) = J_{i0}A_i exp\left(-\frac{e\phi}{kT_i}\right) \qquad \text{for } \phi > 0, \text{ repelled} \quad (4.5)$$

$$J_{e0} = n_0\left(\frac{kT_e}{2\pi m_e}\right)^{\frac{1}{2}} \quad (4.6)$$

$$J_{i0} = -en_iV_{sc} \quad (4.7)$$

where

A_e = electron cross section area (m^2)

A_i = ion cross section area (m^2)

J_{e0} = ambient electron current density (A/m^2)

J_{i0} = ambient ion current density (A/m^2)

T_e = electron temperature (K)

T_i = ion temperature (K)

ϕ = electric potential (V)

n_0 = Initial ambient plasma densty ($/cm^3$)

V_{sc} = spacecraft orbital velocity (m/s)

Here, we approximate that the ambient plasma is maxwellian distribution in which the ion flow velocity is smaller that spacecraft velocity, thus the ion flow can be regard as orbital velocity of the spacecraft. Thus, the currents in equation (4.1) will invest the potential level through following equations , by taking into account only the ambient electron and ion currents.

$$I_t(\phi) = I_e(\phi) - I_i(\phi) = 0 \tag{4.8}$$

$$I_e(\phi) = I_i(\phi) \tag{4.9}$$

$$\frac{en_eA_e}{4}\left(\frac{8kT_e}{\pi m_e}\right)^{1/2} exp\left(\frac{e\phi}{kT_e}\right) = en_iV_{sc}A_i \tag{4.10}$$

Assuming that cross section area for electron 4 times than that of ion ($A_e \approx 4A_i$) and the density and temperature of electron are similar to those of ion ($n_e \approx n_i$, $T_e \approx T_i$), thus the potential can be expressed as follows.

$$\phi = \frac{kT_e}{e}\ln\left\{v_s\left(\frac{2\pi m_e}{kT_e}\right)^{-0.5}\right\} \tag{4.11}$$

In addition, in the presence of precipitating auroral electrons the currents onto spacecraft can be expressed through following equations. Here, we also consider that the auroral electron is maxwellian distribution.

$$I_{ae}\ (\phi) = J_{ae0}A_{ae}exp\left(\frac{e\phi}{kT_{ae}}\right) \tag{4.12}$$

$$J_{ae0} = n_{ae0}\left(\frac{kT_{ae}}{2\pi m_e}\right)^{\frac{1}{2}} \tag{4.13}$$

where $I_{ae}(\phi), J_{ae0}$, n_{ae0} are the current, current density and initial auroral electron density, respectively. The current balance equation by including the auroral electron impact can be written as follows.

$$I_t(\phi) = I_e(\phi) + I_{ae}(\phi) - I_i(\phi) = 0 \tag{4.14}$$

$$\frac{en_eA_e}{4}\left[\frac{8kT_e}{m_e}\right]^{1/2} exp\left(\frac{e\phi}{kT_e}\right) + \frac{en_{ae}A_{ae}}{4}\left[\frac{8kT_{ae}}{m_e}\right]^{1/2} exp\left(\frac{e\phi}{kT_{ae}}\right) - en_iA_iV_{sc} = 0 \quad (4.15)$$

It is important to note that the currents from ambient electron as well as auroral electron can be approximated as random thermal fluxes. It is because both species flow with thermal velocity much larger than the orbital velocity of spacecraft. On the other hand, the ion current can be regarded as directed flux due to its lower thermal velocity compared to spacecraft velocity.

4.2. The Plasma Wake Formation

In spite of charging on the spacecraft, it is also interesting to study the wake structure, another effect of spacecraft-plasma interaction, in the downstream side of spacecraft. The existence of plasma disturbance inside wakefield is believed to affect the performance or subsequent malfunction on payload behind the object. The wake forms due to spacecraft motion in plasma at which the spacecraft moves faster than ion thermal motion, but much smaller than thermal motion of electron, called mesosonic motion. The wake structure has been studied by Al'pert (1983) and describes some common features, i.e., momentarily behind the object where the density ratio of electron to ion is large; There exists focusing effect of charged particles depending on the potential of the object and the temperature ratio of electron to ion; the rise of concentration regions around the wake centerline at long-distance from the object. All above features also explained well by Hastings (1995). Furthermore, the analytical approach of the plasma flow around the object has been done by Wang and Hastings (1992).

The wake structure is not only studied through numerical simulation but also done through in situ experiment using small satellite such as probe mounted in the Explorer 31 satellite (Samir and Wren 1969). Another experiment regarding the wake structure has been done through CHAWS (Charge Hazards and Wake Studies) project flowing aboard STS-60 and STS-69 (Davis et al. 1999). This experiment used negatively biased object to characterize the current collection under charging environmental conditions. In summary, the experimental results showed the different in sheath expansions within the wake region between the highly negative biased object (< -100 V) and the object biasing few volt negative. Moreover, the current collection behaviour inside the wake region is orbit limited in which the ions are only deflected around the probe, depending their angular momentum.

4.2.1 The structure of Plasma Wake

In flowing plasma the ions flow supersonically because their kinetic (flow) energy ($E_{k,i}$) is much larger than their thermal energy ($E_{t,i}$). Conversely, the electrons flow subsonically since their thermal energy ($E_{t,e}$) is larger than their kinetic ($E_{k,e}$) energy. The speed ratio (S), the ratio between flow velocity (u) and thermal velocity (v_{th}) of plasma can be expressed as follows (Hastings 1995).

$$S = \frac{u}{v_{th}} \tag{4.16}$$

If S>>1, the plasma will behave supersonic motion, while subsonic motion can be considered as if S<<1. The presence of an object in flowing plasma gives rise to plasma disturbance that can change the trajectory of ions, depending on the object potential ($e\phi_{sc}$) relatively to kinetic energy of ambient plasma (Ek). If $e\phi_{sc}$ > Ek, thus the ion trajecory will be deflected by spacecraft potential leading to enhanced wake. On the contrary, if $e\phi_{sc}$ < Ek the ion trajectory will pass over the object as an obstacle (Engwall 2004) and the electrons will be repelled away by the object. In this condition, the electrons will be in Boltzmann distribution. The illustration of plasma flow over an object can be seen in Figure 4.2.

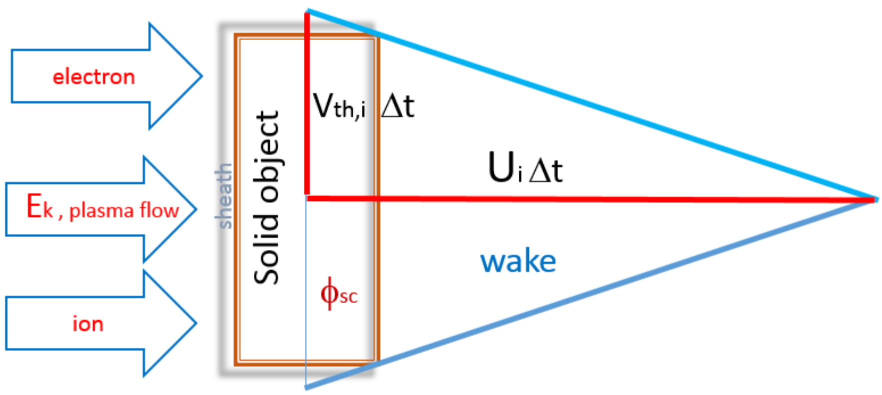

Figure 4.2: The ilustration of wake formation in flowing plasma around the solid object

Figure 4.2 describes collisionless plasma interaction with the solid object of which the mesosonic / mesothermal motion is satisfied. In LEO regime, due to lower thermal speed of ion compared to its drift/flow speed, there exists ion void region behind the object shown in Figure 4.2. This is because the ions need time to load this wakefield, whereas the mobile electrons, due to its subsonic motion, can penetrate deeper inside this wakefield.

It is important to point out that the presence of sheath around the spacecraft will affect the currents calculation onto the surface. The sheath forms due to disturbancase in plasma that breaks the quasineutrality. In equilibrium plasma, we assume that the numbers of free positive (e.g. ions) and negative (e.g. electrons) charge carriers are equal with different signs. When a solid object immersed in plasma, this quasineutrality is violeted due to potential of the object. The region over which this quasineutrality is violeted due to object potential is simply called as sheath. The sheath formation can be easily illustrated through Figure 4.3 (Lieberman and Lichtenberg 1994).

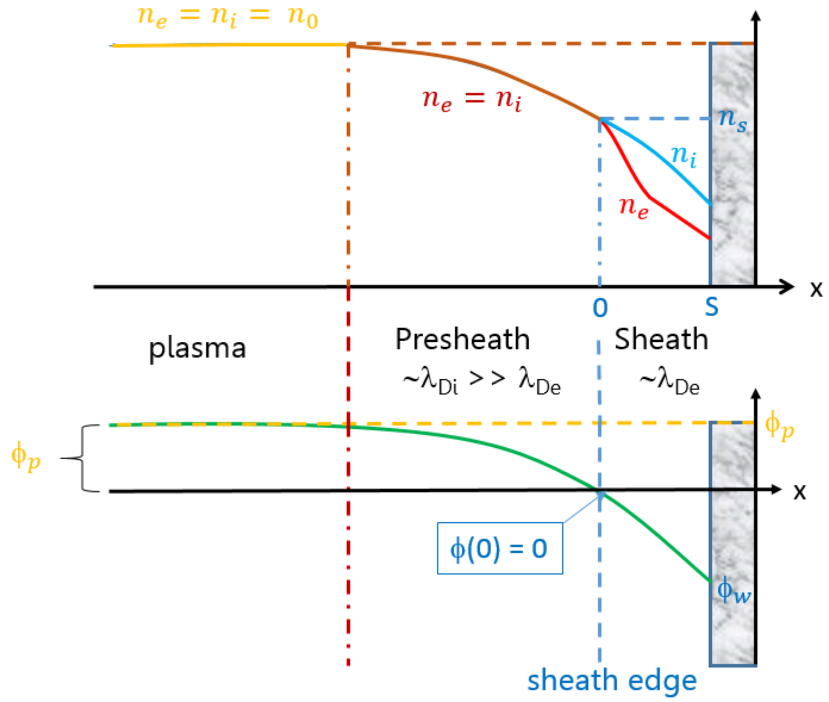

Figure 4.3: The ilustration of sheath formation around the solid object.

Since the ambient electrons and ions overtake the object with thermal and orbital velocities, respectively, the high thermal velocity of electron will yield potential of the object lower than that of ambient plasma to gratify the flux balance. As the plasma flows toward a solid object, according to Boltzmann relation ($n_{e,i} = n_0 e^{\phi(x)/T_{e,i}}$) the density of electrons and ions decreases compared to initial plasma density ($n_0 \neq n_e \approx n_i$). This gives rise to zero potential ($\frac{d^2 \phi}{dx^2} = \frac{e}{\epsilon_0}(n_e - n_i)$) at point x = 0 (sheath edge). At this point, the ion velocity (u_s) can be approach as Bohm velocity (u_B) where $u_s \geq u_B = \left(\frac{eT_e}{M}\right)^{\frac{1}{2}}$. The directed velocity of ions (u_s) in this sheath edge only happens in the presence of finite electric field at particular region in the plasma, called presheath. The presheath region is typically larger than sheath region and the electric field here is overall small. The flow of plasma in presheath is approximately subsonic ($u_i < u_B$). As the ions cross the sheath edge, their flow velocities turn out to be supersonic and the charge neutrality is then violeted. The acceleration of ions to be the Bohm velocity in the presheath is caused by the decrease in potential ($\frac{1}{2}M{u_B}^2 = e\phi_p$; ϕ_p plasma potential).

In order to understand the effect of sheath in calculating the charging on a solid object immersed in plasma, there exists two approaches, i.e., thin-sheath and thick-sheath approximations. Thin-sheath approximation is applicable for case, e.g. LEO regime, where the Debye length (λ_D) is relatively smaller than or comparable with spacecraft length/radius (L), whereas thick-sheath approximation is appropriate for case where λ_D > L such as in geosynchronous Earth orbit (GEO) regime.

4.2.2 Particle-In-Cell Code of EMSES

The Particle-in-Cell (PIC) The PIC method is broadly utilized in analyzing various microscopic phenomena in space plasmas. It has effectively solved the interaction between charged particles and the solid body especially in space. The PIC method describes a mini laboratory of space which consists of large number of macro charged particles, interacting each other under the influence of electromagnetic or electrostatic field. The use of PIC method hitherto focuses mainly on deriving the steady-state and electrostatic solutions (Miyake and Usui 2016). To get a comprehensive picture of trancient and electrostatic processes of interaction which exist in space, it is needed to develope a tool that covers both phenomena where its scheme can be seen in Figure 4.4 (Miyake and Usui 2016).

EMSES is developed to overcome the aforementioned issues. Here, the spacecraft as inner boundaries is assumed as a conducting body at which the incoming or outgoing particles interact with it. In EMSES, the plasma is modeled as collection of superparticles distributed in certain volume and governed by the equation of motion. Their velocities are updated using Buneman-Boris scheme (Birdsall and Langdon 1985). Furthermore, the electromagnetic field defined at grid points is solved by Maxwell's equation solvable through finite-difference time domain (FDTD) method. Inside the simulation domain the fields are maintained at the grids, whereas the particles randomly move under the influence of the fields. In addition, the current density, J, in Maxwell's equation is derived through the charge flux, ρv, calculated at the particle positions to contiguous grid points (Miyake and Usui 2009). The field, together with the particle dynamics, is updated self-consistenly using the scheme shown in Figure 4.4.

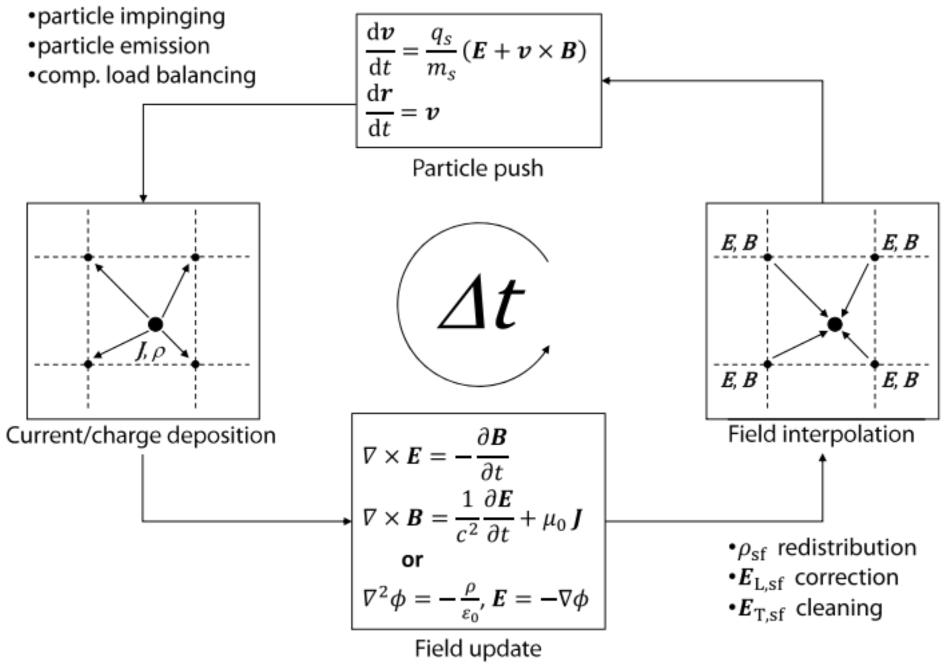

Figure 4.4: The scheme for updating the field and particle dynamics in EMSES

Since the spacecraft is treated as a perfect conducting body, its surface or geometry, represented by several grids in Cartesian cordinate system, is set along grid line where the electric field components are defined. The particles bombardment is assumed to occur at time of particles get inside the spacecraft surface and it occures at very short time (Δt). The particles are assumed to be absorbed inside the body at time larger than Δt. In this state, the absorbed particles resides on the surface giving rise to the induced electric field. The implementation of EMSES to describe the plasma and spacecraft interaction can be seen in next chapter.

4.3. Numerical Simulation Setup

We first selected the parameters for two species, i.e., ambient electron and ion distributed in polar and equatorial environment for LEO satellite cases in Table 3.1. These parameters delineate ionospheric condition at time LEO satellite passes through high latitude and low latitude regions giving rise to anomaly or failure as presented in chapter 3. We then employed following assumptions, i.e., the spacecraft position is relatively fixed in the frame and the ionospheric plasma isotropically flows with respect to the spacecraft; the temperature of electron and ion is chosen during disturbed ionosphere; the satellite is box-shaped with dimension 12 x 12 x 36 cm at the center of a computational box shown in Figure 4.5.

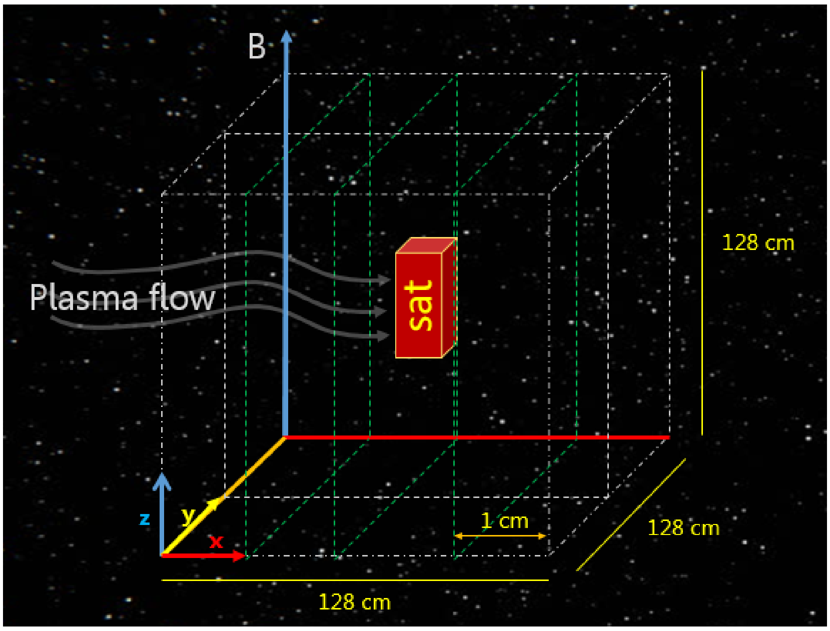

Figure 4.5: The model of simulation box for the spacecraft - plasma interaction.

We set the direction of the magnetic field is perpendicular to the direction of spacecraft motion which is in +z direction shown in Figure 4.5. We employed the magnitude of magnetic field around 27μT obtained from National Oceanic and Atmospheric Administration (NOAA) in https://www.ngdc.noaa.gov/geomag-web/#igrfwmm.

The simulation was run by using following numerical parameters, i.e., the number of grids in each side of the simulation region is 128 (Nx, Ny, Nz); integration time step is 10^{-9}s (10^3 ps) with 5.10^3 iterations in total; the grid size is 1 cm which is less than the average Debye length of 1.3 cm. In addition, the plasma flows along x direction with angle of attack perpendicular to spacecraft surface. The results of simulations can be seen through following sections.

4.4. Overview of Charging and Wake Structure in Ionospheric Plasma

As has been previously mentioned that the mesothermal motion of plasma in ionosphere gives rise to supersonic motion of ions and subsonic motion of electrons. We have performed simulations for 20 polar/equatorial LEO satellite cases ranging from 400 to 900 km altitude. Some input parameters used for EMSES simulation can be seen in Table 4.1.

Parameters such as plasma density and temperature of electron and ion are chosen on the day of failure on satellite. In EMSES simulation, we preferred to use the major composition of ion which varies in each case. For instance, to perform the simulation between ERS 1 satellite and ionospheric plasma the major composition of ion at this altitude comes from Oxygen, thus we employed the Oxygen ions in terms of its mass ratio with electrons (m_i/m_e) in this simulation. On the contrary, in Orcomm 1 simulation, the major composition comes from Hydrogen ion, thus it is more appropriate to describe the form of interaction rather than Oxygen ion.

Table 4.1: The plasma parameters employed for EMSES simulation.

Satellite Name	Failure date	Major composition (%)		Temperature (K)		Plasma density,	Altitude (Km)	Orbit Class.
		O_ion	H_ion	e^-	p^+	N (m^{-3})		
ERS1	10-Mar-00	89.0	6.4	1458.2	1103	1.4853E+11	787	polar
Asca	15-Jul-00	97.4	0.0	1974.1	1261.3	3.1720E+11	473	equatorial
Terra	26-Oct-00	80.3	14.4	1234.9	1052.9	1.1085E+11	703	polar
Fuse1	25-Nov-01	90.0	5.8	2321.6	1670.1	1.6037E+11	754	equatorial
Fuse2	10-Dec-01	90.0	5.8	3364	1966.8	7.8388E+10	754	equatorial
Yohkoh	15-Dec-01	97.3	0.3	1289.1	1179.1	4.4721E+10	543	equatorial
Orbcom1	10-Nov-08	3.6	94.3	1345.0	1176.3	2.3776E+09	759	polar
Aqua	27-Jun-02	72.7	22.1	2116.3	1472.9	4.6687E+10	704	polar
Radar1	27-Nov-02	36.7	58.7	1041.9	985.4	5.7851E+10	797	polar
Radar2	30-Dec-02	37.8	57.5	1262.0	983.8	7.0541E+10	797	polar
Landsat 7	31-May-03	81.5	15.1	1745.3	1684.4	1.1710E+11	704	polar
Icesat	30-Mar-03	96.1	0.2	2473.8	1714.9	1.7439E+11	601	polar
Midori	24-Oct-03	91.2	4.1	1988.7	1562.7	7.8485E+10	812	polar
Dart	15-Apr-05	93.1	2.2	2608.8	1703.5	5.8956E+10	549	polar
Monitor E	18-Oct-05	8.4	88.3	1032.2	878.5	3.9526E+10	746	polar
Kirari	24-Nov-05	23.4	72.7	913.1	842.0	2.0205E+10	604	polar
Kompass 2	29-May-06	96.4	0.5	2454.7	1474.0	7.5408E+10	425	polar
HST	30-Jun-06	89.4	6.9	1007.0	1005.9	4.8627E+10	564	equatorial
Metop A	4-Nov-06	65.6	27.3	2299.5	1918.6	4.7387E+10	827	polar
Orbview 3	4-Mar-07	94.7	3.0	2656.0	1050.0	1.0424E+11	457	polar

The simulation results showed that overall the symmetric wake formed behind the object. Here, we only presented the distribution of ambient electrons and ions for satellite in polar environment, e.g. ERS 1 satellite (case #1 in Table 4.1), and equatorial environment, e.g. ASCA satellite (case #2 in Table 4.1). In general, there is no significant difference between polar and equatorial region in terms of wake formation in the downstream region of solid object shown in Figure 4.6. The spacecraft position in Figure 4.6 is denoted by white square. The electrons and ions scattering are shown through the left and right panels of Figure 4.6, respectively.

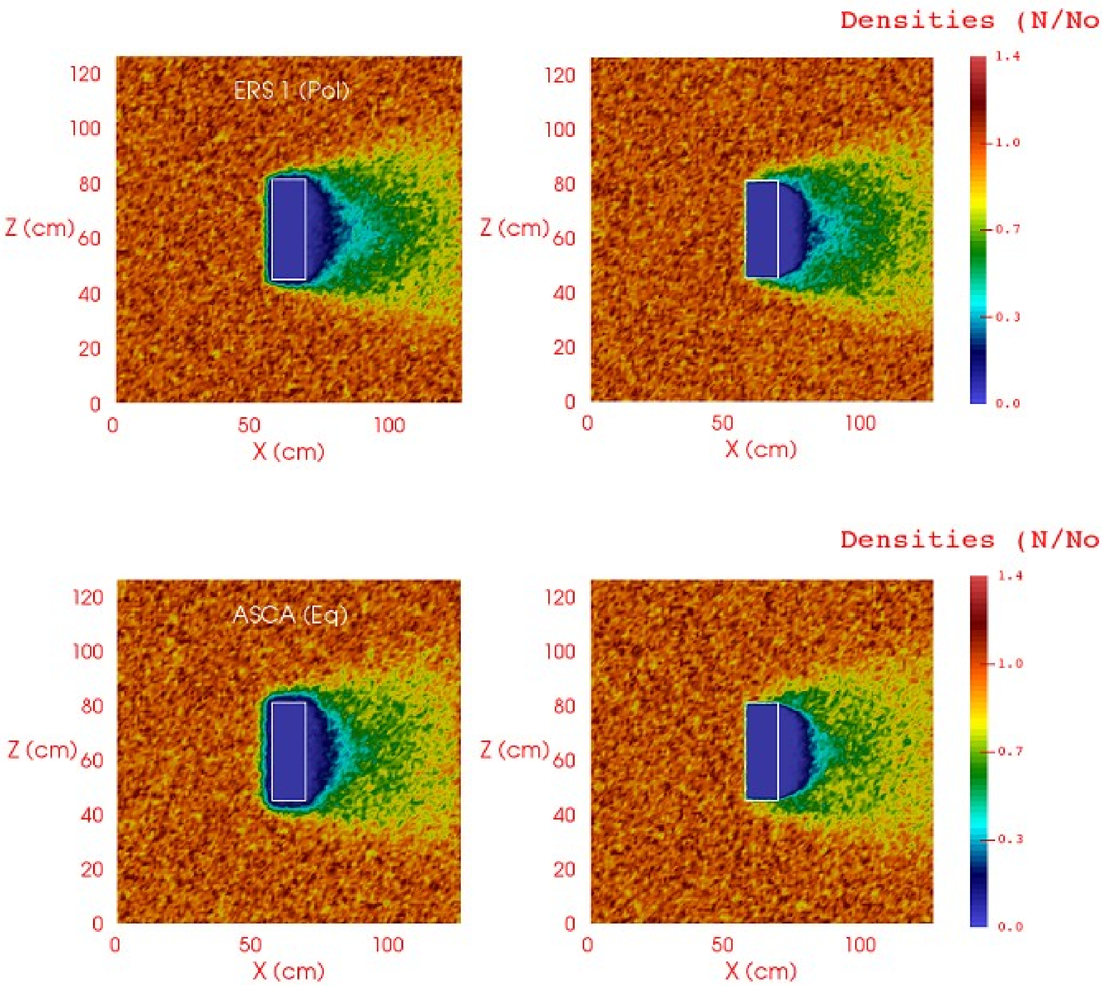

Figure 4.6: The electrons (left) and ions (right) scatterings in the vicinity of spacecraft in polar (upper) and equatorial (lower) regions. The density of electrons and ions (N) is normalized with initial ambient plasma density (No).

We attempt to look up the wake structure at direction of horizontal (parallel to spacecraft motion) and vertical (perpendicular to spacecraft motion) for polar and equatorial satellites shown in Figure 4.7. Here, the distribution of electrons and ions is represented by the red and blue lines, respectively. It is important to note that in this simulation the potensial of ASCA satellite is around -1.4 V, whereas ERS 1 potential is around -0.97. The lower potential of ASCA satellite gives rise to shifted ion void region closer to the object compared to that of ERS 1 case. It can be interpreted as the more negative potential of an object the more ions will be attracted in the donwstream side of the object. This is the common feature of wake structure of ambient plasma in LEO environment. In addition, the more attracted ions in ASCA are also seen in the left panel of Figure 4.7. Here, the curves of wake structure (green lines) are taken along z = 80 cm (~7.7 λ_D) behind the object. Moreover, it is clear that density of electrons and ions decreases monotonically toward the wake centerline at x = 64 cm.

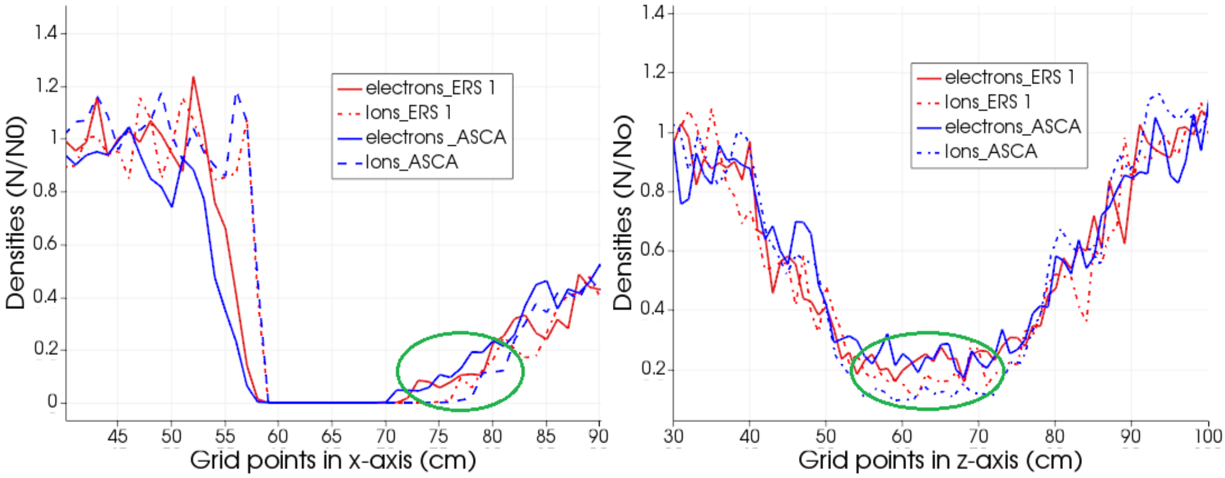

Figure 4.7: The wake structure parallel (left) and perpendicular (right) to spacecraft motion for polar (solid lines) and equatorial (dashed lines) satellites.

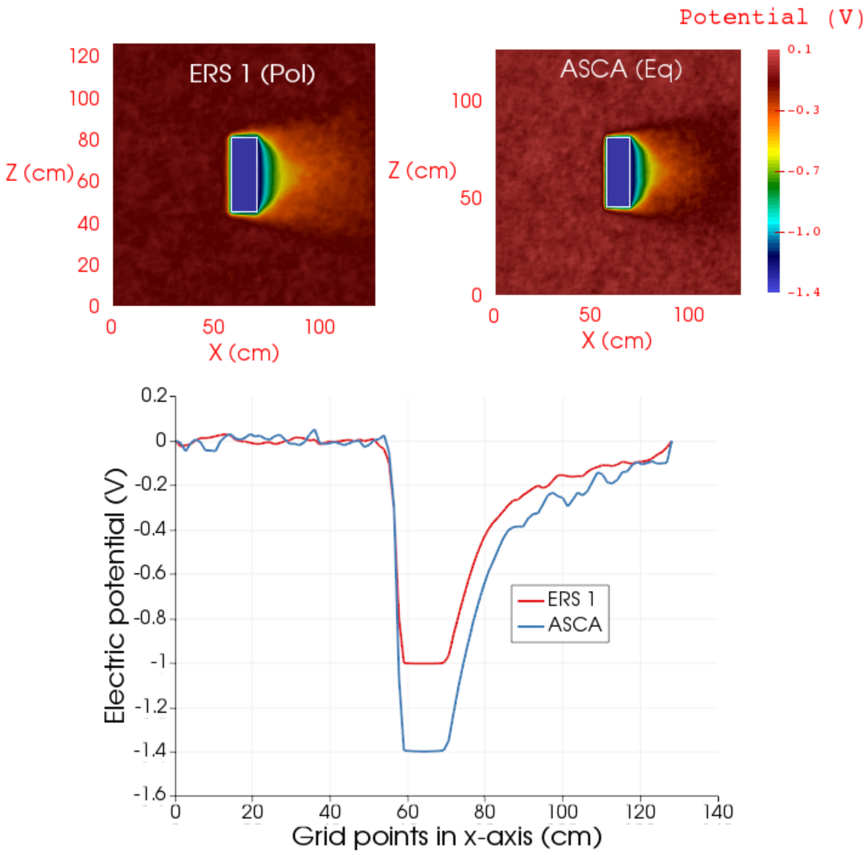

Figure 4.8: The potential distribution for polar (upper-left) and equatorial (upper-right) satellites ; The potential distribution along wake axis at z = 64 cm for both cases.

Furthermore, we show the potential distribution of two cases (ERS 1 and ASCA) shown in Figure 4.8. In general, based on our simulation for all cases presented in Table 4.1, there is no particular characteristic between polar and equatorial satellites in terms of electric potential. It means that the placement of satellite will not directly affect its electric potential.

Table 4.2: The levels of charging on LEO satellites

Satellite Name	Orbit Type	Potential (V)
ERS1	Polar	-0.97
Asca	Equatorial	-1.4
Terra	Polar	-0.82
Fuse1	Equatorial	-1.6
Fuse2	Equatorial	-2.25
Yohkoh	Equatorial	-0.8
Aqua	Polar	-1.4
Radar1	Polar	-0.5
Radar2	Polar	-0.62
Landsat 7	Polar	-1.14
Icesat	Polar	-1.62
Midori	Polar	-1.4
Dart	Polar	-1.7
Monitor E	Polar	-0.44
Kirari	Polar	-0.33
Kompass 2	Polar	-1.6
HST	Equatorial	-0.6
Metop A	Polar	-1.54
Orbview 3	Polar	-1.75
Orbcom 1	Polar	-0.5

As summary, the range of electric potential obtained from this simulation can be classified as follows.

1. Polar satellites : -1.75 V to -0.33 V
2. Equatorial satellites : -2.25 V to -0.6 V.

The detail of charging level addressed by LEO satellites in this study can be summarized in Table 4.2.

We found the general feature of density, potential and electric field for LEO satellites in this study as shown in Figure 4.9. In Figure 4.9, the sheath region is designated as square shaded spanning on the order of Debye length and characterized according to decreasing density in upstream side of the object. It is clear that the density of ions is larger than that of electrons in this sheath region. Moreover, as both densities inside the sheath region decrease the electric potensial declines monotonically in the ram (upstream) side. Conversely, inside the wake (downstream) region, the potential replenishes as both donsities increase toward the quasineutrality state. Here, we assume that the potential of ambien plasma is zero at distance far away from the object (infinity). Furthermore, the electric field around the object fluctuates following the potential shown by the lower panel of Figure 4.9.

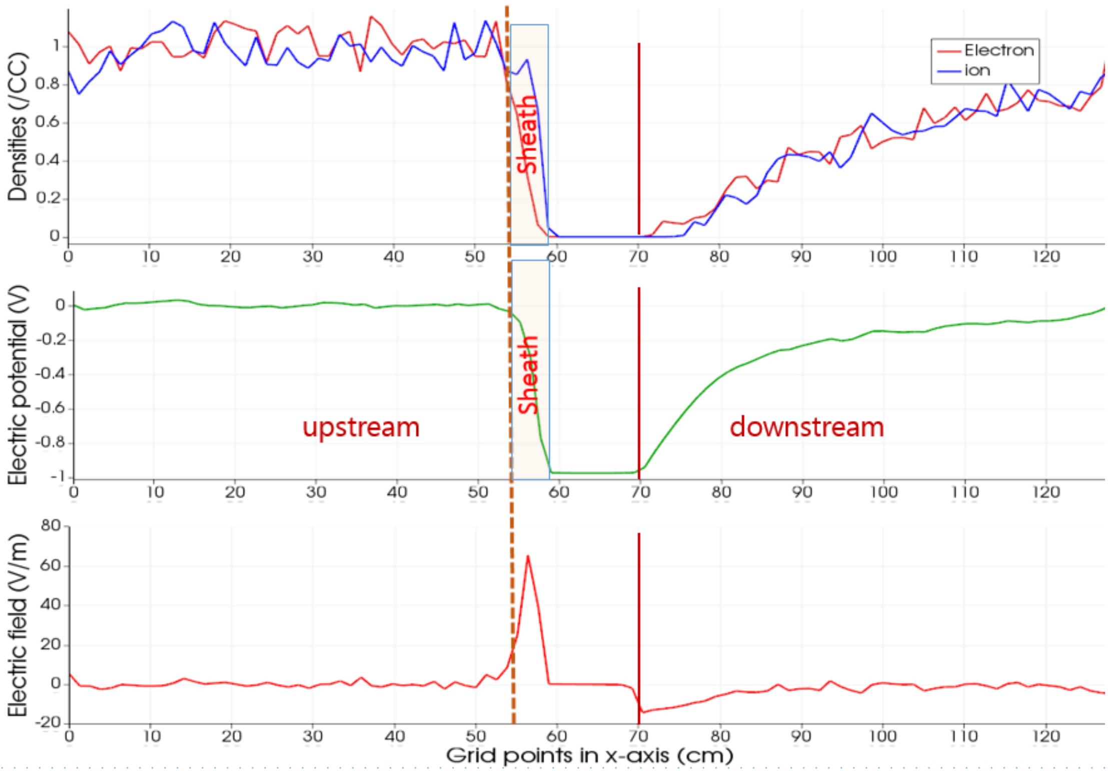

Figure 4.9: The general feature of parameter in the vicinity of spacecraft in LEO environment.

We then investigate the relationship amongst parameters and see how these parameters interact each other as shown in Figure 4.10. The density and electron temperature of each case in Table 4.1 in addition to their floating potentials (Table 4.2) are inventoried as follows.

1. The electron temperature (Te) and electric potential (ϕ) relationship (upper panel)
2. The density (n) and electric potential (ϕ) relationship (middle panel)
3. The electron temperature (Te) and ambient plasma density (n) relationship (lower

panel)

It is obvious that increasing temperature plays important role to decrease the object potential rather than density. The correlation coefficient reaches around 99%. It is worth noting that the density and electron temperature contribute altogether to affecting the potential through Boltzmann relation ($n_{e,i} = \ n_0 e^{\phi(x)/T_{e,i}}$). Nevertheless, simulation done using multiple cases (Table 4.1) shows that the contribution of electron temperature to spacecraft charging is more dominant compared to density. In addition, there is no apparent relation between electron temperature and density shown in lower panel of Figure 4.10.

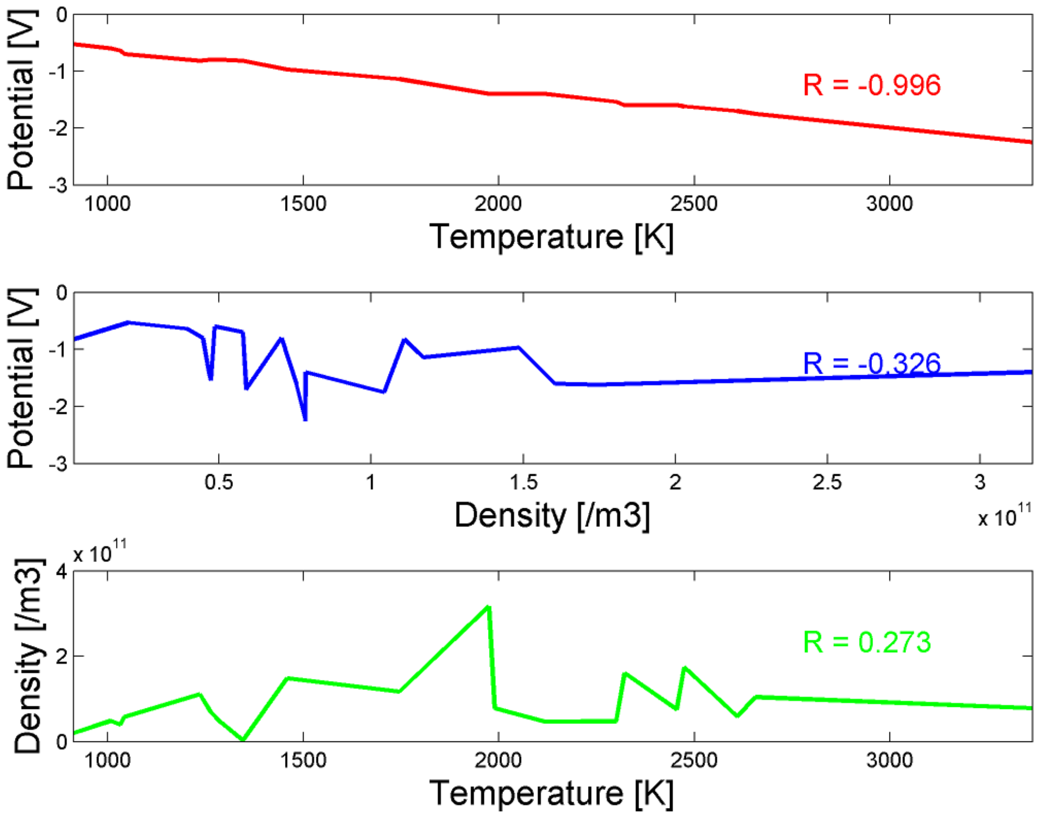

Figure 4.10: The relationship between electron temperature vs potential (upper), density vs potential (middle) and electron temperature vs density (lower) for all LEO cases in Table 4.1.

It is of interest to see the detailed of wake structure around LEO spacecraft immersed in ionospheric plasma. Here we performed another simulation by taking only ERS 1 case and see the behaviour of ambient plasma around it as seen more details in Ahmad et al. (2018) . We modify the size of the object to be 6 x 6 x 12 cm and keep the other settings in Figure 4.5. The results of simulation can be seen in Figure 4.11.

Figure 4.11 shows the density distributions of electrons (left) and ions (right) aroud the object in which the ion void region spans at point x ≈ 78 cm ($8.5\lambda_D$) behind the object. Here, the ambient plasma drifted with average velocity of 11.8 km/s, whereas the average thermal velocity for ions and electrons are 1.8 and 354 km/s, respectively and V_{sc} ~ 7 km/s. While the electrons randomly distributed in the vicinity of the object, the ions scattered giving rise to two symmetric tails toward donwnstream region as shown through white circles in Figure 4.7.

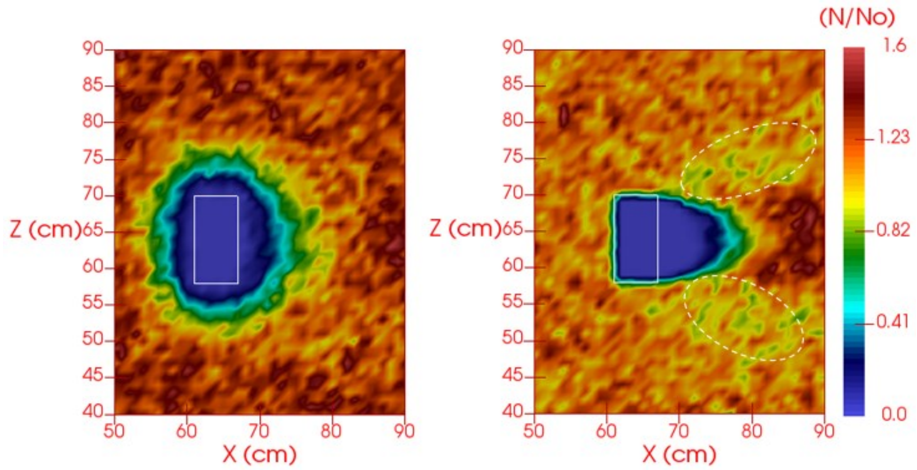

Figure 4.11: The density distribution of electrons (left) and ions (right) around the ERS-1 spacecraft in 2D (x-z plane). The spacecraft is located at grids 61 cm <x< 67 cm and 58 cm <z< 70 cm.

The structure of wake at downstram region in the direction of parallel (x-axis) and perpendicular (z-axis) to spacecraft motion can also be seen in Figure 4.12. Here the spacecraft position lies at the center of simulation box (61cm <x< 67 cm), and the wake centerline is centralized at z = 64 cm. In upper panel of Figure 4.12, it can be seen that the wake region in which the density of electrons is more dominant than that of ion spanning from the rear surface of the object to intersection point (P) at x ≈78 cm (~$8.5\lambda_D$). The intersection point (P) refers to the point at which the density ratio of electron to ion is unity. The rarefaction of ion density inside the wakefield reaches ~61% compared to ion density in upstream side. This means that ions are mostly absorbed by the spacecraft potential leading to ion depletion in the wake region. Conversely, in the upstream region the ion density is larger compared to electron density due to ion acceleration governed by electric field inside the sheath. The higher the magnitude of spacecraft potential, the more ions are captured and redirected by electric field toward the sheath.

We further looked up the structure of ion wake in the direction of perpendicular to the spaceraft motion (z-axis) shown in Figure 4.12 (lower). Here, we focus on the vertical wake structure at point x = 70.5 cm (~5 λ_D) from the object center. It is clear that both densities of ion and electron decline instrusively toward the wake axis at z = 64 cm. It is shown by two brown-arrow around the wake axis at lower panel. The density of ions dominates at region near upper and lower edges of spacecraft (green circles) and then decreases inside the wakefield corresponding to ion void region.

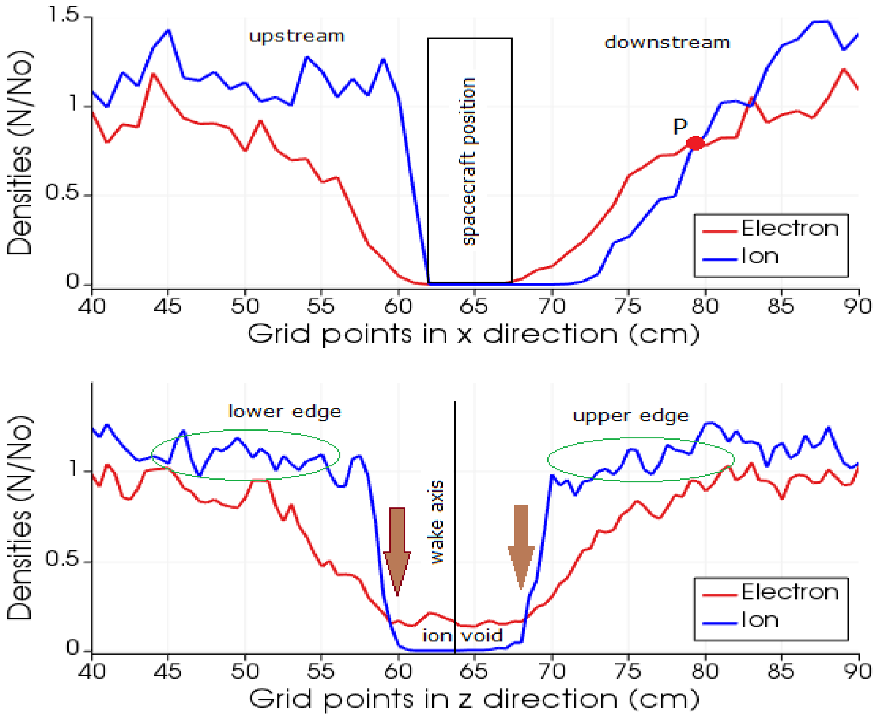

Figure 4.12: The structure of plasma wake in the direction of parallel (upper) and perpendic-ular (lower) to spacecraft motion. The red and blue lines represent the structure for electron and ion, respectively.

Since the acceleration of particle motion strongly depends on the electric field, we attempt to see the electric field distribution as well as the plasma current around the object shown in Figure 4.13. Here, we only show the behaviour of ion current rather than electron current due to electron randomness motion.

The ion trajectory is governed by the electric field. In this case, the flow energy of ion is larger than that of spacecraft potential by factor of 5. Thus, the ion flows toward the spacecraft without significant deflection explaining straightforward ion trajectory in Figure 4.13. As the ions gets closer and penetrates the sheath, the electric field starts accelerating the ion explaining the ion buildup in upstream region. Moreover, at distance around upper and lower edge of the sheath object, the ion trajectories are bended by the electric field (white circles) and elongated into downstream region. Nonetheless, inside the wake region close to wake centerline we can see the cavity indicating the ion void region. Since there is no big difference among parameters (e.g.

density and temperature) used in each case listed in Table 4.1, we guess that aforementioned behaviour is general feature of spacecraft-plasma interaction in LEO environment. The simulated results have been discussed more details in Ahmad et al. (2019).

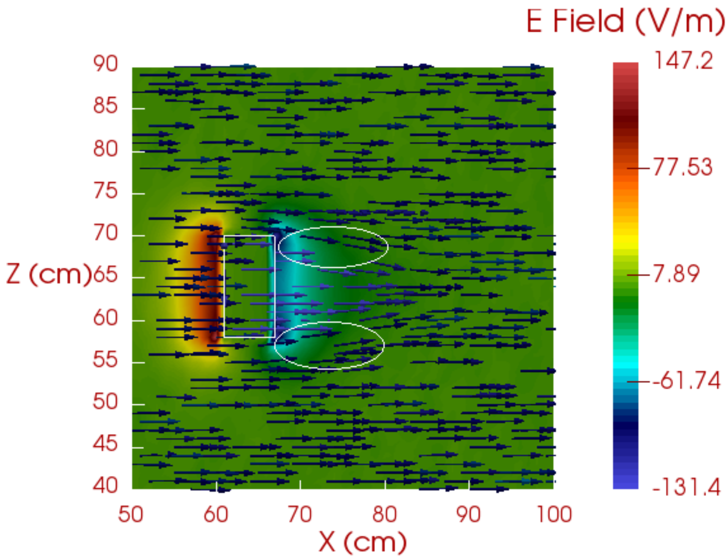

Figure 4.13: The magnitude of electric field distribution (contour map) and ion currents (arrows) in x-z plane around the spacecraft.

Chapter 5

Spacecraft-Plasma Interaction in the Presence of Auroral Electrons

To get better understanding about the floating potential as well as the morphology of wake structure in the presence of auroal electrons, one can use the satellite failure case attributed to environmental charging. It is of interest that the presence of auroral electrons is not always resulting in high voltage charging as shown through studies by Wang et al. (2008) and Ueda et al. (2009). This means that we can not expect all simulations involving auroral electrons will give rise high voltage charging on the spacecraft. Nevertheless, we attempted to examine the potential and the wake structure by employing some LEO satellite failure cases listed in Table 4.1. We setup the simulation as shown in Figure 5.1.

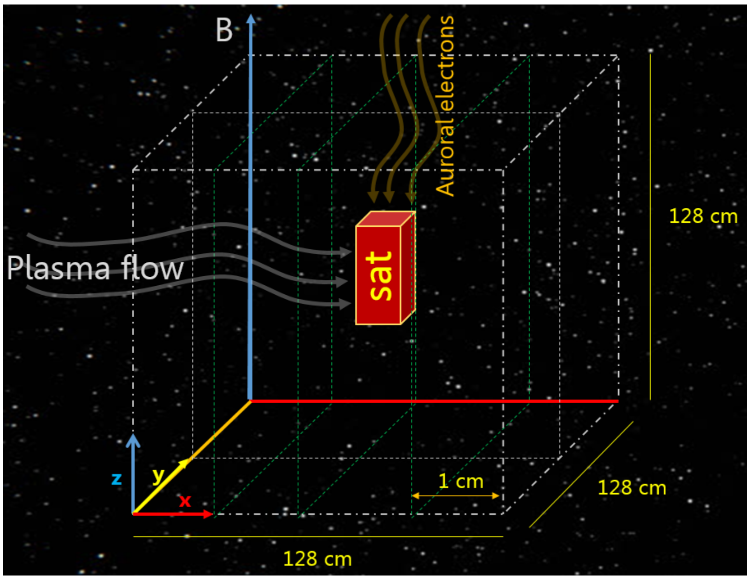

Figure 5.1: The model of simulation box in the presence of auroral electrons

5.1 LEO Satellites in Nightside

In this section, we performed two LEO satellite cases, i.e., ERS-1 and ADEOS-II satellites, during the daytime passage in which the effect of photoelectrons is neglected. The European Remote Sensing Satellite -1 (ERS-1) is an ESA earth observation satellite which was launched on July 17, 1991 at 772 km altitude (https://directory.eoportal.org/web/eoportal/satellite-missions/e/ers-1) and had completed its operation permanently (total loss) due to unknown failure. The similar total loss failure was also sustained by the Advanced Earth Observing Satellite – II (ADEOS-II) belongs to JAXA and had only survived in its orbit for almost 10 months since its launch on December 14, 2002 at 805 km altitude (http://www.satnavi.jaxa.jp/project/adeos2/) .

ERS-1 and ADEOS-II satellites were placed at slightly different altitudes, but at the same polar inclination of 98°. Both satellites passed through polar region approximately 10 times per day with duration around 16 minutes. The estimated calculation is based on auroral oval crossing in which LEO polar satellite such as DMSP experinced high negative charging more than 100 V (Anderson 2012). Within the dynamically auroral oval region, there exist rapid variation of thermal component of ionosphere as well as high energy particles which are strongly related to magnetic activity (Hastings 1995). We have investigated that both failures on satellites occurred near solar maximum around the two extrem solar flares of 14 July 2000 and 28 October 2003 (Tsurutani et al. 2006). The maximum Auroal Electrojet (AE) and solar radiation flux of F10.7 indices were about 760 nT and 200 sfu, respectively on ERS- 1 anomaly day and those of 1205 nT and 189 sfu on ADEOS-II failure day (https://omniweb.gsfc.nasa.gov/form/dx1.html). The AE index characterizes the geomagnetic disturbance related substorms in auroral region, while the F10.7 index is assured as a proxy of Extrem Ultraviolet (EUV) in upper atmosphere (Hastings and Garret 1996). The AE and F10.7 indices, for both cases, showed high level disturbance and strongly affected LEO polar satellites as found by Dorman et al. (2005). In their study, they pointed out that the AE index was attributed to the annual variation of ionospheric conductivity contributing to LEO polar spacecraft anomalies.

5.1.1 Simulation on ERS1 Satellite Case

We ran the simulation by classifying the cases with respect to two conditions, i.e., in the absence of auroral electrons (called case #1) and in the presence of auroral electrons (called case #2). In all cases the density of ionospheric plasma is larger than that of precipitating auroral electrons by factor of 10^4. Here, we changed the integration time step as well as number of iteration to be 10^{-11} s (1 ps) with 2.10^6 iterations, respectively and kept the other settings. The scattered densities of electrons and ions for case#1 have been previously shown in Figure 5.2. In this subsection we only show the wake structure regarding auroral electrons impact where the distribution of ambient plasma can be seen in Figure 5.2.

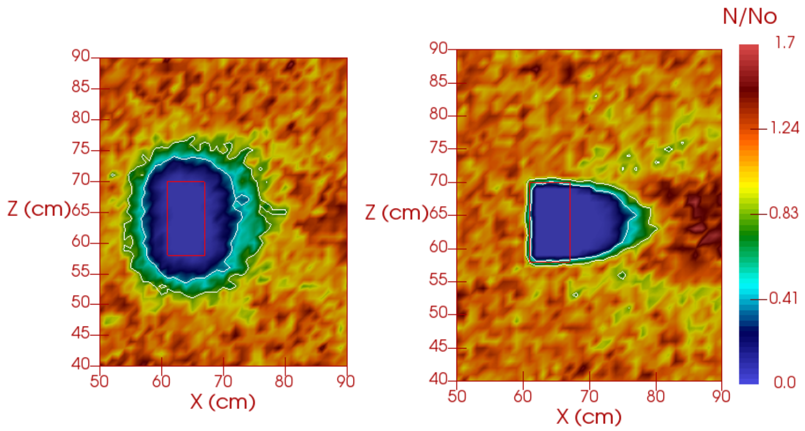

Figure 5.2: The distribution of ambient electrons (left) and ions (right) in the presence of auroral electrons.

In this case, the drift velocity of ambient plasma is determined through the ion acoustic speed from which the average mach number is approximately 6 (Mikaelian 2001). It is of interest that the presence of precipitating electrons in case #2 insignificantly modified the whole wake structure due to high density ratio between ambient plasma and auroral electrons by factor of 10^4 (see Table 4.3). In addition, the induced potential insignificantly changed compared to case #1. Nonetheless, the similar feature is found where the ambient plasma densities decline intrusively toward the object and the wake axis (z = 64 cm).

Table 5.1: Parameters depicted satellite environment for case #1 and case#2

Parameter	Condition	
	Case #1	Case #2
T_i/T_e (Ionospheric)	0.78	0.78
N_p (m-3 ; Ionospheric)	4.10^{10}	4.10^{10}
T_{ae} (K ; auroral el)		$2.3.10^8$
N_{ae} (m-3 ; auroral el)		10^6
$V_{th.ae}$ (km/s)		$8.3.10^4$
$V_{d.ae}$ (km/s)		3.10^4
Γ_r (Γ_{ae} / Γ_e)		10^{-2}

The ambient ions and electrons temperature ratios for case#1 and case#2 are set similar. The temperature of electrons is 1.3 times higher than that of ions. The precipitating auroral electrons subsonically drifted with average velocity 30% lower than thermal component presented in Table 5.1. Here, the notation of ‘p’ and ‘ae’ represents the plasma and auroral electrons, respectively. Γr is the flux ratio between auroral electron and ambient electron. It is obvious that the ambient electron is dominant compared to the other fluxes. As consequence, overall the wakefield is controlled by the ambient plasma rather than the auroral electron, thus the wake structure in the presence of auroral electrons expanded bit outward the object shown in Figure 5.3.

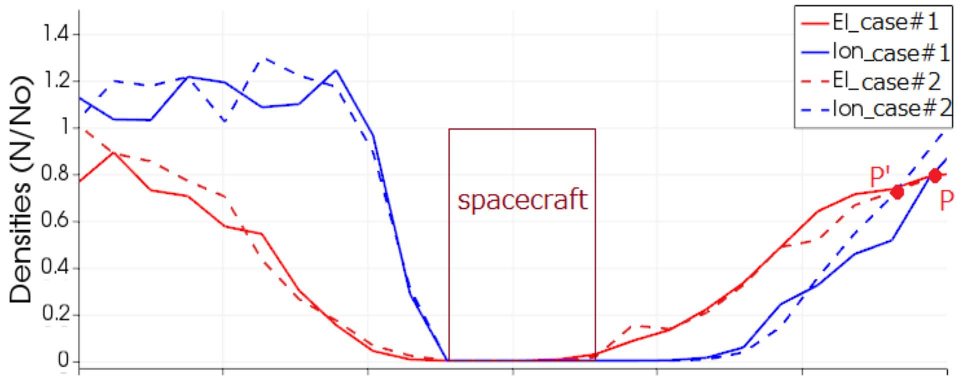

Figure 5.3: The density profiles within the wake region for case #1 (solid lines) and case #2 (dashed lines) along x direction. The brown-square indicates the position of the spacecraft inside the simulation box in x-z plane.

Figure 5.3 is created along x axis and at z = 64 cm, along the wake centerline (only part of simulation box is showed). In this figure, the ambient density profiles in case #1 are represented by the solid lines, while the density variations around the object in the presence of auroral electrons, case #2, are indicated by the dashed lines. The point P denotes the edge of ion void region (in this paper is called as the edge point) for case #1, whereas the point P' designates the edge point for case #2. Here we define the edge point as the boundary scale in which the density ratio of electrons to ions is unity inside the wakefield. The density of electrons dominates in scale less this point, while the ion density is larger than that of electron beyond this point. We intentionaly show these points just to show the different features of ion void regions between without and with the auroral electrons. Thus, the presence of auroral electrons shifts this point inward which in this case spans around $8.5\lambda_D$ (x ≈ 78 cm ; at P') from the rear surface of the object.

The shifted edge point is somewhat similar to the feature explained by Wang et al. (1994) where the high charged object yields the ion backflow in the wake. As consequence, there exists adequate ions along the wake centerline to equilibrate the electrons.

We further analyzed the wake structure perpendicular to the wake centerline, along the z-axis and at x = 70 cm (at distance ~2.3λ_D from the rear surface). The density profiles are shown in Figure 5.4 which shows the variation of ambient plasma inside the wakefield in the vicinity of the spacecraft. The domination of electron plasma is obviously seen in which the average density of electrons 10% larger than that of ions as shown through the green circle in this figure . The wake structure especially electrons changed bit wider from case #1 to case #2. In this case, the flowing plasma has the same angle of attack which is perpendicular to the spacecraft surface. It is clearly shown that the wake density in vertical direction for both cases monotonically decrease toward the wake centerline.

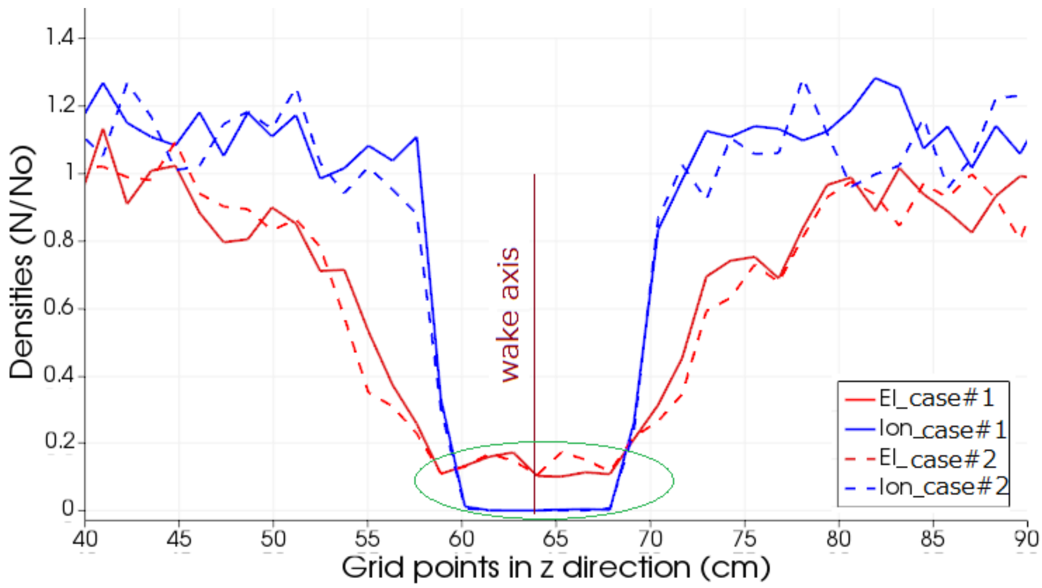

Figure 5.4: The density profiles inside the wakefield along the z direction. The solid lines represent the wake structure for case #1, while the dashed lines designate the wake structure for case #2.

The impact of auroral electrons on the spacecraft in case #2 insignificantly contributed to higher negative charging. In the absence of auroral electrons in case #1, the charge buildup on the spacecraft is purely affected by the ambient plasma currents, thus the induced potential reaches -2V. In the presence of perturbation from the auroral electrons, the floating potential dropped to ~ -2.4 V. The dominant current comes from ambient plasma rather than the auroral electron. Nevertheless, the higher potential of the spacecraft in case #2 insignificantly changed the wake structure.

We initially expected that the higher voltage charging occurred in the presence of auroral electrons. In order to examine our simulation is relatively accurate, we calculated the potential analytically using equation 3.15 by assuming the auroral electron are in maxwellian distribution. Thus, we obtained the analytical solution of potential is around -1.2 V shown in Figure 5.5.

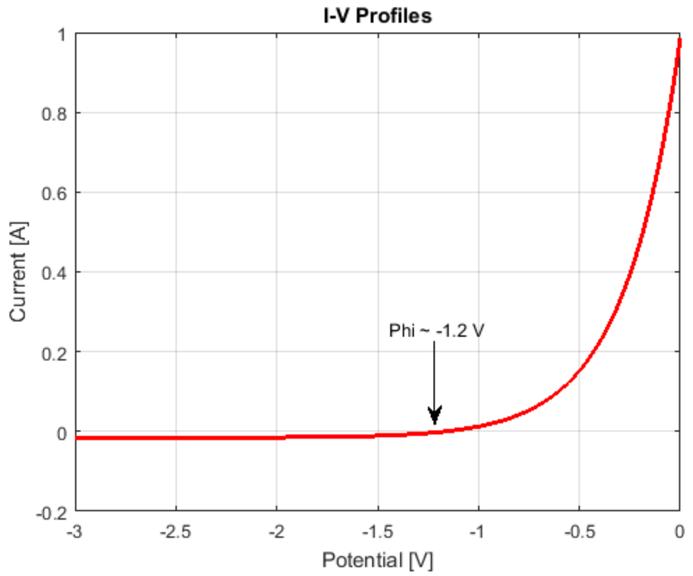

Figure 5.5: The analytical solution of potential for ERS-1 case in the presence of auroral electron (case #2).

The current will be balanced each other (total current, $I_t(V) = 0$) at point around -1.2 shown in Figure 5.5. In this figure, x and y axes represent the spacecraft and total current on the spacecraft, respectively.

It is of interest that the charging as well as the modified wake structures in case #1 and case #2 insignificantly changed even in the presence of auroral electrons in case #2. The induced lower potential in case #2 linked to the domination of ambient plasma currents over the auoral electron currents which are implicitly shown through the density distribution at the downstream region. Here, we attempt to compare spacecraft charging in the presence of auroral electrons between case #2 in this study with high voltage charging faced by LEO DMSP satellite.

As previously mentioned that the DMSP satellite, particularly F6 and F7 series, has been acclaimed to experience high negative charging in the range -47 to -679 V under conditions of which the ambient plasma density dropped and the flux of auroral electron increased in addition to spacecraft in the darkness. Since the parameters depicted the environment for DMSP satellite are somewhat similar order to those of our case #2 (see

Table 5.2), it is interesting to further discuss the difference between two cases.

Table 5.2: Comparison between parameters used for DMSP charging and case #2 of ERS-1.

Parameter	Condition	
	DMSP	ERS-1 Case #2
N_p (cm-3 ; Ionospheric)	$< 10^4$	4.10^4
T_{ae} (keV ; auroral el)	≥ 14	~ 10
N_{ae} (cm^{-3} ; typical auroral el)	-	1
Γ_{ae} (electrons.cm^{-2}.s^{-1}.$ster^{-1}$)	10^{10}	10^{10}

We can see that overall the parameters used for both cases are alike, except for the ambient plasma density and temperature of auroral electrons as presented in the first and the second rows of Table 5.2, respectively. As has been previously shown that at the time of ERS-1 failure, the satellite passed through the auroral arc during eclipse region (see Figure 3.8).

We attempt to overview the DMSP charging using closest temperature as in our case, that is 12 keV (Yeh and Gussenhoven 1987). They found that the negative charging on DMSP ranged from 100 to 317 V. On the other hand, by employing almost identical parameters as DMSP, we found very low negative charging on ERS-1 eventhough it has already fulfilled the condition for DMSP charging. Since the difference between temperature (12 keV for DMSP and 10 keV for ERS-1) is not too large, we inferred that this discrepancy does not come from the temperature energy. Another explanation comes from the density of auroral electrons used for DMSP charging. According to our knowledge of simulation, the smaller the density ratio of auroral electron to ambient plasma, the higher the magnitude of negative charging on the spacecraft. We suspected that the auroral density linked to high DMSP charging is much larger than that of our case.

In attempt to reach very high charging in our simulation, we performed another simulation on ERS-1 (case #3) by increasing the density of auroral electrons 100 times than that of case #2 as presented in Ahmad et al. (2018). Now we have the density ratio of auroral electron to ambient electron around 0.25 %, and the flux ratio (Γr) is unity. In order to describe the detailed structure of the wake, we modified the grid cell size as well as the total grid in each side of simulation box to be 0.25 cm and 256 cm, respectively. In this case, the simulation box size becomes smaller which is 64 cm. We intentionally did not change the box size to avoid the time-consuming simulation. The results of simulation for case #3 can be seen in Figure 5.6.

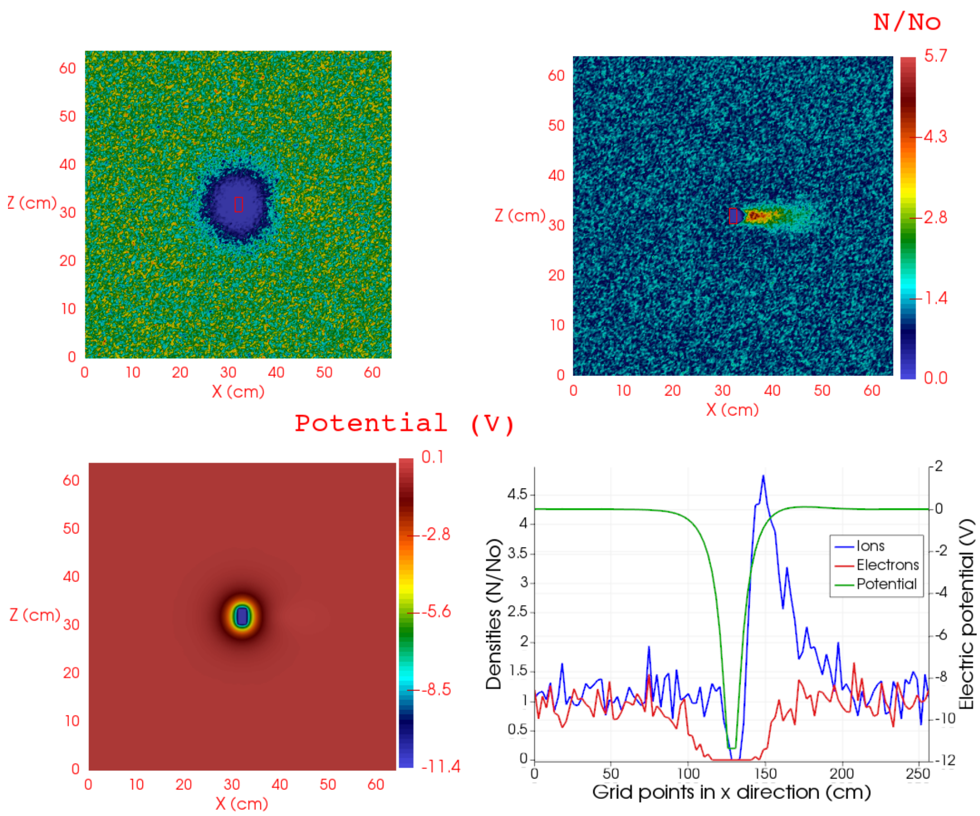

Figure 5.6: The distribution of electrons (upper-left), ions (upper-right), potential (lower-left) and the lineplot of each parameters for case #3.

We still can not get the higher potential as DMSP charging by increasing the density of auroral electron 100 times and the flux ratio (Γr) becomes unity. The new potential is around -11.4 V. However, the wake structure of ion totally changed in which the pronounced focusing ion at the downstream region occurred shown at upper-left panel in Figure 5.6. The discussion about the focusing ion will be discussed in the next subsection.

The simulation of auroral electron contribution to the spacecraft charging for case #2 and case #3 resulted in low negative potential. We tried to compare our results with observational DMSP charging shown in Figure 5.7.

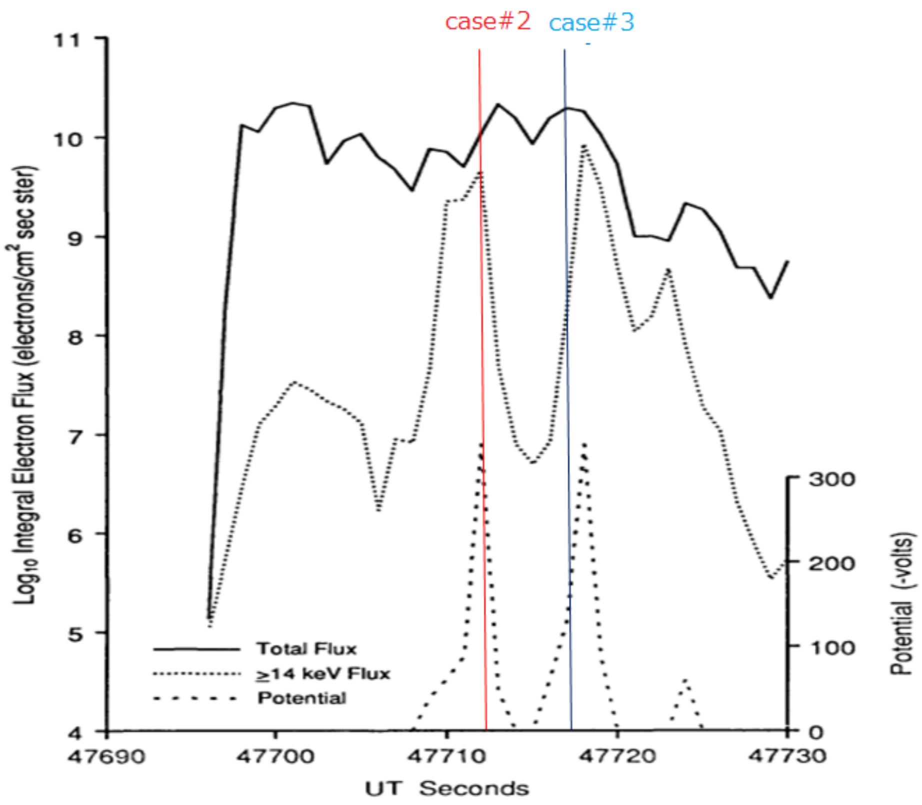

Figure 5.7: The relation of total flux (solid line) and auroral electron flux of ≥14 keV (dotted line) with DMSP satellite charging (dashed line). The vertical blue line is the rough estimation of flux in case #2, whereas the vertical red line is for case #3.

Figure 5.7 depicts the total flux and auroral electron flux during DMSP satellite charging obtained from observation. We can see that overall the smaller the flux ratio between auroral electron and ambient plasma, the higher charging on the DMSP satellite. It means that the presence of auroral electrons dominantly controls the total current on the spacecraft. We estimated roughly the flux ratio for case #2 and case #3 in this study adjustable to above picture represented through vertical blue and red lines, respectively in Figure 5.7. In case #2, the flux of ambient plasma is more dominant 100 times than the flux of auroral electron, thus we obtain very low charging on the spacecraft (blue line). As we increased the density of auroral electron by factor of 2, the Γr value becomes comparable (unity). As the result, the magnitude of negative charging increases (red line) around 5 times than that of case #2. It means that the condition of high voltage charging on the spacecraft will be satisfied if the flux ratio of auroral electron to ambient plasma becomes larger.

5.1.2 Simulation on ADEOS-II Satellite Case

In case of ADEOS-II simulation, the ions and electrons temperature ratio is empirically set lower than ERS-1 case. However, the electron temperature is 1.5 times higher than the ions temperature (Table 5.3). The plasma drifts with velocity of 9.8 km/s, while the ions and electrons thermal speeds are 1.5 and 312.5 km/s, respectively. The average debye length (λ_D) is 2.2 cm. The parameters used in this case can be seen in Table 5.3.

Table 5.3: Parameters used for ADEOS-II case

Parameter	Condition	
	Case#1	Case#2
T_i/T_e (Ionospheric)	0.64	0.64
N_p (m^{-3} ; Ionospheric)	9.10^9	9.10^9
T_{eu} (K ; auroral el)		$2.3.10^8$
N_{eu} (m^{-3} ; auroral el)		10^6
$V_{th.ae}$ (km/s)		$8.3.10^4$
$V_{d.ae}$ (km/s)		3.10^4
Γr (Γ_{ae} / Γ_e)		5.10^{-2}

The similar features are seen of which the densities rarefaction occurred in the wake region (Figure 5.8) for case#1 and case#2 conditions. It is of interest that within the wakefield the density ratio between electrons and ions is slightly reduced in the range 67 cm < x < 80 cm (~ $6\lambda_D$) reaching 5 % in case#2 as shown in Figure 5.9. This feature is also seen in ERS-1 where the decline rate is around 1.3%. This is one indication that as the object is more negatively charged the stronger electric field begins to attract and bend the ions trajectories toward the object and the wake axis.

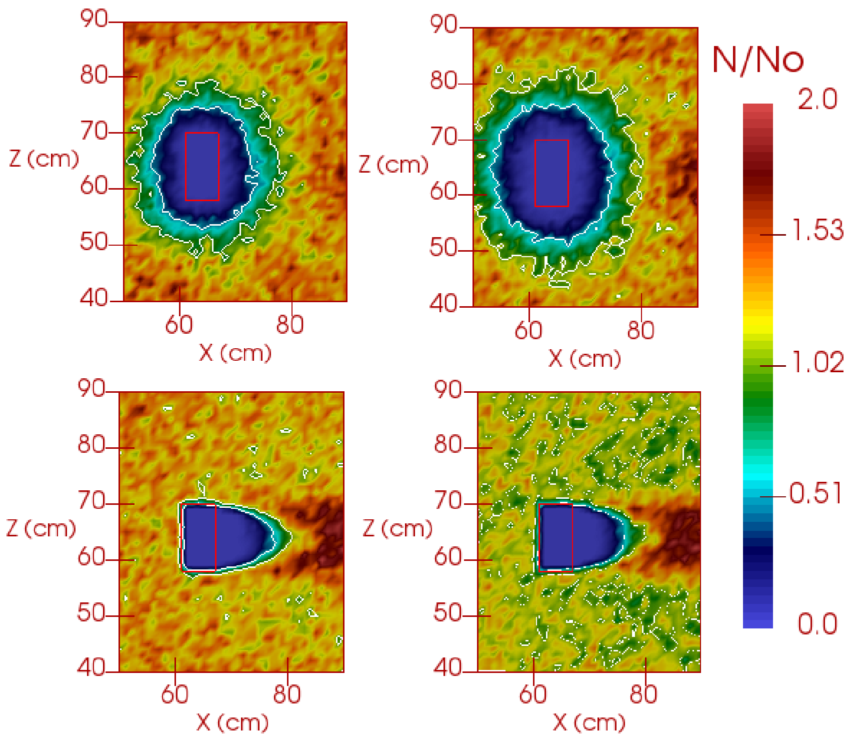

Figure 5.8: The densities distribution for electrons (upper) and ions (lower) for case#1 (left) and case#2 (right) for ADEOS II case. The densities are normalized to initial ambient plasma density (No).

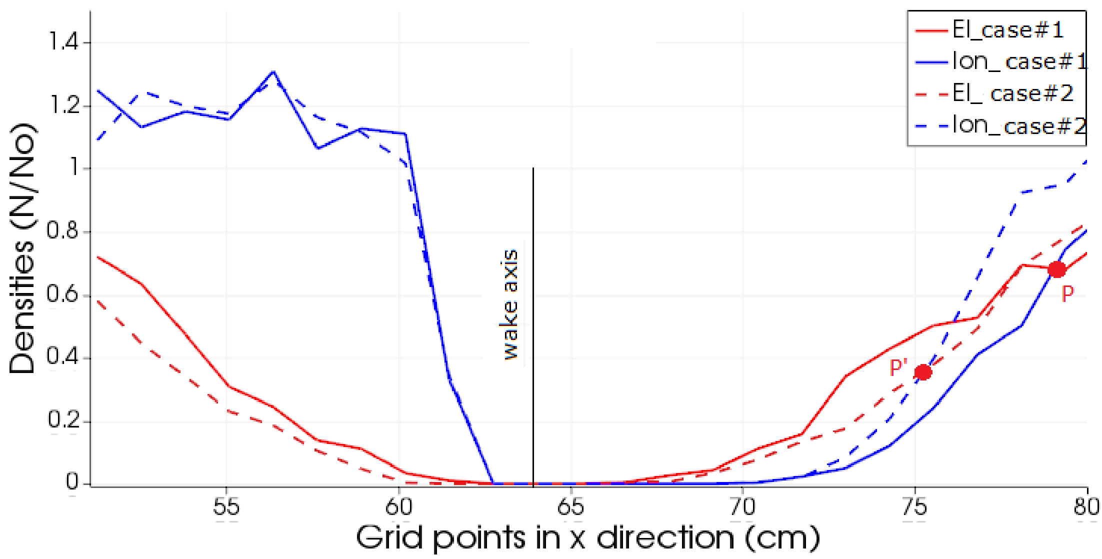

Figure 5.9: The wake structure for case#1 (solid lines) and case#2 (dashed lines) for ADEOS II case along x direction. The edge points are represented by P (case#1) and P' (case#2).

The wake density in vertical direction (along z axis) shows reduction of ion void region in case#2 as shown in Figure 5.10. This reduction is bit larger than that of ERS-1 case. The average density of electrons 2 times larger than that of ions. The electric field starts bending the ion trajectory at the point around $3\lambda_D$ from the wake axis. Both densities of electrons and ions decrease intrusively toward the wake centerline

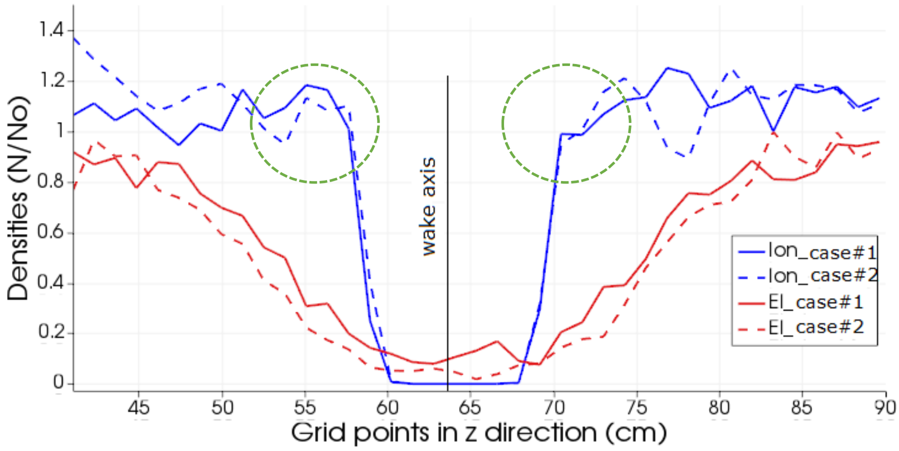

Figure 5.10: The wake structure in vertical direction (along z). The case#1 and case#2 are represented by the solid and dashed lines, respectively

It is evident that the electrons are highly depleted due to higher negative potential on the object. On the other hand, the attracted ions move as the electric field becomes stronger toward the object. However, there exists slight different of wake structure between horizontal (Figure 5.9) and vertical (Figure 5.10) in which the density ratio of ion to electrons in case#1 and case#2 is larger on vertical than that of horizontal direction. We guessed that this is due to the effect of the edge sheath around the object as proposed by Wang and Hastings (1992). As the ion trajectories pass the edge sheath, the electric field in the edge sheath accelerates and deflects ions inside the wakefild leading to ion concentration regions (green-dashed lines) shown in Figure 5.10. On the other hand, the potential distribution inside the wakefiled only leads to small curvature on ion trajectories eventhough in the presence of auroral electrons.

The impact of auroral electrons on the spacecraft insignificantly increases the magnitude of negative potential from 1.7 V up to 2.2 V, so thus insignificantly modified the whole wake structure. However, the presence of auroal electrons in moderate contributes to distort the ion void structure in case#2. It can be known by looking at the structure of the wake in horizontal (along x direction) and vertical (along z direction) in Figure 5.9 and 5.10, respectively.

We tried to compare theharging as well as the modified wake structures in case#2 condition for both cases ,i.e., ERS-1 and ADEOS-II and we found that both features are slightly different and necessarily to discuss. Both satellites have fairly similar evironmental data in terms of density, but significantly different of electron and ion temperature ratios. We focus on two issues, i.e., the wakefield structure and floating potential of the object.

It is clear that the wake structure appears of which the electron population is dominantly scattered within the depleted region of ions. In case#2, the wake structure generally symmetric where the ambient plasma densities tend to decrease toward the wake axis. Nevertheless, the width of wake between ERS-1 and ADEOS-II cases is slightly different. The wake width in this study refers to the wake structure along vertical direction which is sliced at x = 70 cm behind the object. Since we utilized the same geometry and dimension of the object, the wake width supposedly came from different parameters used in the simulation. The width of wake structure for both cases can be seen in Figure 5.11.

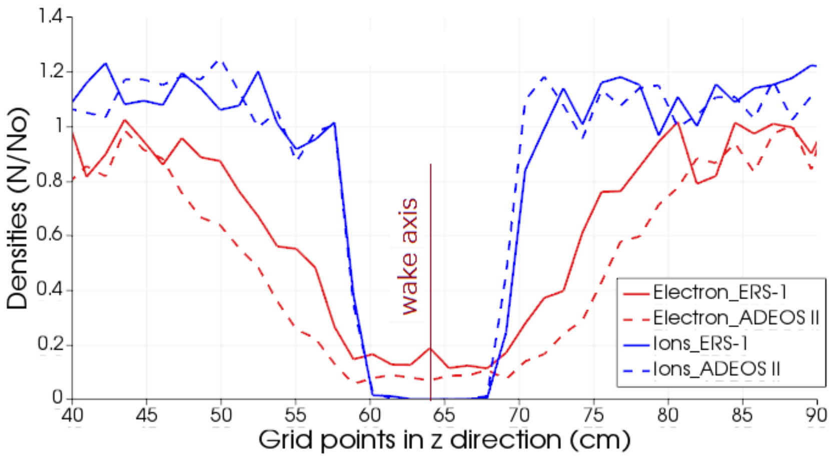

Figure 5.11: The comparison of wakes width between ERS-1 and ADEOS-II in the presence of auroral electrons (case#2).

Figure 5.11 shows the wake width comparison between the above two cases, i.e., ERS-1 and ADEOS-II. Both satellites are placed at a slight different altitude of 772 and 805 km. The solid lines in Figure 5.11 represent the density of electrons (red) and ions (blue) for ERS-1, while the dashed lines designate the density of electron (red) and ion (blue) for ADEOS-II. We localized the wake width comparison within wakefield of x = 70 cm and 40 cm < z < 90 cm from the wake centerline of 64 cm. It is obvious that all densities decline toward the wake centerline. Overall, the width of wake in ADEOS-II case is larger than that of in ERS-1 case. It seems that this feature depends on the satellite altitude. The higher the altitude the wider the wake, meaning that the width is increasing with decreasing density. This feature is clearly shown through the profile of electron rather than the ion shown in Figure 5.11.

5.2 LEO Satellite in Sunlight

We performed another case by employing a LEO satellite during daytime passage in which the effect of photoelectron on satellite is included. Here, we undertook failure case of Aqua satellite, which was reported to experience failure on 27 June 2002 (http://sat-nd.com/failures/). We performed two cases, i.e. without (case#1) and with auroral electrons and photoelectrons (case#2). The parameters used in Aqua simulation can be seen in Table5.4.

Table 5.4: Environmental parameters for AQUA case with photoelectrons

	Condition	
	Case #1	Case #2
T_i/T_e (ionospheric)	0.66	0.66
N_p (m^{-3} ; ionospheric)	$6.5.10^{10}$	$6.5.10^{10}$
T_{ae} (K ; auroral el)		$2.3.10^{8}$
N_{ae} (m^{-3} ; auroral el)		10^{6}
T_{ph} (K ; photoelectron)		3.10^{5}
N_{ph} : (m^{-3} ; photoelectron)		$6.5.10^{10}$

The electron and ion temperatures in case#1 were about 0.3 eV and 0.2 eV, respectively and debye length is ~ 1.5 cm. We applied the similar parameters as of ERS-1 case regarding the ambient temperature ratios and density of precipitating auroral electrons listed in Table 5.4. We keep on setting the density of photoelectron similar to the density of ambient plasma and applicable not only for case#1, but also for case#2. In general, the wake structure in case#1 resembles the previous two cases (ERS-1 and ADEOS-II), thus we interested in comparing the wake structure without and with photoelectrons shown in Figure 5.12.

In case#1 the wake structure overall similar to ERS-1 and ADEOS-II cases in which the ion void region forms behind the spacecraft. Conversely, in the presence of photoelectron in case#2, the dominant density comes from the ambient ion. In the downstream side, the ion void region disappears and transforms to be the ion concentration region (ion focus). The density of ions increases significantly compared to that of ambient electrons and photoelectrons. The ion focusing region spans from distance around $3.3\lambda_D$ ($x \approx 72$ cm) from the rear surface of the spacecraft as shown in Figure 5.13.

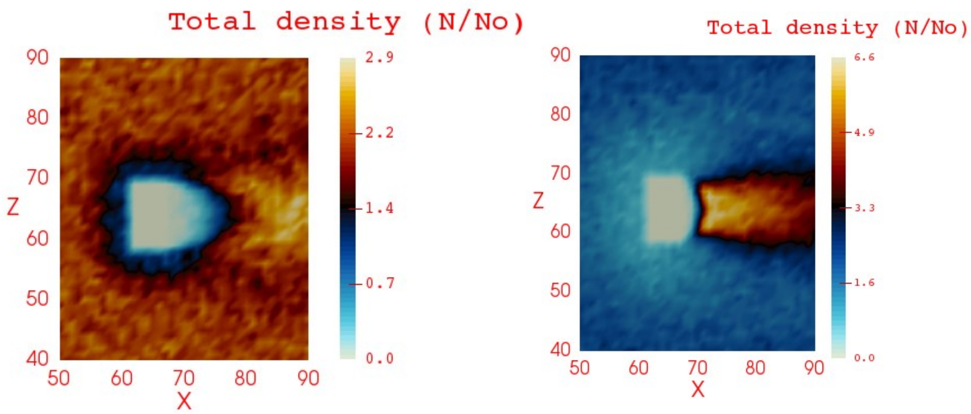

Figure 5.12: The total density distribution around AQUA spacecraft in the absence (left panel) and presence (right panel) of photoelectrons during perturbed condition.

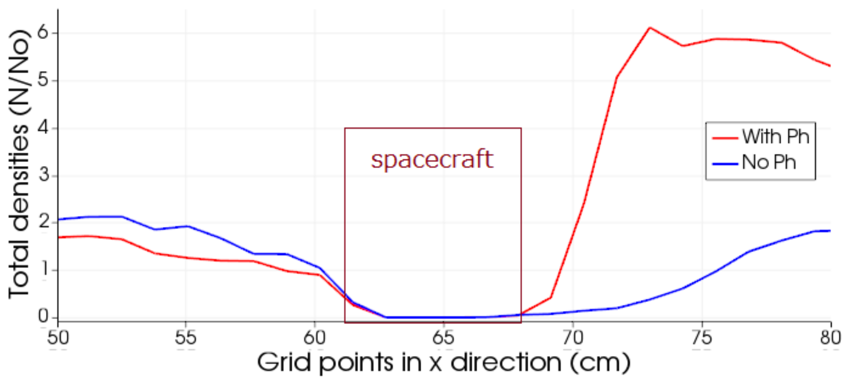

Figure 5.13: The total density distribution along the wake centerline (horizontal) at z = 64 cm without photoelectrons (blue) and with photoelectrons (red).

Figure 5.13 shows the total density distribution around the spacecraft in the absence of photoelectrons (blue line) and in the presence of photoelectrons (red line). The presence of photoelectrons affects the ion density enhancement. The peak of ion density lies at distance ~$3.3\lambda_D$ ($x \approx 72$ cm) from the object. We guessed that this is related to increasing potential behind the spacecraft. Throughout simulation the photoelectron temperature is higher than that of ambient plasma electron by factor of 10^2. Due to lower drift velocities compared to their thermal component, all electron species including the photoelectron move subsonically with respect to the spacecraft. The profiles of ambient plasma and photoelectron in vertical direction at x = 70 cm can be seen in Figure 5.14.

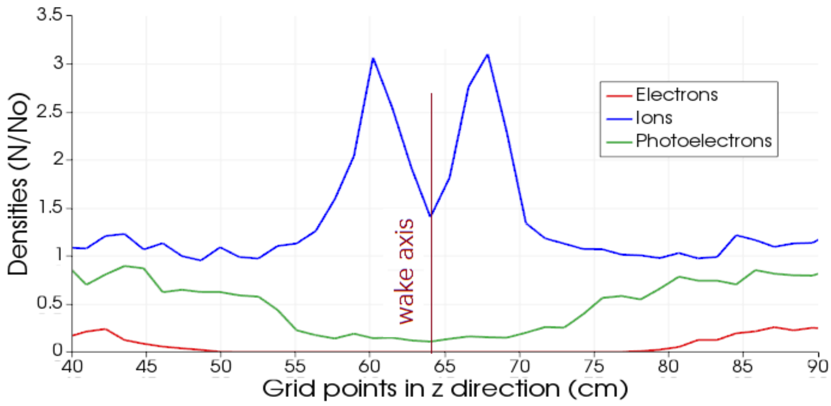

Figure 5.14: The density profiles of ambient plasma and photoelectrons in vertical direction at distance $2\lambda_D$ (x = 70 cm) from the object

Two ion concentration regions appear symmetrically around the wake centerline. Different from the structure of electrons and photoelectrons, the ions structure shows increasing density rather than monotonically decreasing toward the wake centerline. It fluctuates and starts increasing and peaks at distance ~ $2.6\lambda_D$ (x ≈ 60 cm) and drops toward the wake axis and then increases again as shown in Figure 5.15. In this case the ion trajectory is more affected by the electric field due to higher negative potential on the spacecraft. In case of AQUA, the induced potential in case#2 is around -22V.

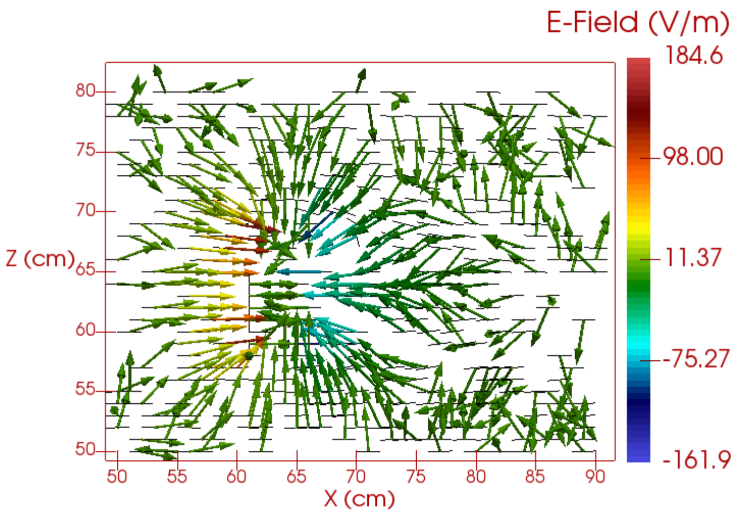

Figure 5.15: The trajectory of ions (brown line) and electric potential distribution (arrow) around the spacecraft in the presence of photoelectrons case.

In addition, it is also interested in discussing the ion focus region in the presence of photoelectrons. Due to lower potential, the electric bends the ion trajectory leading to ion attraction and peaks at distance 3.3λ_D from the rear surface as shown in Figure 5.15.

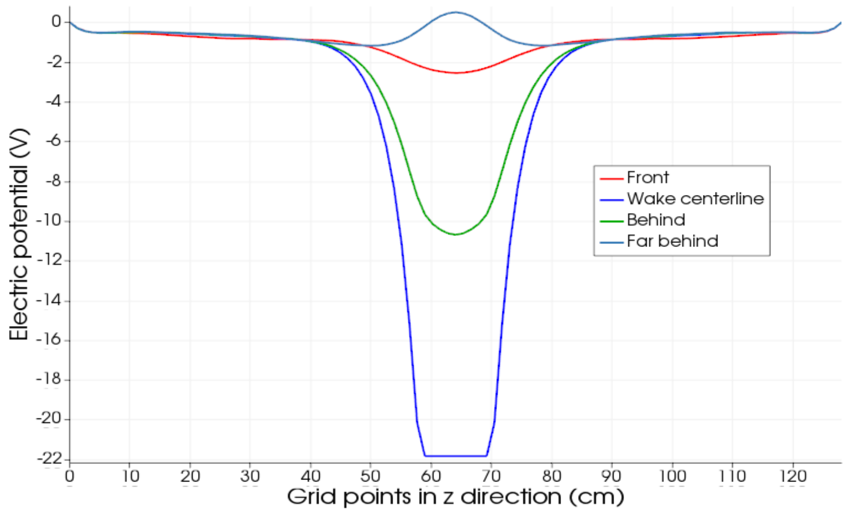

Figure 5.16: Potential profiles in the presence of photoelectrons along vertical direction.

As has already shown (Figure 5.14) that the ion density at the center of the wake is dropped along the vertical direction. This is related to the increasing potential around the object in which the potential becomes positive (grey curve) toward the wake centerline shown in Figure 5.16.

Figure 5.16 shows the variation of potential in the vicinity of the spacecraft at following points, i.e., 9.3λ_D (x ≈ 50 cm) in front (red), wake axis (blue), 4λ_D (x ≈ 70 cm) behind (green) and 10.6 λ_D (x ≈ 80 cm) far behind the object (grey). The acceleration of ions occurs coinciding with negative potential in front of the object and lasts at distance right behind the object. It explains the arise of two symmetric ion concentration regions in Figure 5.14. As the potential of the wakefield becomes positive (grey line in Figure 5.16), the repulsion of ions occurs leading to ion currents reduction in this area owing to the drop of ion density between the two concentration regions shown in Figure 5.14. The existence of ion focusing around the object is more pronounced in the presence of photoelectrons. Since the ion focusing is temperature ratio (T_e/T_i) dependence (Miloch 2010), the greater temperature of electrons gives rise to ion enhancement as shown in AQUA case. In addition, the variation of potential around the object shown in Figure 5.16 contributes to ions deceleration as well as their trajectory deflection. It is evident that higher negative potential creates the ion backflow curvature (see Figure 12 and 13 in their manuscript) toward the object explaining the midwake ion density enhancement (Wang and Hastings 1992). Furthermore, the higher potential of the object scatters the ions inside the wakefiled, but immediately being repelled toward the object as it approaches the wake potential far behind the object (at x ≈ 80 cm in Figure 5.13). The positive wake potential (grey line in Figure 5.16) in this region can be coarsely considered as medium that repels ions flow coming from the edge sheath surrounding the object. The conglomeration of the two above mechanisms explain the arise of more pronounced ion focusing region in AQUA case. It has been investigated that the presence of photoelectron affects the polarized object due to non-Boltzmann electron distribution in which the potential variation in the vicinity of the spacecraft becomes stronger compared to case without photoelectrons (Miloch et al. 2008). This investigation can be used to explain the obtained potential fluctuation in Figure 5.16.

5.3 Wake Structure Comparison

As has already shown that the wake width for ERS-1 and ADEOS-II cases appear to be altitude/composition dependence. In order to condirfm this feature, we presented another simulation for AQUA case without involving the photoelectric effect and make comparison shown in Figure 5.17. Since the ion structures of the three cases are insignificantly modified, we only presented the electron structures shown in Figure 5.17.

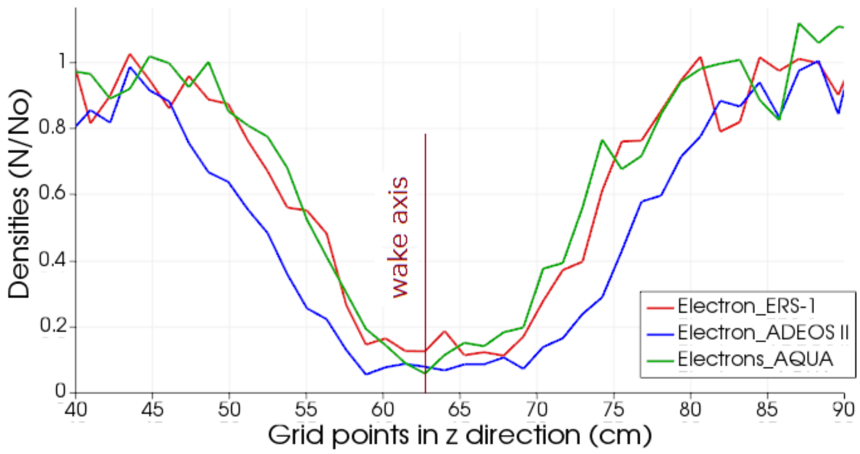

Figure 5.17: The width of wake for 3 ERS-1 (red), ADEOS-II (blue) and AQUA (green) cases in the presence of auroral electrons.

In Figure 5.17, the wake width for ERS-1, ADEOS-II and AQUA are indicated by the red, blue and green lines, respectively. We found a good agreement as previously mentioned that the wake structure changed depending on the altitude and thus ambient density. The similar feature was found by Samir and Wren (1969) in which the wake structure was altitude/composition dependence in spite of the angle of attack. Their study showed that the wake varies as function of the angle of current flow and composition. Conversely, in this study we only imposed the same angle of plasma flow for whole cases, thus the wake structure (wake width) was merely governed by plasma density. We then further related the wake width with temperature and we found that the lower the electron temperature the wider the wake structure.

Another point of interest is the wake structure changes due to the presence of hot auroral electron in case#2. The edge point of ion void region within the wakefield, indicated by P', reduced following the temperature ratio of ion to electron (T_r). These morphologies are shown in Figure 5.18. It is clear that the reduced ion void region in the wakefield for whole cases depends strongly on the temperature ratio between ion and electron (T_i/T_e) rather than the density. The diffusion of ion in the wakefield can occur rapidly due to high temperature of ion. Furthermore, the decreased electron temperature yields lower potential inside the wakefield. The lower temperature of electron effectively shield the potential of the object, thus decreases potential contour as obstacle to ion flows (Engwall et al. 2006).

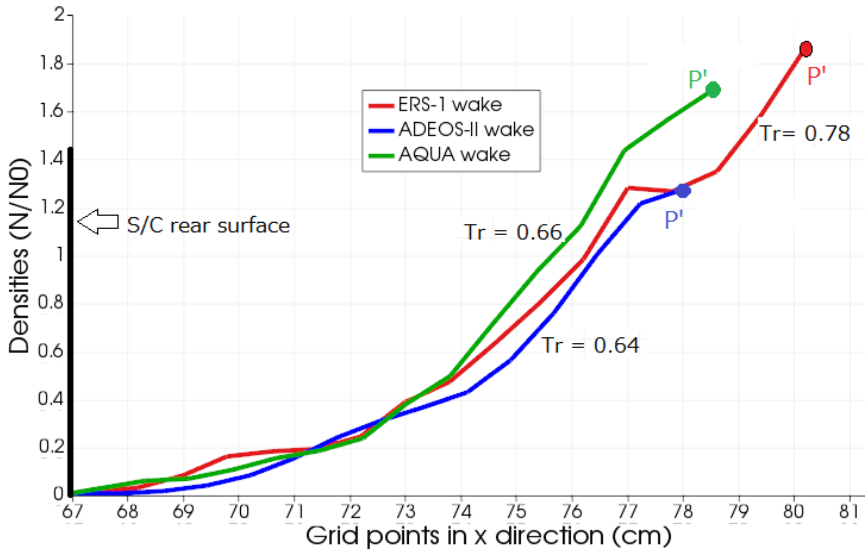

Figure 5.18: The structure of ion void region within the wakefield for ERS-1 (red), ADEOS-II (blue) and AQUA (green) in presence of hot auroral electron. The dotted P' indicates the edge point of balanced ratio of electron to ion inside the wakefield.

The higher the temperature ratio between ion and electron the larger the ion void region within the wakefield. The curves in Figure 5.18 is yielded along the wake centerline behind the object. The edge point P' for ERS-1, ADEOS-II and AQUA cases are represented by the red, blue and green lines, respectively. As previously mentioned that the edge point is determined through the equality of density ratio between ion and electron. In all three cases, we found no clear relation between the edge point and the density. We initially expected that the lower the density, the more shifted inward the edge point toward the object. This discrepancy arises in AQUA case which has larger density than that of in ERS-1 case, but its edge point shifted inward as shown through green line in Figure 5.18.

5.4 Ion Focusing Behind Satellite

5.4.1 The Ion Focusing Region with Fixed Potential

Under particular condition, the ion void region can disappear and turn out to be the ion-rich region (ion focus). In this circumstance, the ion density immediately increases up to at distance several Debye length behind the object. It is found that the ion focus is stronger as the temperature ratio between electron and ions increases (Miloch 2010). The trajectory of ambient plasma especially ions is deflected by stronger electric field inside the sheath edge of the spacecraft.

The issue arises whether the temperature ratio of electron to ion (Te/Ti) is the salient factor governing the ion focus region behind the object, or there must be the other parameters controlling it. Thus, we aim to examine the multiple environmental parameters under particular set of simulation to see which parameter properly contributes to enhanced ion density in the downstream region.

In this simulation, grid points are chosen less than debye length and the particles motion does not exceed the grid point for stability of simulation. The ion and electron mass ratio is preferable close to the real number to depict the density distribution around the spacecraft. We employed total number of grids in each side as 265 grids and set the grid cell width (Δr) to be 0.5 cm . The toal number of time step is 10^5.

The fixed spacecraft potential has been imposed to each case, i.e., -5V, -10V, -15V and -20V. We have simulated 3 cases in which the temperature ratios of electron to ion are 5, 2, and 1.1, respectively as shown in Table 5.5. Here, the density of auroral electron, N_{ae}, in each case is set constant which is $10^6/m^3$. Conversely, the density of ambient plasma varies in each case, covering the lower to higher flux ratio between auroral electron and ambient electron presented in Table 5.5.

Table 5.5: The set of environmental parameters for analyzing the plasma condition in the vicinity of the spacecraft.

Case	T_e	T_i	T_r (T_e/T_i)	N_p (/m^3)	N_{ae} (/m^3)	Γ_r (Γ_{ae}/Γ_e)
1	3750	750	5	10^9	10^6	0.03
2	4000	2000	2	10^8	10^6	0.3
3	4500	4050	1.1	10^7	10^6	2

In Table 5.5, the notation Γ_r represents the flux ratio of auroral electrons (Γ_{ae}) to ambient electrons (Γ_e) and T_r denotes the temperature ratio between electron temperature (T_e) and ion temperature (T_i). In present study, we first performed simulation using varied parameters listed in Table 5.5. To find which parameter prominently contribute to ion focusing, we performed other simulations of which a particular parameter is set varied over time and the remainder are constant.

In all cases the electrons are repelled away from the spacecraft due to higher negative potential. The higher the spacecraft potential, the more electrons are dissociated from the spacecraft shown in Figure 5.19.

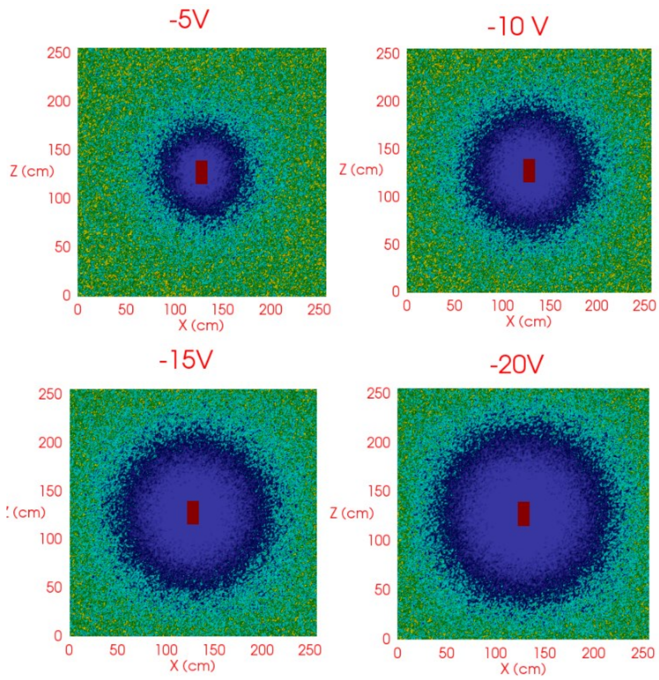

Figure 5.19: The distribution of ambient electrons around the spacecraft for potential of -5, -10, -15 and -20 V, respectively.

In Figure 5.19 the spacecraft is represented by the red-square centralized inside simulation box domain. It is obvious that no boundary effect on electron distribution since quasi-neutrality state is achieved toward the edges of simulation box. Figure 5.19 depicts the potential distribution of case 1. For instance, if we imposed potential of -5V, -10V, -15V and -20V on spacecraft, electrons will depleted omnidirectional around the object at distance ~8λ_D (upper-left), ~10λ_D (upper-right) ,~12 λ_D (lower-left) and ~14 λ_D (lower-right), respectively. This feature overall is seen in case 2 and case 3 where the more negative object potential, the more electrons evacuated from the body.

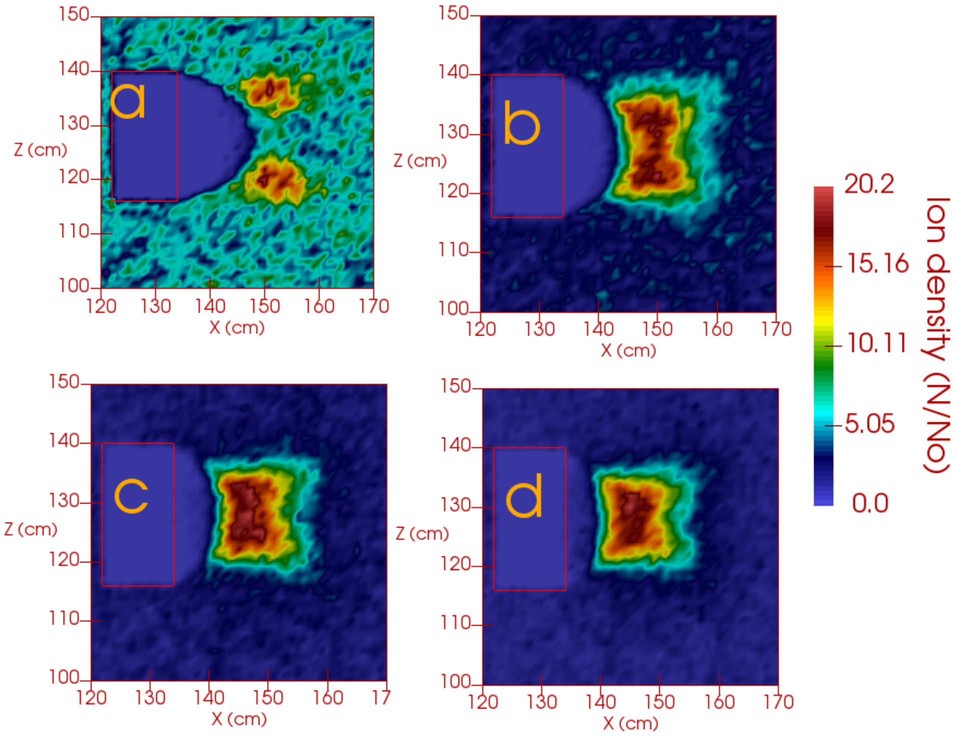

Figure 5.20: Ion focusing structure in the downstream region for case 1.

As the ambient electrons are dissociated away from the object, the density of ambient ions increases especially in the downstream side of the spacecraft shown in Figure 5.20. Here, we present example of ion density variation in case 1 at various potential of -5V to -20V.

In Figure 5.20 we can see that ion focusing regions change over case. The more negative potential of the object creates the pronounced ion-rich region. It is interesting that at potential of -5V, ion-rich region splits up into two triangular shaped structures shown at lower-left panel of Figure 5.20. Initial two separated structures begin merging toward the wake centerline and compressing the initial ion void structure as seen at upper-right panel of Figure 5.20. Distortion of ion void structure is stronger as the potential much more negative attracting more ion inward the object shown at lower-left panel of Figure

5.20. The formation of ion focusing region established of which the ion void structure gradually disappears shown through Figure 5.20 (upper-right panel).

In addition, we attempt to look up ion-rich formation in the downstream region at potential of -5V for case 1 to case 3 shown in Figure 5.21. It is obvious that at the same potential, as the temperature ratio (T_r) decreases the more ion-rich region fade away leaving the initial ion void structure. In Figure 5.21 the ion concentration starts dispersing in case 2 and case 3 and scatters fulfilling the near wake region shown through case 3. Thus, we can infer that increasing T_r drives the ion consentration more compact and more focus in certain region which its evolustion can be clearly seen through case 2 and case 3.

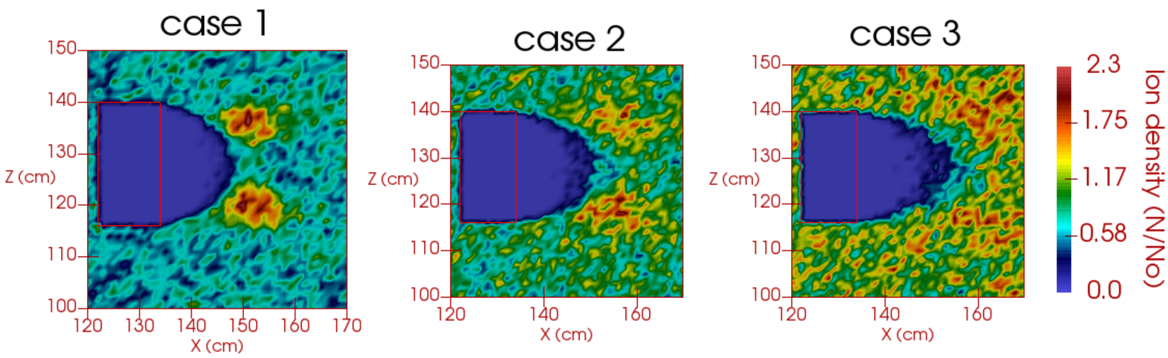

Figure 5.21: The formation of ion-rich region in the downstream region at potential of -5V for all cases listed in Table 5.5.

In all cases, it is found a good agreement that ion void region, a region with negative potential where the density of electrons is much higher than that of ions, gradually disappears and turn out to be ion-rich/ion focusing region. The higher the temperature ratio and/or the magntitude of negative potential, the more ion concentrated forming ion focusing behind the object shown through Figure 5.20 and Figure 5.21. The distortion of ion void structure in Figure 5.20 relatively small from ~$2\lambda_D$ (upper-left) to ~$1.5\lambda_D$ (upper-right), $0.9\lambda_D$ (lower-left) and $0.5\lambda_D$ (lower-right).

The trendlines of ion focusing which increases along with increasing temperature ratio have been found at the potential of -10, -15 and -20 V. Thus, in case where the potential of the object is identical, the ion focusing is dominantly characterized by temperature ratio. However, the temperature ratio is not the only one factor characterizing the ion focusing structure. Aforementioned simulations cleary show this signature in which the change of object potential can attract more ions and accelerate ions to fill up the initial ion void region. This signature can be seen through the shifted ion density lineplot in

Figure 5.22 closer toward the object. In this figure, the spacecraft resides at grid points of 122 cm ≤ x ≤ 134 cm and only part of simulation box domain is shown.

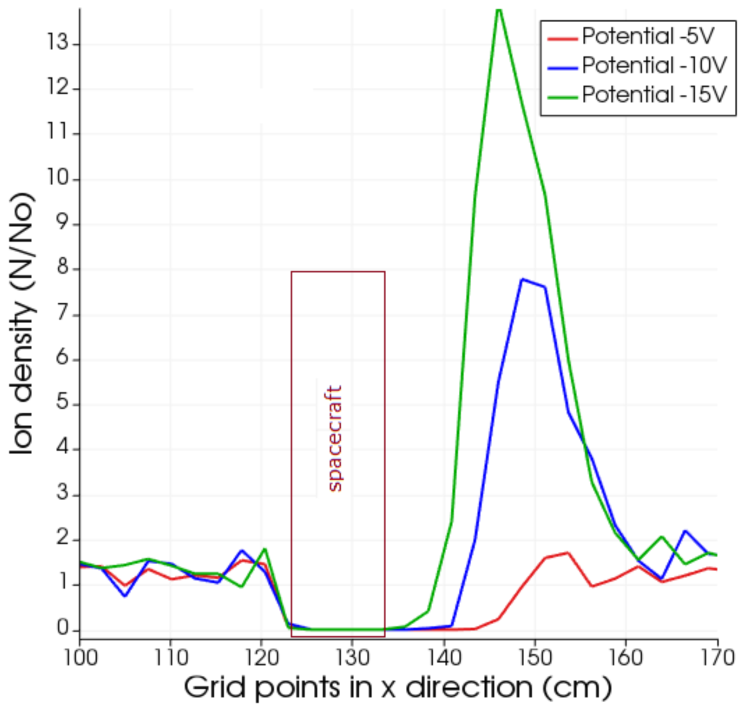

Figure 5.22: The ion density enhancement in the downtream side as the magnitude of negative potential increases from 5 to 15 V for case 1.

As previously mentioned that we attempted to examine which parameter dominantly contributes to ion-rich region by performing additional simulations of which some parameters are set constant. In these simulations, we set the parameters as follows.

1. Change the electron temperature (T_e), and let the other parameters remain constant (case 4)
2. Only the ion temperature (T_i) fluctuates (case 5).
3. Only the ambient plasma density (N_p) changes (case 6)
4. Only auroral electron density (N_{ae}) varies (case 7)

The setup of each case can be seen in Table 5.6 and the ion density profiles can be seen in Figure 5.23 to Figure 5.27.

Table 5.6: The set of environmental parameters for case 4 to case 7

Case	T_e	T_i	T_r (T_e/T_i)	N_p (/m^3)	N_{ae} (/m^3)	Potential (V)
Case 4						
a	3750	2000	1.9	10^8	10^6	-5
b	4000	2000	2	10^8	10^6	-5
c	4500	2000	2.3	10^8	10^6	-5
Case 5						
a	4000	1250	3.2	10^8	10^6	-5
b	4000	2000	2	10^8	10^6	-5
c	4000	2750	1.5	10^8	10^6	-5
Case 6						
a	4000	2000	2	10^9	10^6	-5
b	4000	2000	2	10^8	10^6	-5
c	4000	2000	2	10^7	10^6	-5
Case 7						
a	4000	2000	2	10^8	10^5	-5
b	4000	2000	2	10^8	10^6	-5
c	4000	2000	2	10^8	10^7	-5
d	4000	2000	2	10^8	10^8	-5

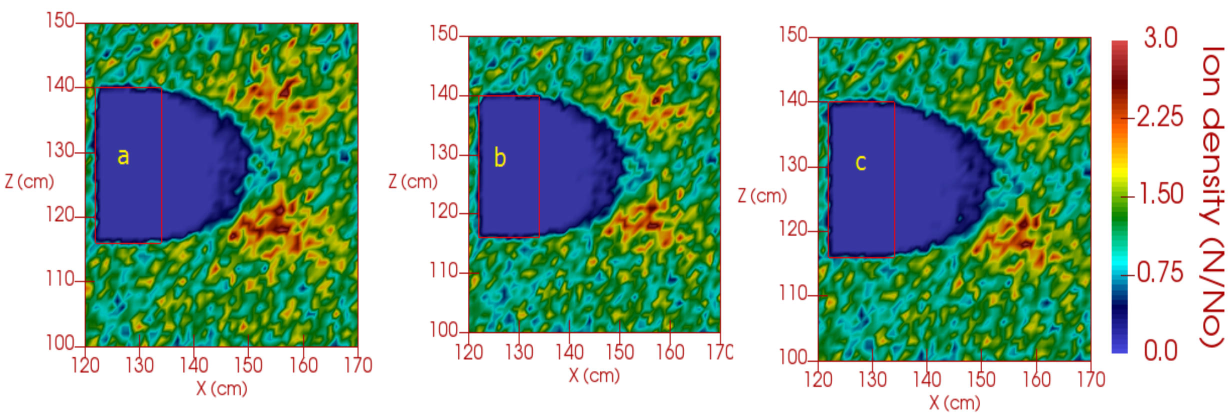

Figure 5.23: The ion focusing structure for case 4. The temperature ratio varies through electron temperature, whereas the rest of parameters remain unchanged.

In Figure 5.23, by setting the electron temperature changes over case, we can not see its contribution to modify the ion-rich structure. The ion focusing structure in each case shows similar pattern and no distortion occurs. We initially presumed that the higher the electron temperature the more ion focused in the downstream side as shown in previous simulation, but the case 4b and 4c in Figure 5.23 do not show this feature. It is also pronounced that the ratios of temperature also increase over case. Thus, the variability of electron temperature ratio insignificantly contributes to ion-rich region. Furthermore, we examined the fifth case of which the ion temperature changes over case, while the rest of parameters are contant. The result of simulation is shown in Figure 5.24.

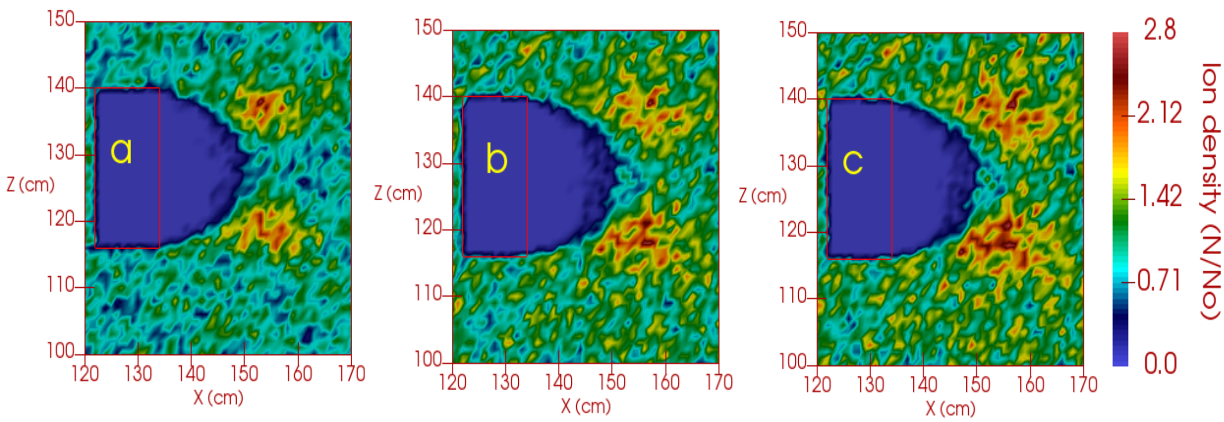

Figure 5.24: The ion focusing structure for case 5. The temperature ratio varies through ion temperature and the other parameters are constant.

Figure 5.24 presents the comparison of ion focusing for case 5 using three condition tabulated in Table 5.6. The contributions of ion temperature changes (T_i) as well as the temperature ratio (T_r) are not obvious to modify ion focusing structure. The good indicator to see this feature comes from the fact that the two separated ion structures in Figure 5.24 do not conjoin together forming an integrated structure rather detach at upper and lower sides of the object. It is important to point out that there exists local change on two-ion focusing structure, but this change is very small and can be omitted. We next performed simulation on the sixth case based on parameters listed in Table 5.6 and the result can be seen in Figure 5.25.

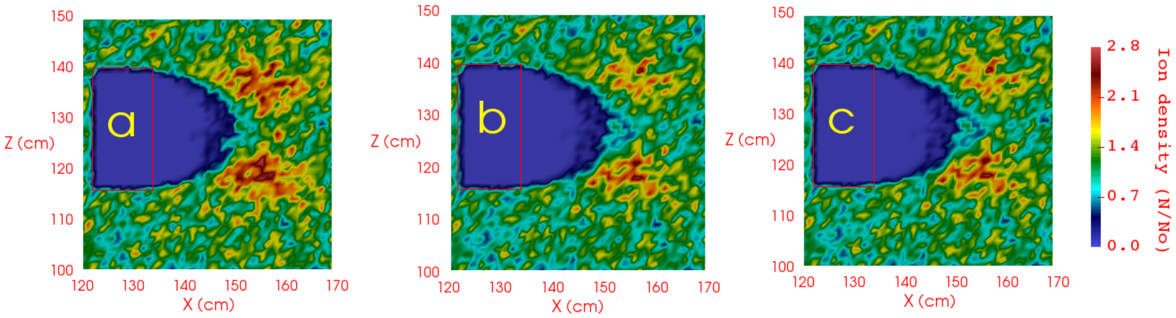

Figure 5.25: The ion focusing structure for case 6. The ambient plasma densitiy temperature ratio varies and the other parameters are constant.

Figure 5.25 shows the ion density enhancement of which ambient plasma density degrades over case presented in Table 5.6. Here, we see the ion density starts to concentrate toward the wake centerline as shown in Figure 5.25a. The structure of ion focusing expands and becomes wider compared to other cases (6b and 6c). The outgrowth of ion focusing structure from case 6b to case 6a can be seen in Figure 5.26. We plot contour map at the particular regions (indicated by two-brown circle area) of case 6a and 6c to see the obvious contortion of ion structure over ambient density distortion.

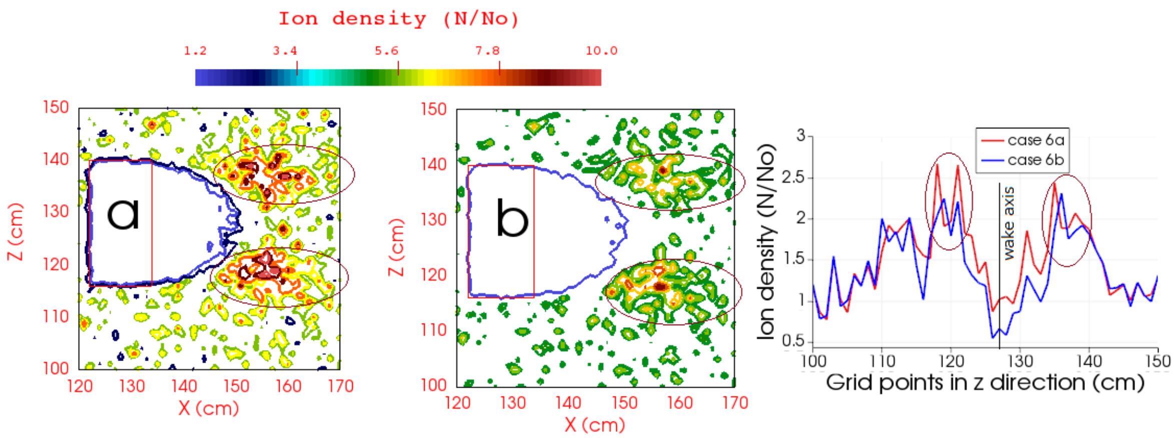

Figure 5.26: The contour map of ion focusing structure evolution as the ambient density decreases in case 6a and 6b.

Figure 5.26 gives insight into ion-rich region dispersion as the ambient density decreases. The difference of ion density peak in brown circle areas is shown through the line plot at the right panel of Figure 5.26. Inspite of more scattered, this structure is also more compact as the ambient plasma density increases. The higher the ambient plasma density meaning the lower the density ratio of auroral electron to ambient plasma, the more noticeable ion focusing structure behind the object. Thus, the variation of ambient plasma density can be one of candidates contributed to ion-rich region structure. We further examined whether the density ratio of auroral electron to ambient plasma density significantly contributes to ion focusing through case 7 shown in Figure 5.27.

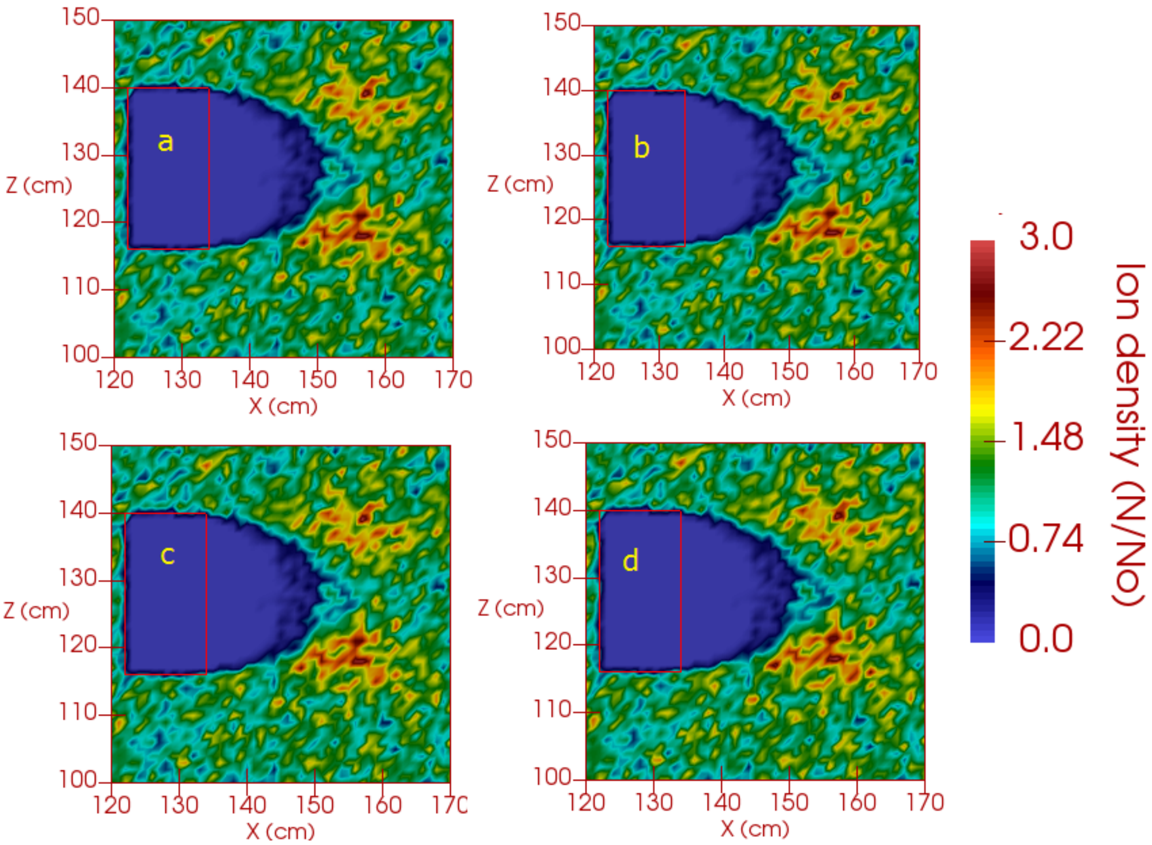

Figure 5.27: The structure of Ion focusing for case 7. The auroral electrons density changes, whereas the other parameters are constant.

It is interesting that the variation of auroral electron density overall insignificantly contributes to ion density enhancement in the downstream region. The features of all cases are alike of which two separated ion concentration regions do not expand toward the wake centerline rather than have relatively static structure. It is so contrast if we compare to previous case of which the ion focusing is likely depending on the density ratio of auroral electrons to ambient plasma. However, simulation in case 7 emphasizes that the density ratio plays insignificant role in driving ion focusing structure. Nevertheless, we infer that the variation of ambient plasma density in the vicinity of the spacecraft contributes to local ion focusing in the form of two-ion streamers.

The interaction between spacecraft and ambient plasma together with precipitating auroral electrons in LEO environment is quite complex since their distribution is highly non-maxwellian distribution. However in most cases, maxwellian distribution is chosen as basic assumption for practical purposes. Here, if the spacecraft is exposed to very low potential relatively to surrounding plasma, a wake formed and ion void region are created due to effect of mesosonic motion. This effect arises since spacecraft motion is faster than ion thermal motion, thus it takes time for ions to fill up the ion-void in the wakefield. However, under particular condition the ion void region consisting of negative potential can be distorted especially when the spacecraft potential becomes much lower.

The physics of ion focusing has been described well which is related to ambient polar electric field due to presseure or density gradient in the wake region. The formation of ion focusing structure can be illustrated through Figure 5.28.

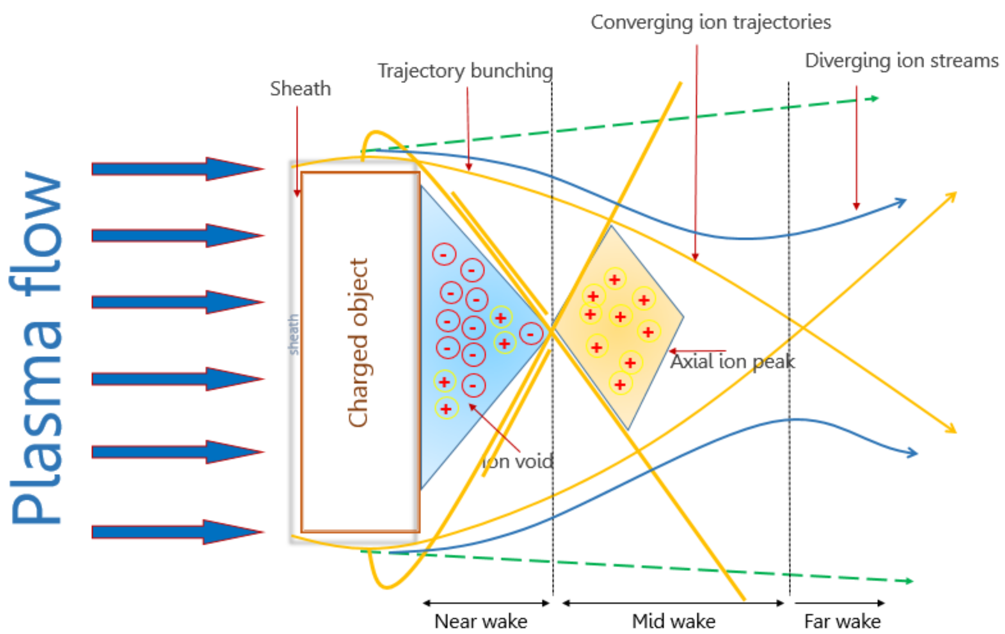

Figure 5.28: The formation of ion focusing structure in the downstream region of the spacecraft. The schematic picture is taken from Stone (1981) with little modification for adjustment.

Flowing plama through the solid object creates an ion compression in the ram side (in front of spacecraft body). Ions will be directed and accelerated by electric field induced by the object with supersonic motion. The density of ion increases in this side, whereas the electron density drops creating sheath. A clear indicator for sheath region is designated through the drop of density ratio of ions to electrons in the ram side. As has previously mentioned that the effect of mesosonic motion results in ion void region in the downstream region. In contrast to upstream region, the electrons dominantly scatter giving rise to negative potential inside the ion void region.

At the sheath edges of the body (upper and lower), the ion trajectories passing these small regions start to be deflected by the electric field in the sheath edges. As the ions continuously experience the electric field along its motion into the downstream region, their trajectories will conjoin each other alongside or around the wake centerline creating an area with high concentration of ions (ion focusing). The further effect of this focusing, ion repopulation in the wakefield can occur. Due to negative space potential inside the ion void region, the repopulated ions migrate toward the object of which the migration rate is potential dependence. During this state, there exists density gradient in the downstream region as shown by all cases in this study. The proximated mechanism of ion focusing subject ot two separated ion structures in this study can be seen in Figure 5.29.

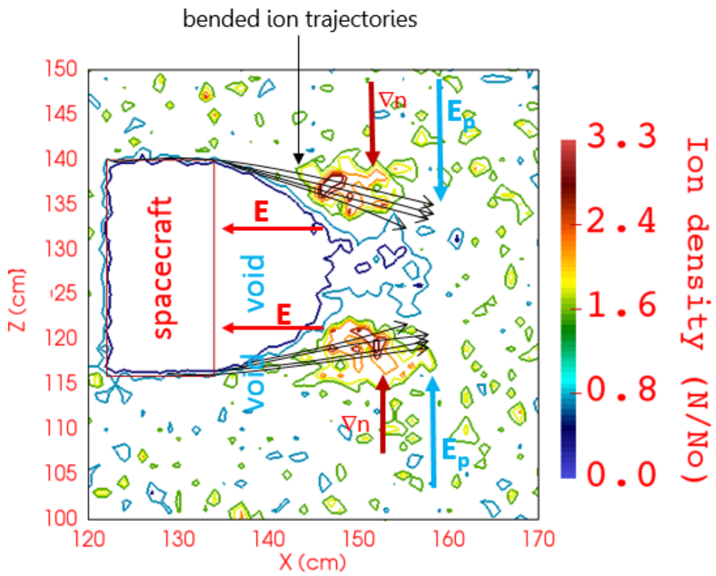

Figure 5.29: The possible mechanism of two ion structures in most cases in this study. This picture samples the simulation on case 1 with potential of -5V.

Figure 5.29 portrays the ion trajectories bunching in the wakefield. The ion trajectories are deflected by elecric field inside the sheath edges. The arise of density gradient (∇n) in the wakefield leads to ambipolar diffusion of plasma where the ions are accelerated and then directed by ambipolar electric field ($\mathbf{E_p}$) in such a direction toward the wake centerline. Without ion deflection, in principal there exists ion density rarefaction expanding down to the downstream region of which its angle (θ) proportionally to mach number (M). Since the ion density increases as θ decreases (Wang and Hastings 1992), overall cases in present study show an increasing ion density in the wake region. However, the rarefaction of ion density is violated and turns out to be two ion-rich structures. In Figure 5.29, the confluence of ion trajectories generated from both edges does not occur remaining two separated structures.

As the magnitude of spacecraft potential becomes larger, the contribution of ion focusing formation not only comes from ambipolar electric field generated by plasma diffusion in the wakefield, but also comes from the electric field generated by spacecraft (**E**). This electric field become stronger as the potential decreases. The resultant of electric field, in spite of leading to ion focusing formation through trajectory deflection, it also attracts the deflected ions toward the spacecraft minimizing the ion void structure. This mechanism explains the expansion of ion focusing structure radially inward shown in Figure 5.20 as the potential of the object becomes more negative.

Simulaton done by setting the fixed potential on the spacecraft and let a particular parameter fluctuate showed that T_r through variation of T_e and T_i (case 4 and 5) together with N_{ae} (case 7) insignificantly lead to ion focusing formation. However, the variation of ambient plasma density around the object can modify the local ion focusing structure in the form of two-ion streamers. Although the density ratios of auroral electrons to ambient plasma in case 7 vary resembling case 6, it does not affect the ion focusing structure due to static ambient density.

Furthermore, we found no strong relation between variation of temperature ratio and ion focusing formation. We should point out that we refer the term of ion focusing as ion-rich region as part of repopulated ions that distorts ion void structure in the wake region. Thus, it occurs when two ion-streamers at upper and lower edges of spacecraft incorporate and migrate toward the spacecraft. Instead, the two ion streamers at upper and lower edges of an object are referred as local ion focusing.

The dependence of ion focusing formation on temperature ratio is not clear from this study. It is so contrast to other study such as Miloch (2010) that found ion focusing is T_r dependence. We admit that the variation of temperature ratio only affects the local ion focusing structure as result of electriec field effect from the sheath edges of the object in addition to plasma diffusion due to density gradient in the downstream region. The only parameter that contributes to ion focusing is potential change in which the more negative object potential, the resultant of electric field generated by spacecraft potential and ambipolar electric field yielded by ambipolar diffusion of plasma will accelerate and govern ions into ion void region giving rise to repopulated ions in the wakefield. This feature is obviously shown through Figure 5.20.

5.4.2 The Ion Focusing Region with Floating Potential

In this simulation we tried to get the floating potential and then see its effect on ion focusing region in the downstream side. We performed two scenarios, i.e., in the absence of auroral electrons (case 1) and in the presence of auroral electrons (case 2). We intentionaly set the varied parameters in each case as listed in Table 5.7.

Table 5.7: The set of environmental parameters for case without auroral electrons

Case 1	Te	Ti	Te/Ti	Np ($/m^3$)	Te/Np $K.cm^3$	Potential (V)
#1	3247	2548	1.2	4.10^{10}	0.08	-2.1
#2	2530	1611	1.6	10^{10}	0.25	-1.6
#3	2116	1473	1.4	$4.67.10^{10}$	0.05	-1.5

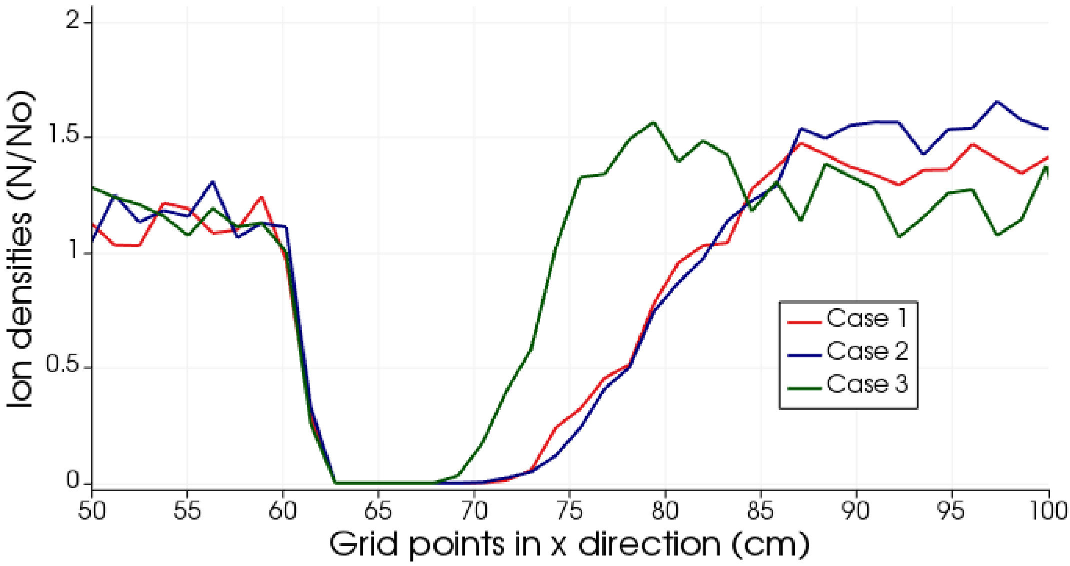

Figure 5.30: The ion density variation in the downstream region for cases without auroral electrons.

In case of without auroral electrons, the ion-rich region formation in the downstream side is independence on temperature ratio as well as potential. For instance, in case 2 the temperature ratio as well as the magnitude of potential are higher than that of in case 3, but the ions in case 3 is more focused compared to case 2 shown in Figure 5.30. There is good agreement between temperature to density ratio ($T_{rn} \sim T_e/N_p$) and ion focusing as well as ambient density (N_p), i.e., the lower T_{rn} or the higher N_p the more ions focused in the wakefield. However, we are intereseted in performing in case of auroral electrons inclusion listed in Table 5.8.

Table 5.8: The set of environmental parameters for case with auroral electrons

Case 2	Te	Ti	Te/Ti	Np (/m^3)	Nae (/m^3)	Te/Np K.cm^3	Potential (V)	Γ_r (Γ_{ae}/Γ_p)
#4	3247	2548	1.2	4.10^{10}	10^6	0.08	-2.3	6.10^{-3}
#5	2530	1611	1.6	10^{10}	10^6	0.25	-2.2	3.10^{-2}
#6	2116	1473	1.4	$4.67.10^{10}$	10^6	0.05	-2.5	7.10^{-3}

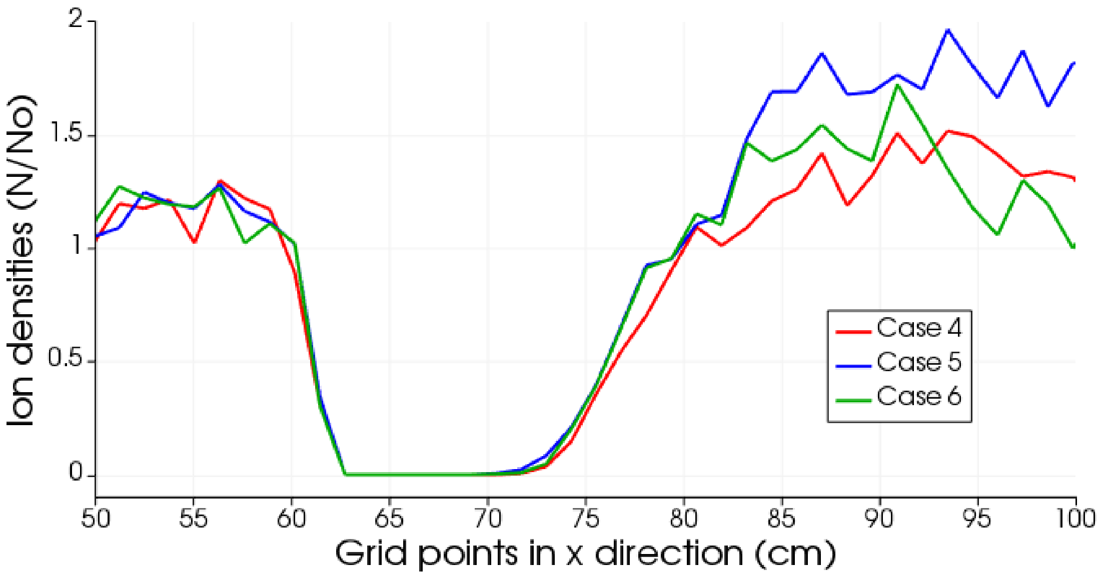

Figure 5.31: The ion density variation in the downstream region for cases with auroral electrons.

In Figure 5.31 it is clear to see that as the temperature ratio (T_r) increases, the more ions concentrated in the downstream. It is also interesting to know that temperature to density ratio (T_{rn}) and ambient plasma density (N_P) insignificantly contribute to ion focusing. In previous case without auroral electrons, the T_{rn} as well as N_p play role to ion focusing formation. In this case, the potential again does not have contribution to ion focusing. However, since the potential depends on flux or current balance, we tried to calculate analytically the flux ratio between auroral electron and ambient plasma as listed at column 9 (Table 5.8). We found that the higher Γ_r the more ion focused shown in Figure 5.31.

The ion focusing phenomena is related to repopulated ion mechanism. Due to mesothermal motion of plasma in LEO, ions are unable to populate the near wakefield instantly, thus the mobile electrons take over inhabiting the ion void region. As consequence, there exists local negative disturbance at particular distance behind the object. Since this region consists of negative potential distribution, it pulls ions into the wakefield and repels incoming electrons giving rise to ion re-population as illustrated in Figure 4.41 . It is important to note that re-population inside the wakefield due to ion trajectory deflection lead to density gradient as ions displace to fill the wake.

As the plasma flows toward the spacecraft impinging on the edge sides of body, rarefaction wave is formed that propagates with ion sound speed radially (perpendicular to spacecraft motion) away from the object. The moving object then results in such cone, called mach cone, produced by boundary of rarefaction region in which its angle is electron temperature and velocity dependence.

The resulted density gradients lead to ambipolar diffusion by ambipolar electric field. It is knowledgable that ambipolar electric field contributes to destroy quasi-neutrality in plasma. As the electrons move faster than ions inside the wakefield, it leads to charge separation creating ambipolar electric field in such direction, e.g. particle diffusion direction, to decelerate electron mobility and accelerate ion, thus both species approximately diffuse at the same rate.

Since the ion void depends on the potential of the object, the much lower potential will exert a force to ions giving rise to more attracted ions into void region. The electric field plays role in defocusing ion trajectory. It notes that ion focusing is strongest in particular region, e.g. symmetic area shown in Figure 5.28. At the sheath edge of body, the ions trajectories start bending toward the focusing area (orange) and continue to be affected by the electric field as they move closer void edges. Close to the focused region, they come across deflected ions from other sheath edge of body. The ion trajectories become convergence leading to ion-rich region. Here, some portions of ions cross the ion peak density region (orange), whereas other ions are deflected by the positive space-charge near a region called mid-wake. In this region ions repel each other and shift further into the deeper downstream region called far-wake. Inside this region the ion streams become divergence.

Chapter 6

Summary and Conclusions

6.1 Summary

In this study, we have diagnosed the failures on LEO spacecraft by using geophysical parameters and investigated the failures related charging including the downstream-plasma structure by performing PIC EMSES simulation.

LEO spacecraft failures

We have found that approximately 60 % of failures in this study were strongly related to lower energy electron fluxes of 30-100 keV as well as its associated magnetic perturbations through Kp and Dst indices. There was tendency of failures following three patterns, i.e., occurred during the main phase of magnetic storm (pattern 1) suffered by Asca satellite (case #2) ; concided with the recovery phase of storm (pattern 2) as shown in Fuse 1 (case #4), Dart (case #12) and Monitor-E (case #13); attributed to multiple storms prior to and after the anomaly day (pattern 3) such as in Radarsat 1(1) (case #7), Terra (case #3), Yohkoh (case #5b), Radarsat 1(2) (case #8), Landsat 7 (case #9), Icesat (case #10) and Midori (case #11). We also pointed out that amongst these three patterns, LEO spacecraft failures were mostly linked to pattern 3 (40 %). The remaining cases such as in Fuse 1(2) (case #5a), Aqua (case #6) and Kirari to Orbcomm (case #14 to case #19), it seems that the failure occurences were weakly linked to geophysical parameters used in this study. Nevertheless, we can not say that the contribution of lower energy electron fluxes and its associated geomagnetic disturbances did not play role in these cases. This argument referred to failure on Fuse 1(2) (case #5a) where its failure resembled the Fuse 1(1) (case #4) malfuction. It might be the further effects of the initial damage on Fuse 1 satellite.

The determination of satellite local time through longitude of acending node (LAN) parameter resulted in small deviation between local time –SND derived and local time – Extracted TLE which is less than 2 minutes. It indicates that LEO spacecraft failures in this study occurred around ascending phase of satellites. Although LAN parameters changes over time, but its oscillation is very small per day. It only affects the calculation of minutes and seconds, but not in hours of local time from method used in this study (Table 4, column 4). Since this parameter can represent the position of satellite relative to the sun, so it is relevant to determine the mean local time of satellite with respect to the sun in association with energetic particles injection in the nightside magnetotail.

Furthermore, the satellite local time distribution of LEO failures in this study shows that failures were scattered dominantly within two sectors, i.e., pre-dusk and pre-midnight confining to migration of low energy electrons in the nightside of magnetosphere. The events predominantly occurred from dusk to dawn sectors of magnetic local time (65 % of occurrences). During the migration, energetic electrons were accelerated in the magnetotail plasma sheet and drifted into the ring current. A large portion of these energetic electrons, with complex mechanisms, were lost and precipitated into upper atmosphere where LEO satellite immersed in it. It can be seen through fluxes variation of lower energy channels as a result of magnetic perturbations represented by Kp and Dst indices.

LEO Spacecraft Charging and Wake Structure

We have performed PIC EMSES simulation to get the level of charging and structure of plasma wake in the downstream region by using some LEO satellites. In the absence of auroral elctrons, i.e., only accounted the ionospheric plasma impact on spacecraft (undisturbed plasma condition), the average floating potential has a good agreement with other studies which is less than 3V (negative). In most cases, both electron and ion flow in mesosonic motion, i.e., electron flows subsonically and ion flow supersonically, leaving such ion void region in near-wake region behind the spacecraft. The ion void inside the near-wake region varies depending on the body potential. The higher the magnitude of negative potential, the more distorted the ion void toward the object in the downstream region. In addition, one additional interesting feature is the floating potential dependence on electron temperature rather than ambient plasma density. The varied temperature of electron from 20 LEO satellite cases showed that as the electron temperature becomes higher, the floating potential on LEO satellite decreases with confidence level reaching 99%.

Simulation by involving the impact of auroral electrons on the spacecraft samples some LEO satellites. Interestingly that the presence of auroal electrons insignificantly contributes to higher charging due to small ratio of flux between auroral electron and ambient electron. As consequence, the wake structure inconsiderably modified and only distorted the ion void structure inward as the magnitude of negative potential increases. This features are seen through the shifted edge points in the presence of auroral electrons case. By increasing the density of auroral electrons, e.g. ERS 1 case, so that the flux ratio between auroral electrons and ambient electrons is unity does not give high voltage charging, only the order of less than 20V (negative). The insignificance charging might be come from the simulation in which the steady state floating potential has not reached yet due to time-consuming simulation. However, another feature, i.e., ion focusing arises in spite of ion void structure in the wakefield. We guess that it is related to ion trajectory deflection by the electric field as the potential of the spacecraft becomes much more negative. The confluence of deflected ion trajectories results in ion-rich region at particular distance from the object.

The inclusion of photoelectrons together with auroral electrons during daytime passage in this study gives rise to more ion focused region in the downstream region. It is interesting that the space potential in the mid-wake increases leading to positive potential. We suggested that it turns to be a barrier for ions leading to ion-back flow toward the near-wake region enriching ion density there.

The existence of ion focusing in the downstream region is more pronounced through multi simulations in this study covering cases with fixed and floating potentials. Regarding the fixed potential case, it is obvious that the ion focusing feature is temperature ratio and potential dependence. The larger temperature ratio and/or the lower potential the more pronounced ion focusing region in the wakefield, and vice versa. However this relation becomes unclear in case of floating potential especially in the presence of auroral electrons. Nevertheless, the general signature is found of which the flux ratio between auroral electrons and ambient plasma plays role in focusing ion inside the wakefield. The higher this flux ratio the more ion focused in the downstream region. The contribution of flux ratio to ion focusing is presumably related to ambi polar electric field as a result of density gradient of ions which diffuse and accelerate in the downstream region.

6.2 Future Works

Simulation Box Domain

In this study we employed limited size of simulation box domain, i.e., 128 cm^3 and 64 cm^3 for grid cell size (Δr) of 1 cm and 0.25 cm, respectively. This size of simulation box generally acommodates lower charging on the solid body, thus the evolution of wake structure in the downstream region is still observable. In contrast, for high level charging body, it is necessary to employ larger size of simulaton box with smaller grid cell size to avoid the boundary effects on the object and to capture the plasma wake evolution clearly with fine resolution. This effort is surely time-consuming simulation.

Other Currents Effect on the Object

Overall the simulation in this study only considers the effect of ambient plasma, auroral electrons and photoelectrons on the spacecraft and neglects other effects coming from back-scattered and secondary electrons which also contribute to spacecraft charging. Although in most cases their contribution is relatively small especially on LEO environment, omitting their effects on the spacecraft lead to floating potential calculation to shift little bit negative.

Spacecraft Geometry

Throughout simulation, the spacecraft is assumed as box-shaped with dimensions of the order of cm and material is perfectly conductor. However, it is needed to perform simulation by using spacecraft-like size on the order of meter (m) covering not only conducting body but also non-conducting body.

Multi Body Effect of Interaction

The simulation hitherto only performs single solid body interaction immersed in plasma, thus the potential as well as the resulted wake structure is purely as a result of interaction with single object. It is interesting to see how multiple objects immersed in plasma interact each other affecting the wake structure formation around these objects.

Bibliography

Ahmad N, Herdiwijaya D, Djamaluddin T, Usui H, Miyake Y (2018) Diagnosing low earth orbit satellite anomalies using NOAA-15 electron data associated with geomagnetic perturbations, Earth, Planet and Space, 70:91. https://doi.org/10.1186/s40623-018-0852-2

Ahmad N, Usui H, Miyake Y (2018) Particle in Cell Simulation to Study the Charging and Evolution of Wake Structure of LEO Spacecraft. Part of chapter Communications in Computer and Information Science, Methods and Applications for Modeling and Simulation of Complex Systems book 946 : 255-268. http://dx.doi.org/10.1007/978-981-13-2853-4_20

Ahmad N, Usui H, Miyake Y (2018) The Particle-In- Cell simulation on LEO spacecraft charging and the wake structure using EMSES. In: Proceeding of , the 37th JSST Annual International Conference on Simulation Technology, page 109-112.

Ahmad N, Usui H, Miyake Y (2019) The Particle-In- Cell simulation on LEO spacecraft charging and the wake structure using EMSES. Accepted in Journal of Advanced Simulation in Science and Engineering (JASSE) on January 7, 2019.

Al'pert YL (1983) The near-Earth and interplanetary plasma : plasma flow plasma waves and oscillations, vol 2. Cambridge University Press, New York.

Anderson PC, Koons HC (1996) Spacecraft charging anomaly on a low-altitude satellite in an aurora. J Spacecraft Rockets 33(5):734–738. https://doi.org/10.2514/3.26828

Anderson PC (2012) Characteristics of spacecraft charging in low Earth orbit. J Geophys Res 117:A07308.https://doi.org/10.1029/2011JA016875

Andriyas T, Andriyas S (2015) Relevance vector machines as a tool for forecasting geomagnetic storms during years 1996–2007. J Atmos Terr Phys 125-125: 10-20. https://doi.org/10.1016/j.jastp.2015.02.005

Asikainen T, Mursula K (2008) Energetic electron flux behaviour at low L-shells and its relation to the South Atlantic Anomaly. J Atmos Terr Phys 70:532–538

Asikainen T, Mursula K (2013) Correcting the NOAA/MEPED energetic electron fluxes for detector efficiency and proton contamination. J Geophys Res 118(10):6500–6510. https://doi.org/10.1002/jgra.50584

Belov A, Dorman L, Iucci N, Kryakunova O, Ptitsyna N (2005) The relation of high- and low-orbit satellite anomalies to different geophysical parameters. In: Daglis IA (ed) Effects of space weather on technology infrastructure. Part of the NATO sciences series II: mathematic, physics and chemistry book series, vol 176. Kluwer Academic Publishers, Dordrecht, pp 147–163

Birdsall CK, Langdon AB (1985) Plasma physics via computer simulation. McGraw-Hill, New York.

Choi HS, Lee J, Cho KS, Kwak YS, Cho IH, Park YD, Kim YH, Baker DN, Reeves GD, Lee DK (2011) Analysis of GEO spacecraft anomalies: space weather relationship. Space Weather 9(6):1–12. https://doi.org/10.1029/2010SW000597

Colson A (2011) DMSP spacecraft charging in auroral environments, NASA USRP – Internal Final Report, MSFC. Accessed 25 December 2017.

Cooke DL (2000) Simulaton of an auroral charging anomaly on the dmsp satellite. In : 6th Spacecraft Charging Technology Conference, AFRL-VS-TR-20001578

Davis VA, Mandel MJ, Cooke DL, Enloe CL (1999) High‐voltage interactions in plasma wakes: simulation and flight measurements from the Charge Hazards and Wake Studies (CHAWS) experiment. J Geophys Res 104(A6) :12445-12459. https://doi.org/10.1029/1998JA900071

DeForest SE (1972) Spacecraft charging at synchronous orbit. J Geophys Res 77 (4): 651-659. https://doi.org/10.1029/JA077i004p00651

Dorman LI, Belov AV, Eroshenko EA, Gromova LI, Iucci N, Levitin AE, Parisi M, Ptitsyna NG, Pustil'nik LA, Tyasto MI, Vernova ES, Villoresi G, Yanke VG, Zukerman IG (2005) Different space weather effects in anomalies of the high and low orbital satellites. Adv Space Res 36(12): 2530-2536. https://doi.org/10.1016/j.asr.2004.05.007

Engwall E, Eriksson AI, Forest J (2006) Wake formation behind positively charged spacecraft in flowing tenuous plasmas. Phys. Plasmas 13 (062904). https://doi.org/10.1063/1.2199207

Eriksson AI, Wahlund JE (2005) Charging of a conductive spacecraft in the auroral zone. In : Proceeding of the 9th Spacecraft Charging Technology Conference – 2005, JAXA-SP-05-001E.

Evans R, Garret H, Gabriel S, Whittlesey A (1989) A preliminary spacecraft charging map for the near Earth environment. In: Olsen RC(ed) Proceedings of the spacecraft charging technology, vol 2, Monterey, CA.

Evans DS, Greer MS (2004) Polar orbiting environmental satellite space environment monitor-2: instrument description and archive data documentation. NOAA technical memorandum OAR SEC 93. Available at ftp://satdat.ngdc.noaa.gov/sem/poes/docs/sem2_docs/2006/SEM2v2.0.pdf Accessed 21 November 2017

Farthing WH, Brown JP, Bryant WC (1982) Differential spacecraft charging on the geostationary operational environmental satellites. NASA technical memorandum 83908. Available at https://ntrs.nasa.gov/archive/nasa/casi.ntrs.nasa.gov/19820018480.pdf.

Accessed 7 November 2017

Fennell JF, Koons HC, Roeder L, Blake JB (2001) Spacecraft charging: observations and relationship to satellite anomalies. In: Harris RA (ed) Proceeding of the seventh international conference, ESTEC, Noordwijk, the Netherlands, 23–27 April 2001

Frooninckx TB (1991) High-latitude spacecraft charging in low-earth polar orbit, AD-A249868.

Frooninckx TB, Sojka JJ (1992), Solar cycle dependence of spacecraft charging in low Earth orbit. J Geophys Res 97(A3): 2985-2996. doi:10.1029/91JA02704

Garret HB, Whittlesey AC (2012) Guide to mitigating spacecraft charging effects. John Wiley & Sons, Inc., Hoboken, New Jersey.

Gonzales WD, Joselyn JA, Kamide Y, Kroehl HW, Rostoker G, Tsurutani BT, Vasyliunas VM (1994) What is geomagnetic storm? J Geophys Res 99(A4):5771–5792. https://doi.org/10.1029/93JA02867

Gubby R, Evans J (2002) Space environment effects and satellite design. J Atmos Terr Phys 64(16):1723–1733. https://doi.org/10.1016/S1364-6826(02)00122-0

Gussenhoven MS, Hardy DA, Rich F, Burke WJ, Yeh HC (1985) High-level spacecraft charging in the low-altitude polar auroral environment. J Geophys Res 90(A11):11009–11023. https://doi.org/10.1029/JA090iA11p11009

Hastings DE (1995) A review of plasma interactions with spacecraft in low Earth orbit. J Geophys Res 100(A8):14457–14483. https://doi.org/10.1029/94JA03358

Hastings D, Garret H (1996) Spacecraft environment interaction. Cambridge University Press, Cambridge

Horne RB (2001) Benefits of a space weather programme. ESA Space Weather Programme Study Alscatel Consortium, WP1100. Accessed 3 September 2018.

Iucci N, Dorman LI, Levitin AE, Belov AV, Eroshenko EA, Ptitsyna NG, Villoresi G, Chizhenkov GV, Gromova LI, Parisi M, Tyasto MI, Yanke VG (2006) Spacecraft operational anomalies and space weather impact hazards. Adv Space Res 37(1):184–190. https://doi.org/10.1016/j.asr.2005.03.028

Kichak RA (2011) Independent GLAS anomaly review board executive summary. Available at https://icesat.gsfc.nasa.gov/icesat/docs/IGARB.pdf. Accessed 25 July 2017

Koons HC, Mazur JE, Selesnick RS, Blake JB, Fennell JF, Roeder JL, Anderson PC (2000) The impact of the space environment on space systems. In: Proceedings of the 6th spacecraft charging conference, AFRL science center, 1 September 2000

Lai ST (2012) Fundamentals of spacecraft charging: spacecraft interactions with space plasmas. Princeton University Press, Princeton

Lam HL, Hruska J (1991) Magnetic signatures for satellite anomalies. J Spacecraft 28(1):93–99. https://doi.org/10.2514/3.26214

Lam MM, Horne RB, Meredith NP, Glauert SA, Griffin TM, Green JC (2010) Origin of energetic electron precipitation >30 keV into the atmosphere. J Geophys Res 115(A4):A00F08. https://doi.org/10.1029/2009JA014619

Lieberman MA, Lichtenberg AJ (1994) Principles of plasma discharges and materials processing. John Wiley & Sons, New York.

Lohmeyer W, Cahoy K, Baker DN (2012) Correlation of GEO communication satellite anomalies and space weather phenomena: improved satellite performance and risk mitigation. In: 30th AIAA international communications satellite system conference (ICSSC), Ottawa, Canada, 24–27 September 2012. https://doi.org/10.2514/6.2012-15083

Mazur JE, Likar JJ, Fennel JF, Roeder JL, O'brien P, Guild TB (2011) The timescale of surface charging events. In: Presentation to the 2011 Space Weather Workshop, Aerospace. Accessed 22 December 2015.

Mikaelian T (2001) Spacecraft charging and Hazards to electronics in space. Canada: York University. Accessed 10 November 2017.

Miloch WJ, Trulsen J, Pecseli HL (2008) Numerical studies of ion focusing behind macroscopic obstacles in a supersonic plasma flow. Phys Rev E77: 056408-1 – 056408-9. https://doi.org/10.1103/PhysRevE.77.056408

Miloch W J (2010) Wake effects and mach cones behind objects, Plasma Phys. Control. Fusion 52(12), 124004. https://doi.10.1088/0741-3335/52/12/124004

Miyake Y, Usui H (2009) New electromagnetic particle simulation code for the analysis of spacecraft-plasma interactions. Phys. Plasmas 16 (062904). https://doi.org/10.1063/1.3147922

Miyake Y, Usui H (2016) Particle-in-cell modeling of spacecraft-plasma interaction effects on double-probe electric field measurements. Radio Science 51(12): 1905-1922. https://doi.org/10.1002/2016RS006095

NASA's Goddard Space Flight Center (NASA GSFC)(2016) OMNIweb data documentation. https://omniweb.gsfc.nasa.gov/html/ow_data.html. Accessed 15 September 2016

NASA (1999) Avoiding problems caused by spacecraft on-orbit internal charging effects. NASA technical handbook, NASA-HDBK-4002. Acessed 1 March 2013.

NOAA's National Center for Environmental Information (NOAA NCEI) (2017) POES space environment monitor data and documentation. http://satdat.ngdc.noaa.gov/sem/poes/data. Accessed 17 April 2017

O'Brien TP (2009) SEAS-GEO: a spacecraft environmental anomalies expert system for geosynchronous orbit. Space Weather 7(9):1. https://doi.org/10.1029/2009SW000473

Patil CG, Rajaram G, Prasad MYS (2008) Correlation of GSO satellite anomalies with space weather data. Acta Astronaut 63(1–4):458–470. https://doi.org/10.1016/j.actaastro.2007.12.050

Peck ED, Randall CE, Green JC, Rodriguez JV, Rodger CJ (2015) POES MEPED differential flux retrievals and electron channel contamination correction. J Geophys Res 120(6):4596–4612. https://doi.org/10.1002/2014JA020817

Pilipenko V, Yagova N, Romanova N, Allen J (2006) Statistical relationship between satellite anomalies at geostationary orbit and high-energy particles. Adv Space Res 37(6):1192–1205. https://doi.org/10.1016/j.asr.2005.03.152

Pisacane VL (2008) The space environment and its effects on space systems. American In-stitute of Aeronautics and Astronautics, Inc, 1801 Alexander Bell Drive, Reston, VA 20191, 2008

Prolss GW (2004) Physics of the Earth's space environment: an introduction. Springer, Berlin

Robertson B, Stoneking E (2003) Satellite GN&C anomaly trends. In: 2003 AAS guidance and control conference, American Astronautical Society guidance and control conference, Breckenridge, United States, 5–9 February 2003

Rodger CJ, Clilverd MA, Green JC, Lam MM (2010) Use of POES SEM-2 observations to examine radiation belt dynamics and energetic electron precipitation into the atmosphere. J Geophys Res. https://doi.org/10.1029/2008JA014023

Rosen A (1976) Spacecraft charging: environment-induced anomalies. J Spacecraft Rockets 13(3): 129-136. https://doi.org/10.2514/3.57073

Rostoker G (2000) Effects of substorms on the stormtime ring current index Dst. Ann. Geophysicae 18: 1390-1398

Samir U, Wren GL (1969) The dependence of charge and potential distribution around a spacecraft on ionic composition, Planetary and Space Science 17(4): 693-706. https://doi.org/10.1016/0032-0633(69)90189-5

Satellite News Digest (SND) (2017) Satellite outages and failures. https://www.sat-nd.com. Accessed 2 August 2017

Schwenn, R (2006) Living Rev. Sol. Phys 3(2). https://doi.org/10.12942/lrsp-2006-2

SIA (2015) State of the satellite industry report – September 2015. Available at http://www.sia.org. Accessed 22 Desember 2015

Space-Track (2015) Two-line element set database. https://www.space-track.org. Accessed 18 November 2015

Stone NH (1981) The Aerodynamics of bodies in a rarefied ionozed gas with applications to spacecraft environmental dynamics. NASA technical paper. Accessed 30 October 2018.

Tadokoro H, Tsuchiya F, Miyoshi Y, Misawa H, Morioka A, Evans DS (2007) Electron flux enhancement in the inner radiation belt during moderate magnetic storms. Ann Geophys 25(6):1359–1364. https://doi.org/10.5194/angeo-25-1359-2007

Tafazoli M (2008) A study of on-orbit spacecraft failures. Acta Astronaut 64(2-3): 195-205. https://doi.org/10.1016/j.actaastro.2008.07.019

Thomsen MF, Henderson MG, Jordanova VK (2013) Statistical properties of the surface-charging environment at geosynchronous orbit. Space Weather 11(5):237–244. https://doi.org/10.1002/swe.20049

Tsurutani BT, Gonzales WD, Gonzales ALC, Guarnieri FL, Gopalswamy N, Grande M, Kamide Y, Kasahara Y, Lu G, Mann I, McPherron R, Soraas F, Vasyliunas V (2006) Corotating solar wind streams and recurrent geomagnetic activity: A review. J Geophys Res 111(A7): 11 107- 11 132. https://doi.org/10.1029/2005JA011273

Ueda, HO, Okada, M, Usui, H, Muranaka, T, Shinohara, I (2009) Estimation of auroral environment by electrostatic full-particle simulations modelling of REIMEI satellite observations. Tran. JSASS Space Terch. Japan, Vol.7, No. ists26, pp. Pr_2_13-Pr_2_18. https://doi.org/10.2322/tstj.7.Pr_2_13

Union of Concerned Scientists (UCS) (2015) UCS satellite database. https://www.ucsusa.org. Accessed 22 December 2015

Vallado DA, McClain WD (1997) Fundamentals of astrodynamics and applications. McGraw-Hill, New York

Vallado DA, Crawford P, Hujsak R, Kelso TS (2006) Revisiting Spacetrack report #3. In: AIAA/AAS astrodynamics specialist conference and exhibit, Keystone, Colorado, 21-24 August 2006. https://doi.org/10.2514/6.2006-6753

Vampola AL (1994) Analysis of environmentally induced spacecraft anomalies. J Spacecraft Rockets 31(2):154–159. https://doi.org/10.2514/3.26416

Wang J, Leung P, Garret H, Murphy G (1994) Multibody-plasma interactions : charging in the wake. J Spacecraft Rockets 31(5): 889-894.

Wang J, Qiu JW, Qin XG (2008), PIC simulation of Surface Charging in the Wake Zone. In: PIERS Proceedings, Hangzhou, China

Wang J, Hastings DE (1992) Ionospheric plasma flow over large high-voltage space plastform. 1: ion-plasma-time scale interactions of a plate at zero angle of attack. Phys. Plasmas 4(1615). https://doi.org/10.1063/1.860069

Welling DT (2010) The long-term effects of space weather on satellite operations. Ann Geophys 28(6):1361–1367. https://doi.org/10.5194/angeo-28-1361-2010.

Wing S, Gkioulidou M, Johnson JR, Newell PT, Wang CP (2013) Auroral particle precipitation characterized by the substorm cycle. J Geophys Res 118(3):1022–1039. https://doi.org/10.1002/jgra.50160.

Wu CC, Liou K, Lepping RP, Meng CI (2004) Identification of subtorms within storms. J Atmos Terr Phys 66(2):125–132. https://doi.org/10.1016/j.jastp.2003.09.012

Yeh HC, Gussenhoven MS (1987) The statistical electron environment for Defense Meteorological Satellite Program eclipse charging. J Geophys Res 92(A7): 7705-7715. https://doi.org/10.1029/JA092iA07p07705

Appendix A

Space Weather Variation Around the Anomaly Day of LEO Satellites

A.1 Pattern II (geophysical parameters variation prior to the anomaly day)

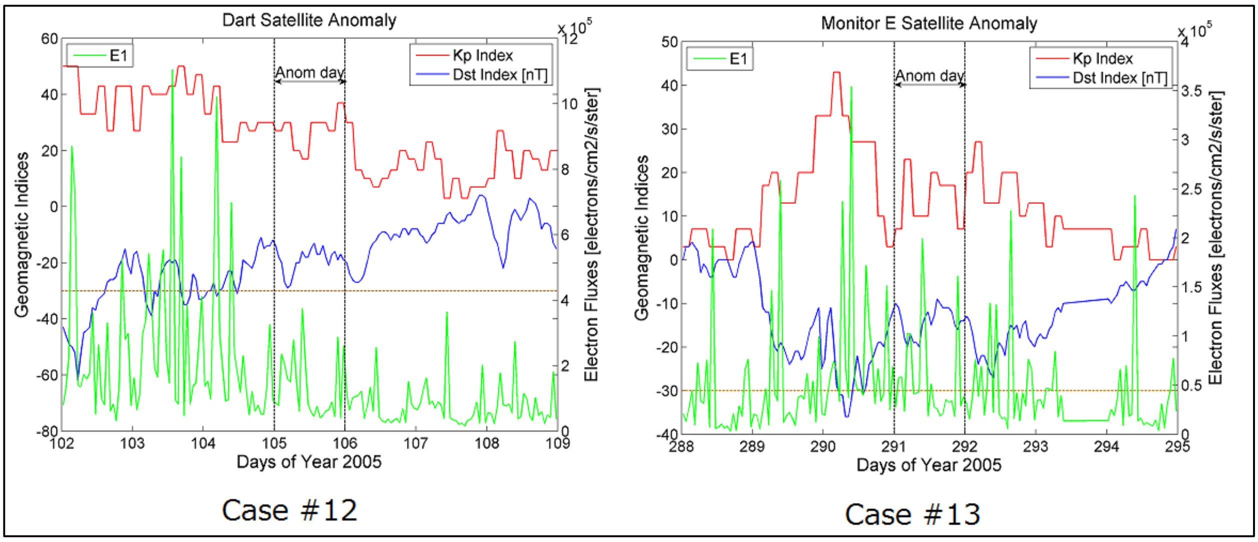

A.2 Pattern III (multiple variations of geophysical parameters around the anomaly day)

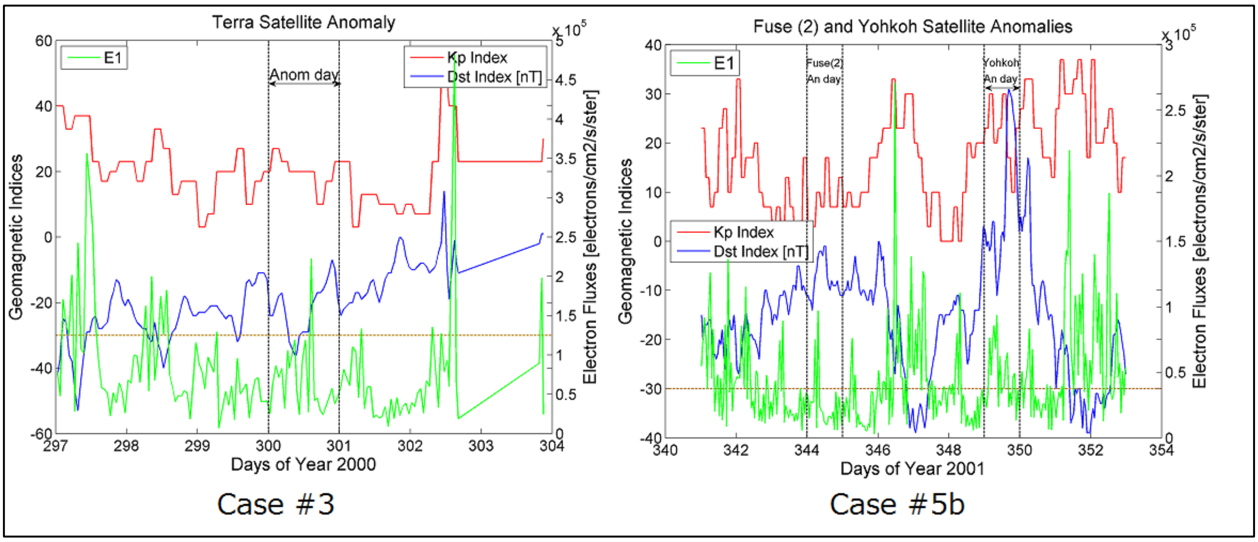

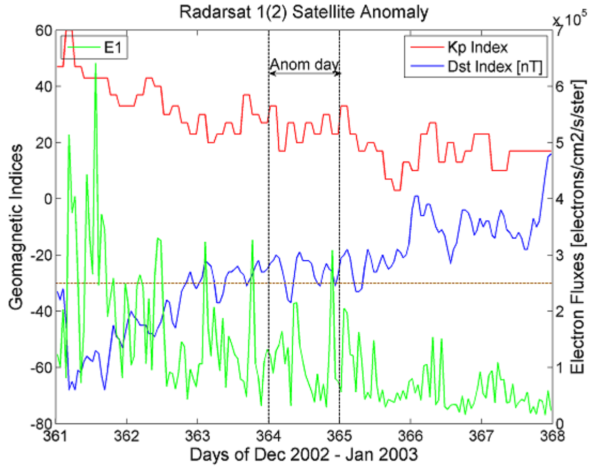

Case #8

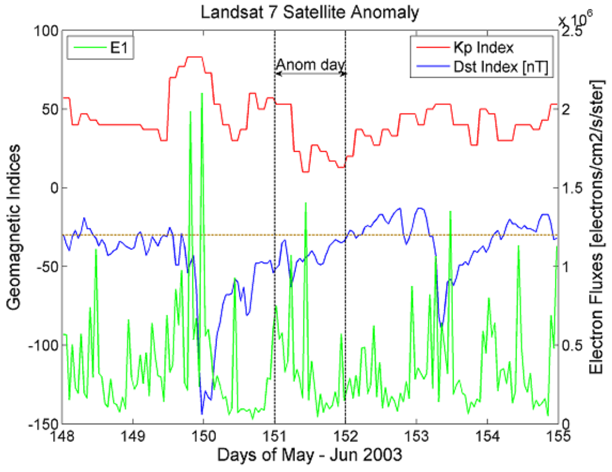

Case #9

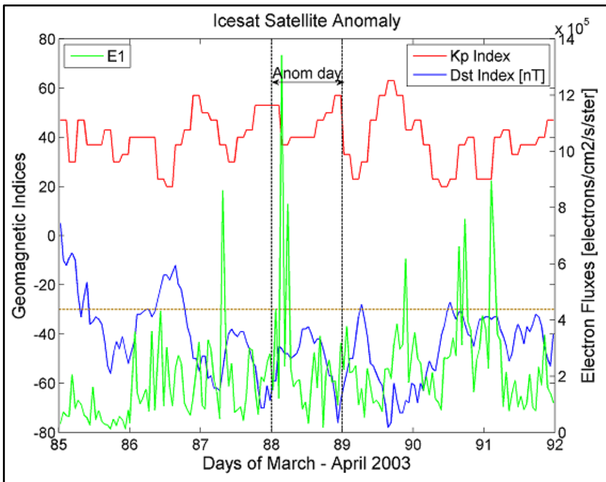

Case #10

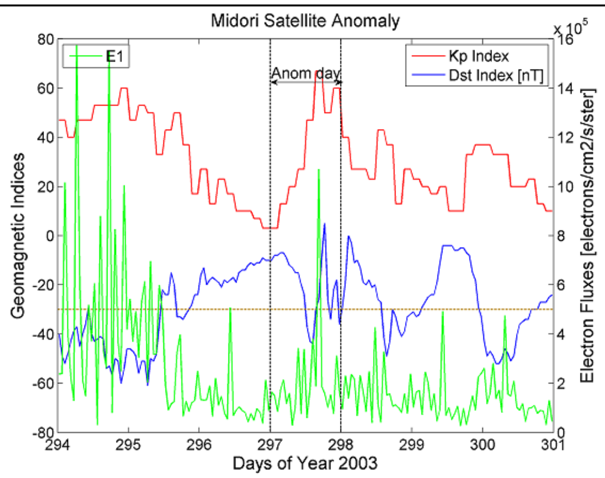

Case #11

A.3 Weak link (low level of geomagnetic storm/substorm)

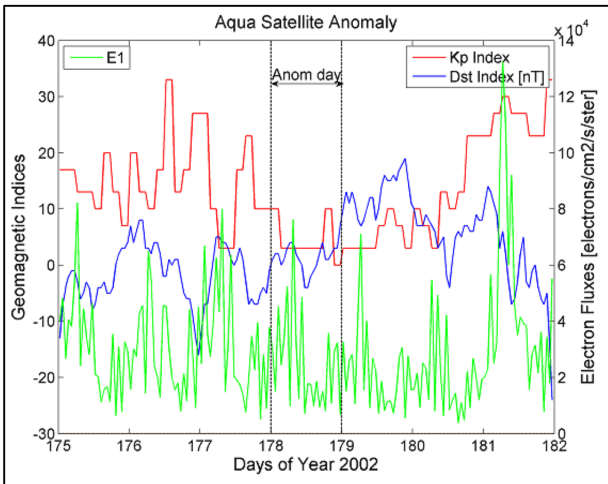

Case #6

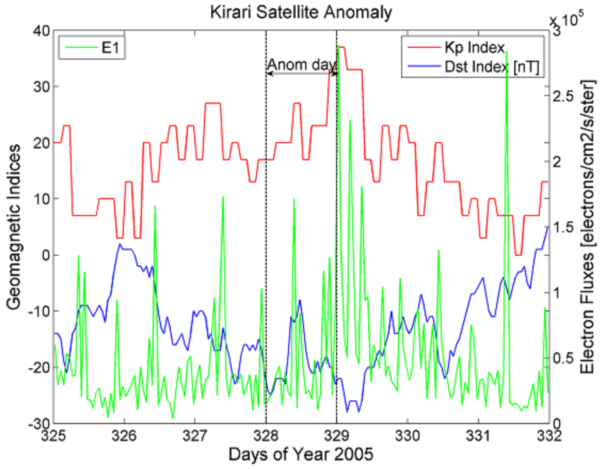

Case #14

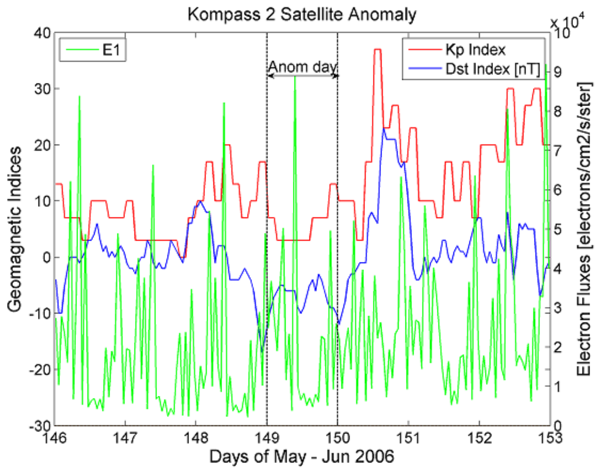

Case #15

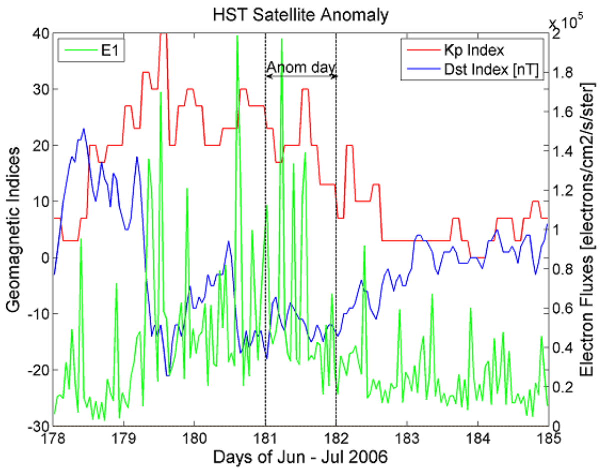

Case #16

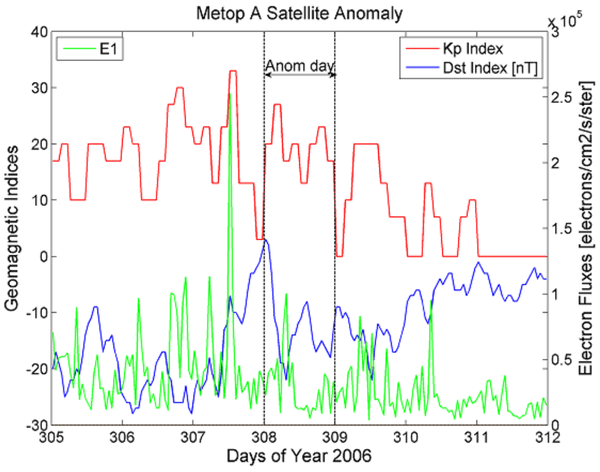

Case #17

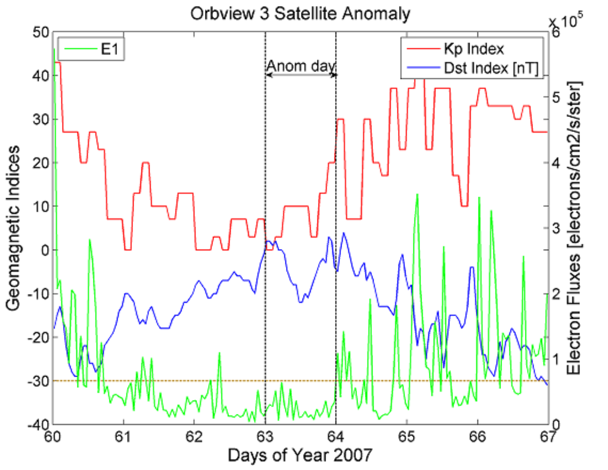

Case #18

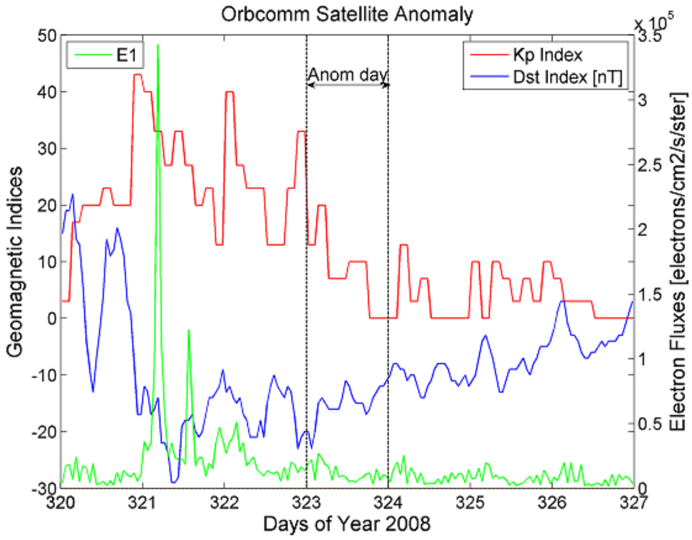

Case #19

Appendix B

Active Satellites and Anomalous Systems

B. 1 Number of on Orbiting Active Satellites by Function in 2015

(SIA 2016 in https://www.sia.org)

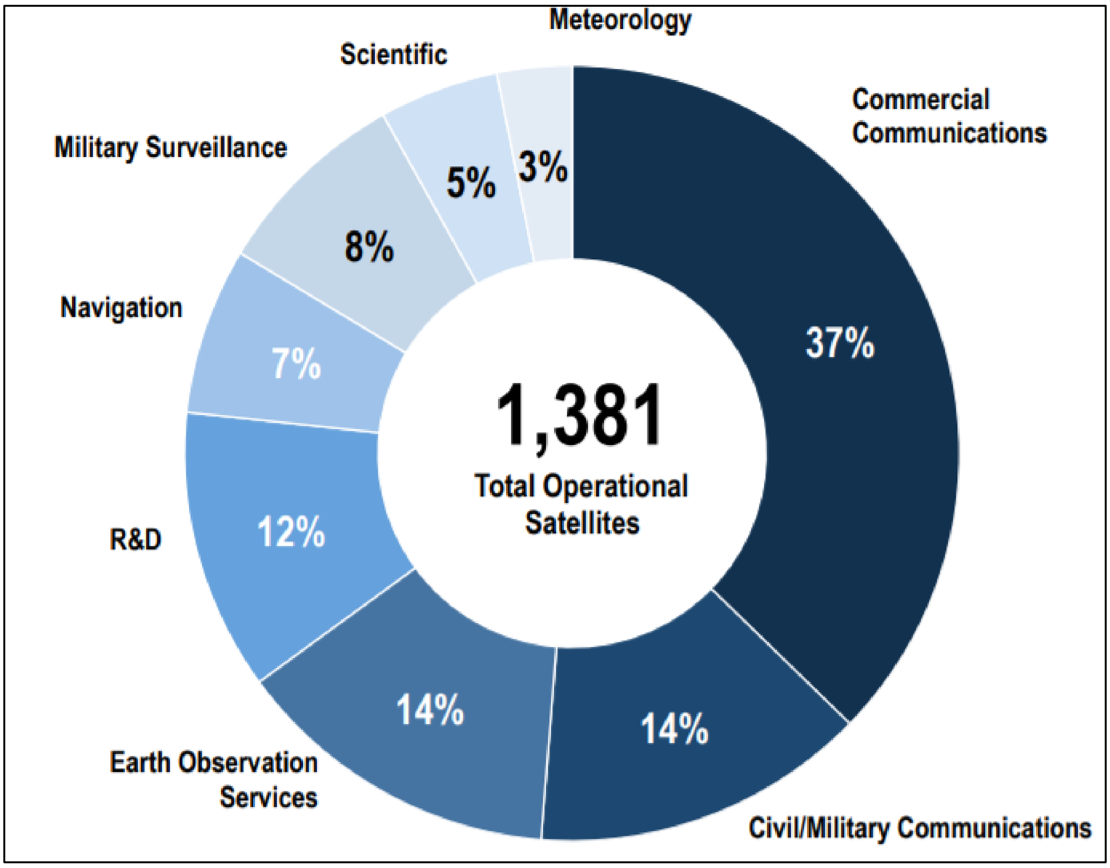

B. 2 Anomalous Systems on Satellite (Tafazoli M, Acta Astronautica, page 195-205,2009)

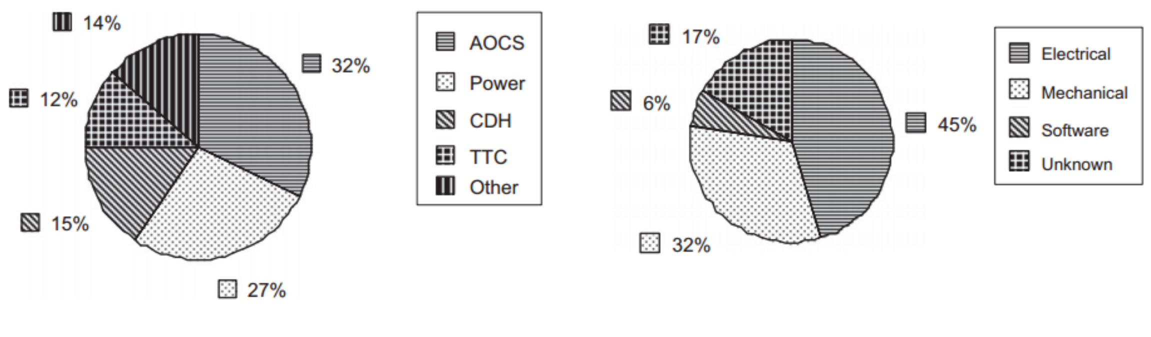

1. Spacecraft subsystems failures

2. Types of failures on spacecraft

AOCS : Attitude and Orbit Control System

CDH : Command and Data Handling

TTC : Telemetry, Tracking and Command

Doctor Thesis, Kobe University
"Study on LEO Satellite Charging and Associated Plasma Disturbance in the Ionosphere"
107 pages
Submitted on January 23rd, 2019

The date of publication is printed in cover of repository version published in Kobe University Repository Kernel.